ABSTRACT

Title of dissertation: THE EFFECTS OF TURBULENCE ON MAGNETIC RECONNECTION AT THE MAGNETOPAUSE

Lora McMurtrie Price, Doctor of Philosophy, 2017

Dissertation directed by: Professor James Drake
Department of Physics

Magnetic reconnection facilitates the conversion of magnetic energy to thermal energy and plasma flows. Reconnection occurs at the magnetopause, the magnetic boundary between the plasmas of the terrestrial magnetosphere and the heliosphere. Turbulence is known to develop at this boundary, but its influence on reconnection, particularly on small scales, is unknown. In light of this, an important goal of NASA's Magnetospheric Multiscale (MMS) Mission is to understand the role turbulence plays in the development of reconnection.

We present two- and three-dimensional particle-in-cell simulations of the 16 October 2015 MMS magnetopause reconnection event. While the two-dimensional simulation is laminar, turbulence develops at both the x-line and along the magnetic separatrices in the three-dimensional simulation. This turbulence is electromagnetic, is characterized by a wavevector k given by $k\rho_e \sim (m_e/m_i)^{0.25}$ with ρ_e the electron Larmor radius, and appears to have the ion pressure gradient as its source of free energy. Taken together, these results suggest the instability is a variant of the

lower-hybrid drift instability. The turbulence produces electric field fluctuations in the out-of-plane direction with an amplitude of around ± 10 mV/m, which is much greater than the reconnection electric field of around 0.1 mV/m. Such large values of the out-of-plane electric field have been identified in the MMS data. The turbulence in the simulation controls the scale lengths of the density profile and current layers, driving them closer to $\sqrt{\rho_e \rho_i}$ than the ρ_e or d_e scalings seen in 2D reconnection simulations, where d_e is the electron inertial length. The turbulence produces both anomalous resistivity and anomalous viscosity. Each contribute significantly to breaking the frozen-in condition in the electron diffusion region. The crescent-shaped features in velocity space seen both in MMS observations and in two-dimensional simulations survive. We compare and contrast these results to a three-dimensional simulation of the 8 December 2015 MMS magnetopause reconnection event in which the reconnecting and out-of-plane guide fields are comparable. LHDI is still present in this event, although its appearance is modified by the presence of the guide field. The crescents also survive although, in agreement with MMS, their intensity decreases. Nevertheless, the developing turbulence remains strong.

THE EFFECTS OF TURBULENCE ON MAGNETIC RECONNECTION AT THE MAGNETOPAUSE

by

Lora McMurtrie Price

Dissertation submitted to the Faculty of the Graduate School of the
University of Maryland, College Park in partial fulfillment
of the requirements for the degree of
Doctor of Philosophy
2017

Advisory Committee:
Professor James F. Drake, Chair/Advisor
Dr. Michael M. Swisdak, Co-Advisor
Professor Adil B. Hassam
Dr. David Sibeck
Dr. Jason TenBarge
Professor Thomas Antonsen, Dean's Representative

Acknowledgments

I am incredibly grateful for the support from my advisors Jim Drake and Marc Swisdak. I would never have succeeded if not for their flexibility and near-infinite patience. Special thanks go to Adil Hassam, who advised me for a year and introduced me to plasma physics. Thanks also go to Dave Sibeck, Jason TenBarge, and Tom Antonsen for agreeing to sit on my committee.

I would also like to thank my past officemates: Wrick Sengupta, Joel Dahlin, Qile Zhang, Kevin Schoeffler, Ray Fermo, and Yi-Hsin Liu. You made the office feel like a second home. Additional thanks to other colleagues in the plasma physics group: Jimmy Juno, Matt Landreman, Tak Chu Li, Mike Martin, Obioma Ohia, Elizabeth Paul, Gareth Roberg-Clark, and George Wilkie. You reminded me that it's always worth taking a break for cupcakes. I would be remiss to not thank my current officemate Baxter, though if I'm being honest I could do with a little less barking during Skype calls. Or really less barking in general.

I am so proud to have been involved with the UMD Women in Physics group, because I met so many wonderful people through it: Michelle Groce, Kristen Burson, Caitlin Williams, Caroline Figgatt, Amy Gabel, Hannalore Gerling-Dunsmore, Deborah Hemingway, Hilary Hurst, Rachel Lee, Megan Marshall, Kim Moore, Gina Quan, Holly Tinkey, Sonali Shukla, and Donna Hammer. While I was involved in (too) many things during my time in grad school, I will never regret the time I spent with you all. Special thanks to Caroline, Gina, and Megan, who are strong as heck.

I would also like to thank Zach Smith, who I could only beat at Mario Kart

because Baxter was licking his head. Thanks to Mark Herrera for commiserating with me. Thank you to friends I've known since high school: Gabrielle Arrowood, Randi Skullestad, and Alison Ven.

I am grateful for the support from the Wyvill clan. You all welcomed me like, well, family. Visiting one week a year can't compare to living nearby. My summers are less bright without those pool parties; my holidays less merry without forty of us crammed into an unlucky person's house or the farm.

Thanks to Aunt Val, who inspires me to stick it to The Man.

Thank you to my parents and my seester, Christie. You make me feel capable and smart when I feel anything but. It's been a long and difficult journey, but your love and support have helped more than I can say.

Thank you to my husband Ryan. You continuously push me to be better and to not sell myself short. When I see myself through your eyes, I feel like I can accomplish anything. You're my favorite.

Lastly, thanks to two of my high school teachers: Phil Bombino and Robert Stauffer. They started me on this path, and I can only hope to inspire students as they inspired me.

Table of Contents

List of Figures

List of Abbreviations

$\mathbf{B}$	Magnetic field
$\mathbf{b}$	Magnetic field unit vector ($\mathbf{B}/\lvert\mathbf{B}\rvert$)
$\mathbf{E}$	Electric field
$\mathbf{J}$	Current density
$\mathbf{v}$	Plasma flow velocity
$E_\parallel$	Parallel electric field ($\mathbf{E}\cdot\mathbf{b}$)
P	Plasma pressure
T	Plasma temperature
n	Particle density
β	Plasma beta
d_i	Ion inertial length
d_e	Electron inertial length
λ_D	Debye length
ρ_i	Ion Larmor radius
ρ_e	Electron Larmor radius
ϵ_B	Inverse length scale of the magnetic field
ϵ_n	Inverse length scale of the density
ϵ_T	Inverse length scale of the (electron) temperature
ω_{ci}	Ion cyclotron frequency
ω_{ce}	Electron cyclotron frequency
ω_{pi}	Ion plasma frequency
ω_{pe}	Electon plasma frequency
Ω_{lh}	Lower-hybrid frequency
c_A	Alfvén velocity
c	Speed of light
v_i	Ion thermal velocity
v_e	Electron thermal velocity
v_E	$E \times B$ velocity
v_{di}	Ion diamagnetic drift velocity
v_{de}	Electron diamagnetic drift velocity
e	Electron charge
m_i	Ion mass
m_e	Electron mass
R_e	Earth radius

LHDI	Lower-hybrid drift instability
MHD	Magnetohydrodynamics
MMS	Magnetospheric Multiscale Mission
MTSI	Modified two-stream instability
STDT	Science and Technology Definition Team

Chapter 1: Introduction

1.1 History of Magnetic Reconnection

Magnetic reconnection is a fundamental plasma process that facilitates the conversion of magnetic energy to high-speed plasma flows and thermal energy. The idea of magnetic reconnection was proposed in the 1950s, but our understanding of the process is still incomplete. An excellent overview of the topic, including discussion of the many mysteries still remaining, can be found in [1].

Magnetic reconnection was proposed in an attempt to understand solar flares. Solar flares are large bursts of radiation near the surface of the sun, accompanied by sudden flashes of light and, usually, the ejection of material from the plasma surrounding the sun. The first observed solar flare, now dubbed the 'Carrington Flare,' was observed independently by Richard C. Carrington and Richard Hodgson in 1859 [2,3]. Almost a century later, Ron Giovannelli noted that solar flares often occur in regions with a reversal of magnetic field [4]. Upon investigation, James Dungey found that oppositely directed magnetic field lines could break apart and reconnect because of diffusion, forming a thin current sheet in the process [5,6]. He later coined the term 'magnetic reconnection.'

In 1956, Peter Sweet presented a model of reconnection at a conference. In

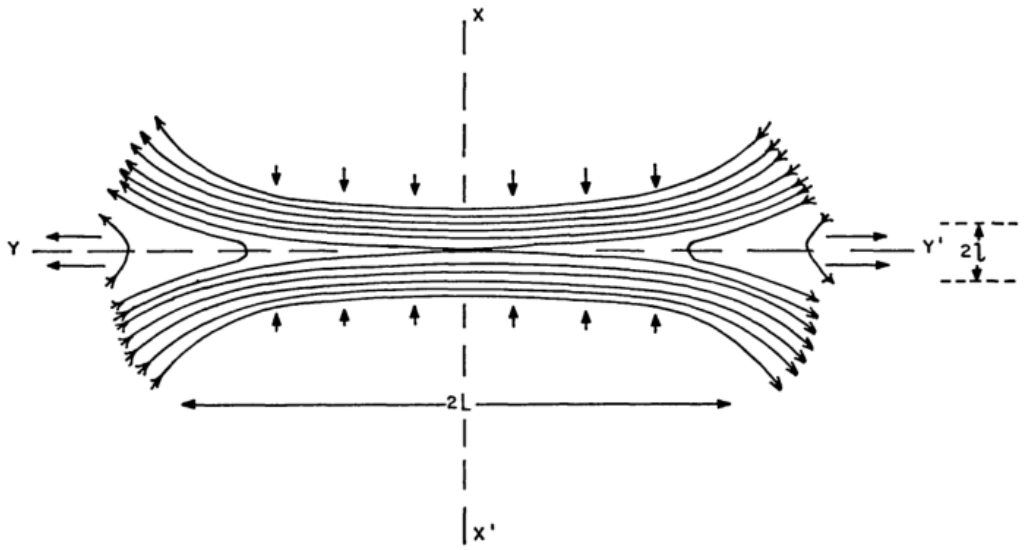

Figure 1.1: Sweet-Parker reconnection. Oppositely directed magnetic field lines are driven together. The field lines break and reconnect, and plasma and field lines are ejected to the left and right. Reprinted from Parker, 1963 [7]

his model, bipolar magnetic fields were pressed together, forming Dungey's diffusive region [8]. Eugene Parker was in attendance and used steady-state scaling analysis to derive what is now known as Sweet-Parker reconnection (see Figure 1.1) [9, 10]. While this collisional reconnection model has been confirmed in the laboratory, it predicts a magnetic energy dissipation rate far faster than diffusion alone but far slower than that observed in solar flares.

As will be discussed in Chapter 2, one of the reasons Sweet-Parker reconnection is slow is the large aspect ratio of the reconnection layer (ℓ/L in Figure 1.1). In 1964, Harry Petscheck proposed an alternate model where the inflow and outflow regions are separated by stationary slow shocks, resulting in a small Sweet-Parker diffusion region [11]. While this model predicts a dissipation rate comparable to that seen

in solar flares, it has since been found that this configuration is unsustainable [12] unless the resistivity (which is the main mechanism for reconnection) is locally non-uniform [13].

Recent work has shown that incorporating the Hall effect can support the Petschek configuration [14]. With a thin enough current layer, small-scale kinetic[1] physics allows energy to be released fast enough to explain observed energy release times [15]. This 'Hall reconnection' has been observed in the magnetosphere [16–18].

Although magnetic reconnection was originally proposed to explain solar flares, it is an important process seen in both space physics (geomagnetic storms, aurora, and coronal mass ejections) and the laboratory (the sawtooth crash is a major impediment to achieving magnetic confinement in fusion devices). Reconnection is also suspected of playing an important role in astrophysical contexts as well.

1.2 The Magnetosphere

A magnetosphere is the region around a planet in which the planet's magnetic field exerts a dominant influence. While other planets and comets have magnetospheres (see [19] for a thorough overview), Earth's magnetosphere has been the most studied and is the focus of the Magnetospheric Multiscale (MMS) Mission.

[1] Kinetic scales are those smaller than a collisional mean free path. Above kinetic scales, plasmas can be modeled as fluids moving with collective motion. Below kinetic scales, the fact that plasma consists of individual particles is important.

1.2.1 History

The study of the magnetosphere begins with William Gilbert's proposal in 1600 that Earth has a dipolar magnetic field [20]. While the Earth's magnetic field is essentially dipolar near the surface, further out it is distorted. The cause of this distortion was unknown for another three and a half centuries.

On the day following the Carrington flare in 1859, a geomagnetic storm occurred. Carrington supposed the flare and the storm were related and suggested that there were particles flowing from the sun [2]. In the 1930s, Sydney Chapman and Vincent C. A. Ferraro hypothesized that plasma was emitted by the sun and was deflected by the Earth's magnetic field [21–24]. In 1951, Ludwig Biermann noted that, regardless of travel direction, the tail of a comet always points away from the sun [25]. It was not until 1958 that Eugene Parker theorized that these separate hypotheses were describing the effects of a singular phenomenon, which he called the solar wind [26].

The following year, Thomas Gold proposed the name 'magnetosphere' [27]. In 1961, Dungey proposed that magnetic reconnection could be a mechanism that transmits solar wind energy to the magnetosphere [28]. By the 1960s, much work had been done to probe the inner magnetosphere. This work was spearheaded by James Van Allen, and by 1958, Explorer 1 and 3 [29] had detected the Earth's radiation belt [30]. In 1961, Explorer 12 observed the magnetopause, which had been predicted by Chapman and Ferraro [31, 32]. Cluster II [33] and THEMIS [34] are more recent missions probing the magnetosphere. The Magnetospheric Multiscale

Mission continues this work, to learn as much as we can about the magnetosphere.

1.2.2 Structure

A detailed overview of the structure of magnetospheres can be found in [19]. All of the planets in our solar system have magnetospheres. If a planet does not have its own magnetic field (Venus and possibly Mars), its magnetosphere is called induced; otherwise, a planet's magnetosphere is intrinsic. Regardless of its nature, each planet's magnetosphere is bounded by a bow shock. This bow shock is caused by the solar wind decelerating and deflecting as it encounters the planet. When the solar wind encounters the magnetosphere on the dayside (the side of the planet facing the sun), the solar wind magnetic field lines drape around the planet. Due to this draping, the nightside (the side of the planet facing away from the sun) has a region of extended magnetic field lines, that may or may not intersect with the planet, called the magnetotail. In an induced magnetotail, these field lines do not intersect with the planet but close on themselves, usually in the tail. In an intrinsic magnetotail, these magnetic field lines intersect the planet at the polar caps and stretch into the nightside. The last features discussed herein are only found in intrinsic magnetospheres. The area where the pressure from the planetary magnetic field is equal to the pressure from the solar wind is called the magnetopause (discussed extensively in [35]). Conditions at the magnetopause are varied and complex, and as such it is an ideal location to investigate asymmetric magnetic reconnection. The area between the magnetopause and the bow shock is referred to

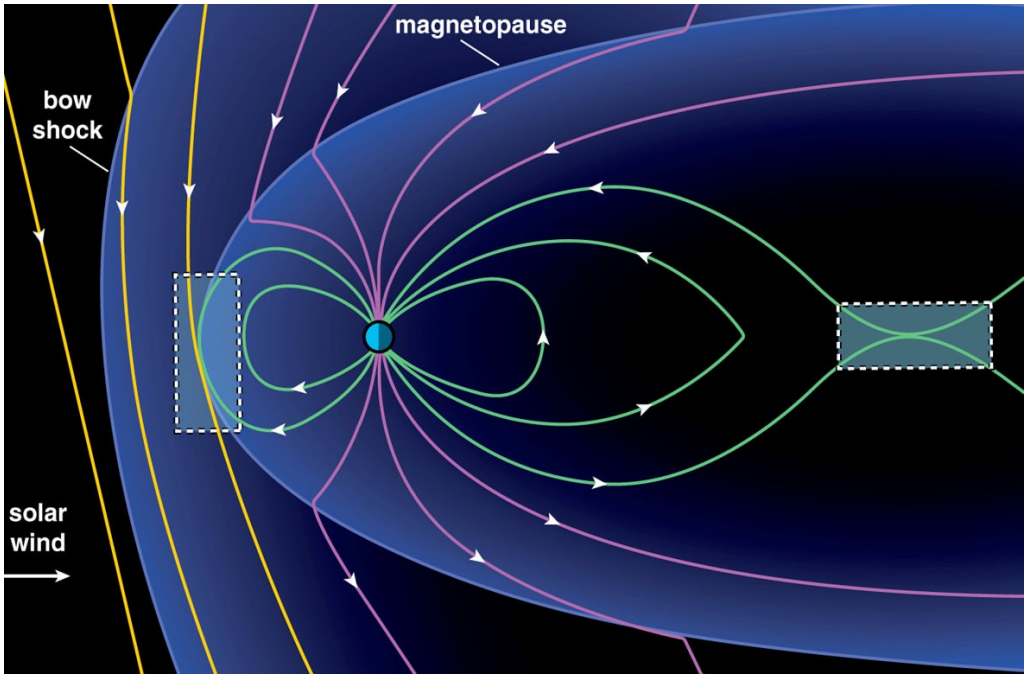

Figure 1.2: The magnetosphere in the noon-midnight meridian plane. The rectangles denote locations where magnetic reconnection is frequently observed– left, at the magnetopause, and right, in the magnetotail. Reprinted from Burch et al., 2016 [36] [2]

as the magnetosheath.

A sketch of Earth's magnetosphere can be seen in Figure 1.2. Though distances fluctuate by several R_e due to fluctuations in the solar wind, the bow shock is located approximately $13R_e$ in front of the Earth, while the magnetopause is about $10R_e$ away along the Earth-Sun line. The magnetopause stretches about $15R_e$ on either side of the Earth before continuing in the nightside. Magnetic reconnection in the magnetotail occurs in primarily two regions: near-Earth between 20 and $30R_e$, and more distant, as far as $140R_e$ [37].

1.3 The Magnetospheric Multiscale Mission

The Magnetospheric Multiscale Mission (or MMS) officially began in 2002 [36], although the mission itself was some time longer in planning. The MMS Science and Technology Definition Team (STDT) report in 1999 [37] identified four key questions about reconnection to be probed with MMS:

1. What are the kinetic processes responsible for collisionless magnetic reconnection, and how is reconnection initiated?

2. Where does reconnection occur at the magnetopause and in the magnetotail, and what influences where it occurs?

3. How does reconnection vary with time, and what factors influence its temporal behavior?

4. How are flux transfer events and plasmoids/magnetotail flux ropes formed, and how do they evolve?

The original STDT plan recommended the use of five spacecraft, identically instrumented, flying in either a hexahedral or "quad-tetrahedra" formation, to be launched in June 2006. As is often the case, the mission plan evolved in both objective and implementation. With advancements in both theory and modeling, the MMS science goal became to "[u]nderstand the microphysics of magnetic reconnection by determining the kinetic processes occurring in the electron diffusion region that are responsible for collisionless magnetic reconnection, especially how

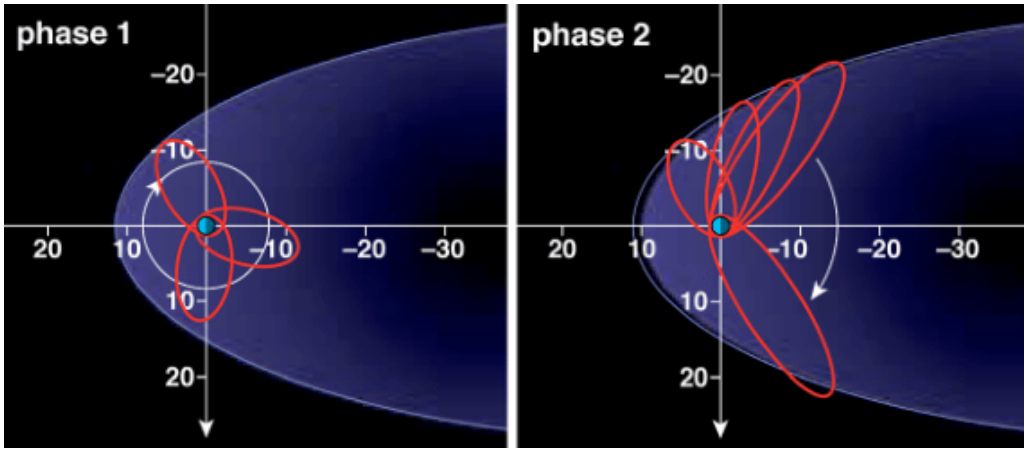

Figure 1.3: Sketch of the MMS orbits for phases 1 and 2. The axes are in units of R_e. Reprinted from Burch et al., 2016 [36] [2]

reconnection is initiated" [36]. Its three specific objectives are, in order of priority:

1. Determine the role played by electron inertial effects and turbulent dissipation in driving magnetic reconnection in the electron diffusion region.

2. Determine the rate of magnetic reconnection and the parameters that control it.

3. Determine the role played by ion inertial effects in the physics of magnetic reconnection.

The plan was also pared down from the original five to four identical spacecraft flying in tetrahedral formation. These spacecraft were successfully launched on March 12, 2015.

The mission itself has two planned phases (depicted in Figure 1.3), the first probing the dayside magnetopause and the second the nightside magnetotail. In

the first phase, the spacecraft travel in an orbit with perigee at $1.2R_e$ and apogee at $12R_e$, which in the second phase the apogee is raised to $25R_e$. Phase One began almost six months after the launch date on September 1, 2015. The second phase is expected to start in May 2017.

MMS boasts several improvements over previous missions. The four spacecraft can maintain a spacing of as little as 10 km, with an accuracy of 100 m [36]. This spacing of 10 km translates roughly to $6d_e$ (where d_e is the electron inertial length), based on a magnetosheath density of 12cm^{-3} [38]. For comparison, Cluster II's minimum spacing distance is 200 km [37]. The spacecraft accurately measure the three-axis electric and magnetic fields with cross-calibrations to measure variations in both time and space. The spacecraft also measure all-sky electron and ion velocity-space distributions with time resolutions of 30 ms for electrons and 150 ms for ions. Previous resolutions were in the seconds range.

1.4 Summary of Results

Earth's magnetosphere is an ideal laboratory to investigate the intricacies of magnetic reconnection, and MMS's high spatial- and temporal-resolution measurements allow us to probe the electron-scale kinetic physics in the region around the X-line.

Chapter 2 is a brief discussion of magnetic reconnection theory, including the differences between symmetric and asymmetric reconnection.

In Chapter 3, I discuss in depth a particular type of instability that is com-

monly observed in asymmetric configurations likely to be found at the magnetopause, the lower-hybrid drift instability (LHDI).

In Chapter 4, I discuss two- and three-dimensional simulations with initial conditions reflective of a magnetic reconnection event observed by MMS. The inclusion of the third dimension permits the development of strong turbulence, which makes significant contributions to the balance of Ohm's Law. This turbulence does not disrupt the formation of crescent-like features observed by MMS in velocity-space distribution functions.

In Chapter 5, I perform detailed analysis of the turbulence observed in this simulation and another with a more realistic mass-ratio. This turbulence is electromagnetic in nature and is characterized by a wavevector given by $k\rho_e \sim (m_e/m_i)^{0.25}$, which suggests the instability is LHDI.

In Chapter 6, I present preliminary results of a three-dimensional simulation with initial conditions reflective of another reconnection event observed by MMS, this time with a significant guide field. Strong turbulence develops along the magnetosphere separatrix with a wavevector again consistent with LHDI. We reproduce the crescent-shaped distribution functions observe by MMS. The strong turbulence that develops does not appear to significantly contribute to the balance of Ohm's Law. More simulations are needed to explore turbulence near the X-line.

In Chapter 7, I summarize my conclusions and discuss possible future work.

[2]Reprinted without modification under the terms of the Creative Commons license, http://creativecommons.org/licenses/by/4.0/

Chapter 2: Magnetic Reconnection

In this chapter I discuss the general theory behind magnetic reconnection. First I present the ideal magnetohydrodynamic (MHD) formulation of plasma physics, the concept of magnetic tension, and the frozen-in theorem. Next I discuss the general reconnection process, where magnetic energy is released in an effort to minimize magnetic tension and the frozen-in theorem is no longer valid. I then consider steady-state reconnection, comparing and contrasting Sweet-Parker reconnection with Hall reconnection. Magnetopause reconnection is often asymmetric, as seen in MMS observations, and the simulations presented in Chapters 4-6 focus on asymmetric reconnection. As such, I discuss the differences between symmetric and asymmetric reconnection, where I derive Sweet-Parker scaling laws for asymmetric reconnection and show that the X-point and stagnation point are generally not co-located. I conclude by describing the particle-in-cell (PIC) code used in the simulations presented in Chapters 4-6.

2.1 Magnetohydrodynamics

A simple model of the behavior of plasma is magnetohydrodynamics (MHD), where plasma is treated like an electrically conducting fluid. MHD is usually suffi-

cient to describe the global behavior of plasma, though as we will see in a moment, it does not hold in certain regions of interest.

The equations governing ideal MHD are as follows:

$$\frac{\partial \rho}{\partial t} + \boldsymbol{\nabla} \cdot (\rho \mathbf{v}) = 0 \tag{2.1}$$

$$\rho \frac{d\mathbf{v}}{dt} = \frac{1}{c}\mathbf{J} \times \mathbf{B} - \boldsymbol{\nabla} P \tag{2.2}$$

$$\frac{\partial \mathbf{B}}{\partial t} = -c\boldsymbol{\nabla} \times \mathbf{E} \tag{2.3}$$

$$\boldsymbol{\nabla} \times \mathbf{B} = \frac{4\pi}{c}\mathbf{J} \tag{2.4}$$

$$\mathbf{E} + \frac{1}{c}(\mathbf{v} \times \mathbf{B}) = 0 \tag{2.5}$$

These are the continuity equation, the momentum equation, Faraday's Law, Ampére's Law, and the ideal Ohm's Law, respectively. Here, ρ is the mass density, $\mathbf{v}$ is the bulk velocity, $\mathbf{J}$ is the current density, $\mathbf{B}$ is the magnetic field, P is the scalar pressure, $\mathbf{E}$ is the electric field, and $d/dt = \partial/\partial t + \mathbf{v} \cdot \boldsymbol{\nabla}$ is the convective derivative. An additional equation, usually the adiabatic equation of state, is needed to close this set of equations.

The momentum equation (Eq. 2.2) can be rewritten, by substituting $\mathbf{J}$ from equation 2.4, as

$$\rho \frac{d\mathbf{v}}{dt} = \frac{\mathbf{B} \cdot \boldsymbol{\nabla}\mathbf{B}}{4\pi} - \boldsymbol{\nabla}\frac{B^2}{8\pi} - \boldsymbol{\nabla} P. \tag{2.6}$$

The first term on the right-hand side corresponds to magnetic tension, acting to straighten curved magnetic field lines. It acts in the direction of $\mathbf{b} \cdot \boldsymbol{\nabla}\mathbf{b}$, where $\mathbf{b} = \mathbf{B}/|\mathbf{B}|$ is the unit vector in the direction of $\mathbf{B}$. The second term on the right-hand side represents the magnetic pressure, which acts in a manner similar to the thermal pressure P.

2.1.1 Frozen-in Theorem

One of the most important results obtained using ideal MHD theory is Alfvén's frozen-in theorem [39]. It states that, in a system with infinite electric conductivity (i.e. one where the ideal Ohm's Law holds) magnetic field lines are "frozen" to the surrounding fluid and must move with the fluid. Thus in such a system a field line cannot break.

Mathematically, this is stated as

$$\Phi = \int_S \mathbf{B} \cdot d\mathbf{S} = const, \tag{2.7}$$

i.e., the magnetic flux Φ moving through a surface is constant. This result is obtained with the help of the induction equation,

$$\frac{\partial \mathbf{B}}{\partial t} = \boldsymbol{\nabla} \times (\mathbf{v} \times \mathbf{B}), \tag{2.8}$$

which comes from the combination of equations 2.3 and 2.5. The change of magnetic flux over time is

$$\frac{d\Phi}{dt} = \frac{d}{dt}\int_S \mathbf{B} \cdot d\mathbf{S} = \int_S \frac{\partial \mathbf{B}}{\partial t} \cdot d\mathbf{S} + \oint_C \mathbf{B} \cdot \mathbf{v} \times d\mathbf{l}. \tag{2.9}$$

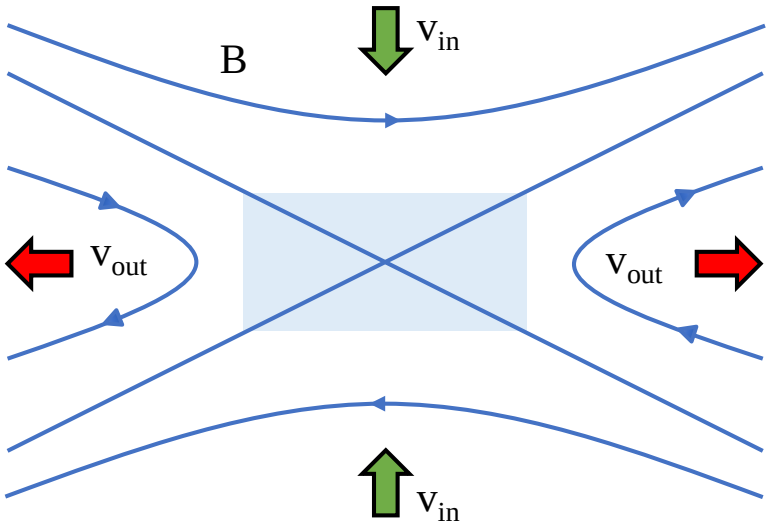

Figure 2.1: Two-dimensional reconnection. Oppositely directed magnetic field lines are drawn into the diffusion region (shaded blue), where they break and reconnect before being drawn into the outflow region.

When substituting the induction equation (equation 2.8) into the first term on the right-hand side and invoking Stokes' theorem, the entire right-hand side vanishes, resulting in equation 2.7.

2.2 Reconnection Theory

2.2.1 The Reconnection Process

While MHD is usually a good approximation for plasma behavior, it is not sufficient to explain magnetic reconnection. Figure 2.1 shows a canonical reconnection

configuration. Oppositely directed magnetic field lines, on the top and bottom, are separated by separatrices, meeting at a central X-line. The magnetic tension in the curved field lines pulls the field lines away from the diffusion region (the region near the X-line, shaded blue), driving the pressure down in the diffusion region. This lower pressure draws in plasma from outside the diffusion region (above and below the blue region), where the frozen-in theorem is still valid, bringing magnetic field lines with it. These new magnetic field lines cross the separatrix, where they break and reconnect with a magnetic field line on the opposite side of the X-line. Because the magnetic field lines break, plasma is no longer frozen to these lines. Thus in this diffusion region, the frozen-in theorem is no longer true, implying that the physics not included in the ideal Ohm's Law (Eq. 2.5) is important for enabling magnetic reconnection. The magnetic field lines that result are heavily bent, and the tension in the field lines causes them to accelerate out of the diffusion region in the direction shown by the green arrows in an attempt to straighten. Once out of the diffusion region, the frozen-in theorem holds, so these field lines accelerate plasma out of the region, further drawing the pressure in the diffusion region down. This self-driven process continues until all available magnetic flux in the inflow/upstream region is spent.

A large percentage of the initial energy in the magnetic field lines is released in this process. To demonstrate this, consider a contracting magnetic bubble (usually referred to as a magnetic island) as seen in Figure 2.2. The initial bubble has major radius L and minor radius w, with $w \ll L$. The island contracts in an effort to minimize magnetic tension, resulting in a bubble of radius R. Reconnection is a

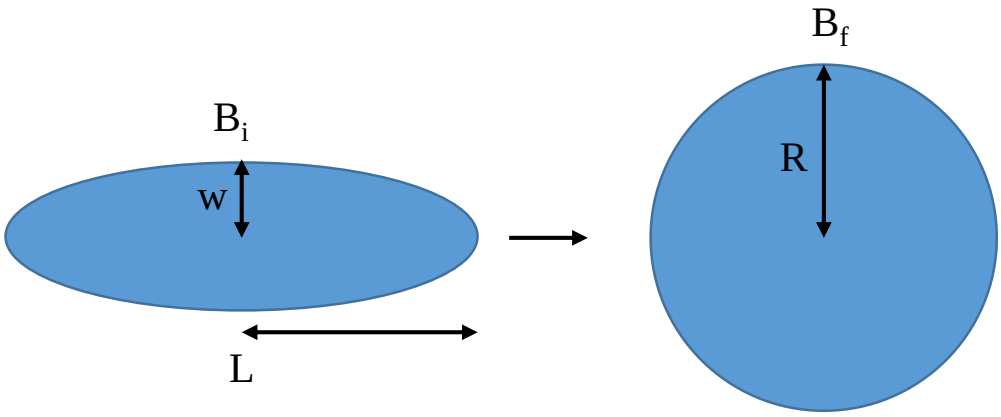

Figure 2.2: Cartoon of a squashed magnetic bubble contracting. Figure and example courtesy of Jim Drake.

nearly incompressible process, so the area of the bubble is conserved through this process, giving $\pi wL \approx \pi R^2$ or $R \approx \sqrt{wL}$. The magnetic flux Φ is also conserved, so $B_i w = B_f R$, where B_i is the initial magnetic field, predominantly in the horizontal direction. The magnetic energy $\mathcal{E}$ depends on both the area and the magnetic energy density $B^2/8\pi$, but as the area is conserved in this process, the ratio of final and initial energies only depends on the ratio of the magnetic energy densities:

$$\frac{\mathcal{E}_f}{\mathcal{E}_i} = \frac{B_f^2}{B_i^2} = \left(\frac{w}{R}\right)^2 = \frac{w}{L} \ll 1. \tag{2.10}$$

Thus, most of the initial energy in the magnetic fields is converted to plasma energy.

Outside of the diffusion region the frozen-in theorem holds, so as the magnetic island contracts, plasma moves with the field lines. If we suppose that almost all of the initial magnetic field energy $B_i^2/8\pi$ is converted to kinetic energy of the initially stationary plasma $\frac{1}{2}\rho v_f^2$, where ρ is the mass density, and v_f the final flow velocity, then

$$v_f \approx \frac{B_i}{\sqrt{4\pi\rho}} = c_A, \tag{2.11}$$

where c_A is the Alfvén speed based on the initial magnetic field strength.

2.2.2 Steady-State Reconnection

Although these toy models are demonstrative, to determine quantitative results we must consider different theories of reconnection. Here we quantitatively treat the steady-state ($\partial/\partial t = 0$) reconnection process for both Sweet-Parker reconnection and Hall reconnection.

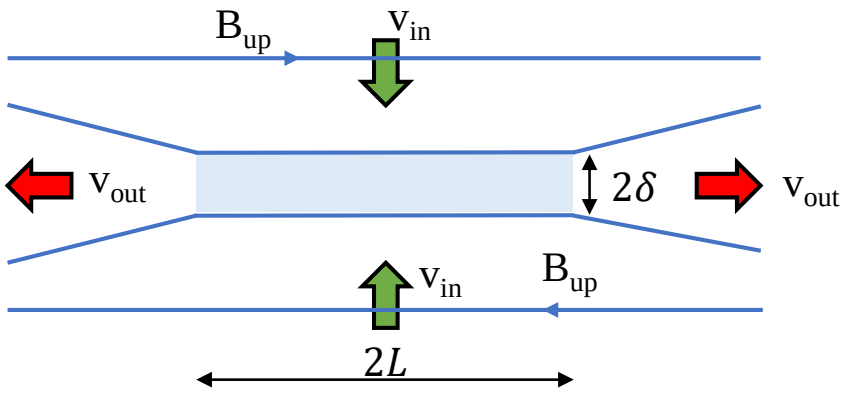

Figure 2.3: Sweet-Parker configuration. δ and L are the half-lengths of the diffusion region. The magnetic field upstream of the diffusion region, B_{up}, is pulled into the diffusion region in the direction of v_{in} and is then expelled outward in the direction of v_{out}.

2.2.2.1 Sweet-Parker Theory

Consider the Sweet-Parker configuration in Figure 2.3. δ and L are the half-lengths of the diffusion region, where $\delta \ll L$.

Reconnection is a nearly incompressible process, meaning the mass density ρ is constant. Thus, the continuity equation (Eq. 2.1) reduces to $\boldsymbol{\nabla} \cdot \mathbf{v} = 0$. This gives

$$\frac{v_{in}}{\delta} \sim \frac{v_{out}}{L} \implies v_{in} \sim \frac{\delta}{L} v_{out}, \tag{2.12}$$

where v_{in} and v_{out} are the inflow and outflow velocities, respectively. A similar result is obtained from Gauss' Law ($\boldsymbol{\nabla} \cdot \mathbf{B} = 0$):

$$\frac{B_{up}}{L} \sim \frac{B_{down}}{\delta} \implies B_{down} \sim \frac{\delta}{L} B_{up}, \tag{2.13}$$

where B_{up} and B_{down} are the magnetic fields upstream and (not depicted in Figure 2.3) downstream of the diffusion region.

Furthermore, by balancing the $\mathbf{v} \cdot \boldsymbol{\nabla}\mathbf{v}$ and $\mathbf{B} \cdot \boldsymbol{\nabla}\mathbf{B}$ terms in the modified momentum equation (Eq. 2.6) for the horizontal direction (neglecting the pressure gradient), we find

$$v_{out}^2 \sim \frac{B_{up}^2}{4\pi\rho} \sim c_{Aup}^2, \tag{2.14}$$

where c_{Aup} is the Alfvén speed based on the upstream magnetic field. This result is reminiscent of our result from the contracting island discussion (Eq. 2.11), as one might expect.

Next, we consider the reconnection rate. The reconnection electric field E (into the page in our configuration) is used for the reconnection rate. From the ideal Ohm's Law (Eq. 2.5, which holds outside the diffusion region),

$$E \sim \frac{v_{in} B_{up}}{c}. \tag{2.15}$$

The reconnection rate is usually presented in a normalized form E':

$$E' = \frac{cE}{v_{out} B_{up}}, \tag{2.16}$$

which simplifies to

$$E' \sim \frac{v_{in}}{v_{out}} \sim \frac{\delta}{L}. \tag{2.17}$$

Thus, to find the reconnection rate E', we must determine the inflow speed v_{in}. In Sweet-Parker reconnection, the mechanism for dissipation is electron-ion collisions, modifying the ideal Ohm's Law (Eq. 2.5) to

$$\mathbf{E} + \frac{\mathbf{v} \times \mathbf{B}}{c} = \eta \mathbf{J}, \tag{2.18}$$

where η is the resistivity. When this equation is used in combination with the rest of the equations describing ideal MHD (Eqs. 2.1-2.4) in lieu of the ideal Ohm's Law, this set of equations make up resistive-MHD. Substituting this into Equation 2.3 gives

$$\frac{\partial \mathbf{B}}{\partial t} = (\mathbf{B} \cdot \boldsymbol{\nabla})\, \mathbf{v} - (\mathbf{v} \cdot \boldsymbol{\nabla})\, \mathbf{B} + \frac{\eta c^2}{4\pi} \boldsymbol{\nabla}^2 \mathbf{B}. \tag{2.19}$$

Several of these terms may be neglected: along the symmetry line just upstream of the dissipation region, the first term on the right-hand side is zero, while the left-hand term is zero in steady state. Evaluated in the vertical direction for the configuration depicted in Figure 2.3, this gives

$$\frac{\eta c^2}{4\pi} \frac{B_{up}}{\delta^2} \sim \frac{v_{in} B_{up}}{\delta} \implies v_{in} \sim \frac{\eta c^2}{4\pi \delta}. \tag{2.20}$$

From Equation 2.17, the reconnection rate is thus

$$E' \sim \sqrt{\frac{\eta c^2}{4\pi} \frac{1}{c_A L}} \sim \frac{1}{\sqrt{S}}, \tag{2.21}$$

where S is the Lundquist number. In astrophysical systems, the Lundquist number is typically very large ($S = 10^9$ typically for solar flares), resulting in a very small reconnection rate. This is due to both a very small resistivity η of astrophysical plasmas and a very large length scale L, typically the size of the system [12, 40–42].

While the Sweet-Parker model is not sufficient to describe astrophysical phenomena, the scaling laws derived above are consistent with results from laboratory experiments [43, 44].

2.2.2.2 Non-Ideal Reconnection

The previous treatment was a fluid approach to reconnection. If kinetic effects are included, ideal MHD can break down when ions "decouple" from the electrons and the magnetic field lines. At small scales, ions and electrons gyrate around magnetic field lines, but as the ion mass is larger, their gyroradius is larger. If a magnetic field line is within one ion gyroradius of another field line, the ions are no longer constrained to their initial magnetic field line.

Several non-ideal terms are omitted from the ideal Ohm's Law. A generalized Ohm's Law can be derived from the electron equation of motion:

$$m_e \frac{d\mathbf{v}_e}{dt} = -\frac{1}{n}\boldsymbol{\nabla}\cdot\mathbb{P}_e - e\left(\mathbf{E} - \frac{\mathbf{v}_e \times \mathbf{B}}{c}\right) + m_e \nu_{ei}\left(\mathbf{v}_e - \mathbf{v}_i\right), \tag{2.22}$$

where m_e is the electron mass, $\mathbf{v}_e$ is the electron flow velocity, $\mathbb{P}_e$ is the electron pressure tensor, ν_{ei} is the electron-ion collision frequency, and $\mathbf{v}_i$ is the ion flow velocity. Using $\mathbf{J} = ne\left(\mathbf{v}_i - \mathbf{v}_e\right)$ to eliminate $\mathbf{v}_e$ and approximating

$$\frac{d\mathbf{v}_e}{dt} = \left(\frac{\partial}{\partial t} + \mathbf{v}_e \cdot \boldsymbol{\nabla}\right)\mathbf{v}_e \simeq \left(\frac{\partial}{\partial t} - \frac{\mathbf{J}}{ne}\cdot\boldsymbol{\nabla}\right)\left(-\frac{\mathbf{J}}{ne}\right), \tag{2.23}$$

we get

$$\mathbf{E} + \frac{\mathbf{v}_i \times \mathbf{B}}{c} = \eta\mathbf{J} + \frac{1}{nec}\mathbf{J}\times\mathbf{B} - \frac{1}{ne}\boldsymbol{\nabla}\cdot\mathbb{P}_e + \frac{m_e}{e^2}\frac{d\mathbf{J}/n}{dt}, \tag{2.24}$$

where $\eta = \nu_{ei} m_e / ne^2$ is the resitivity. The terms on the right-hand side are the resistive term, the Hall term, the electron pressure gradient term, and the electron

inertia term, respectively. When Equation 2.24 (without the rightmost two terms) is used in combination with the rest of the equations describing ideal MHD (Eqs. 2.1-2.4) in lieu of the ideal Ohm's Law (Eq. 2.5), this set of equations make up Hall-MHD. The resistive term, the off-diagonal electron pressure gradient term, and the electron inertia term can all violate the frozen-in theorem.

Because the ions are decoupled from the electrons and field lines, the diffusion region takes on a two-scale structure, with an ion diffusion region and a smaller electron diffusion region. The Hall term is important in both the ion and electron diffusion regions, leading to some substantial differences between Hall reconnection and Sweet-Parker reconnection. The Hall reconnection rate does not depend on the dissipation mechanism [15], nor does it depend on system size [45, 46]. The reconnection rate is a constant of order $E' \sim 0.1$ [45]. Thus, including kinetic effects avoids the major pitfalls of Sweet-Parker reconnection.

2.3 Asymmetric Reconnection

Thus far the discussion has been limited to symmetric reconnection, where the values of the magnetic fields, mass densities, and ion and electron temperatures are the same for the two inflowing plasmas. Magnetotail reconnection is often symmetric, while magnetopause reconnection is often asymmetric. There are a few significant differences between symmetric and asymmetric reconnection, which are discussed here.

2.3.1 Sweet-Parker Scaling Laws

Here, we derive Sweet-Parker scaling laws for asymmetric reconnection, first derived in [47] (which this section closely follows). These scaling laws are for anti-parallel reconnection.

It is convenient to rewrite the MHD equations in conservative form:

$$\frac{\partial \rho}{\partial t} = -\boldsymbol{\nabla} \cdot (\rho \mathbf{v}), \tag{2.25}$$

$$\frac{\partial (\rho \mathbf{v})}{\partial t} = -\boldsymbol{\nabla} \cdot \left[\rho \mathbf{v}\mathbf{v} + \left(P + \frac{B^2}{8\pi} \right) \mathbf{I} - \frac{\mathbf{B}\mathbf{B}}{4\pi} \right], \tag{2.26}$$

$$\frac{\partial \mathcal{E}}{\partial t} = -\boldsymbol{\nabla} \cdot \left[\left(\mathcal{E} + P + \frac{B^2}{8\pi} \right) \mathbf{v} - \frac{(\mathbf{v} \cdot \mathbf{B})}{4\pi} \mathbf{B} \right], \tag{2.27}$$

$$\mathbf{E} = -\frac{\mathbf{v} \times \mathbf{B}}{c} + \mathbf{R}, \tag{2.28}$$

along with Faraday's Law (Eq. 2.3). Here $\mathbf{I}$ is the unit tensor, $\mathcal{E} = \rho v^2/2 + P/(\gamma - 1) + B^2/8\pi$ is the total energy density, γ is the ratio of specific heats, and $\mathbf{R}$ stands for the remaining terms in the generalized Ohm's law. We write these equations in conservative form so that we may easily integrate these equations over a volume V for reconnection in a steady state, giving:

$$\oint_S d\mathbf{S} \cdot (\rho \mathbf{v}) = 0, \tag{2.29}$$

$$\oint_S d\mathbf{S} \cdot \left[\rho \mathbf{v}\mathbf{v} + \left(P + \frac{B^2}{8\pi} \right) \mathbf{I} - \frac{\mathbf{B}\mathbf{B}}{4\pi} \right] = 0, \tag{2.30}$$

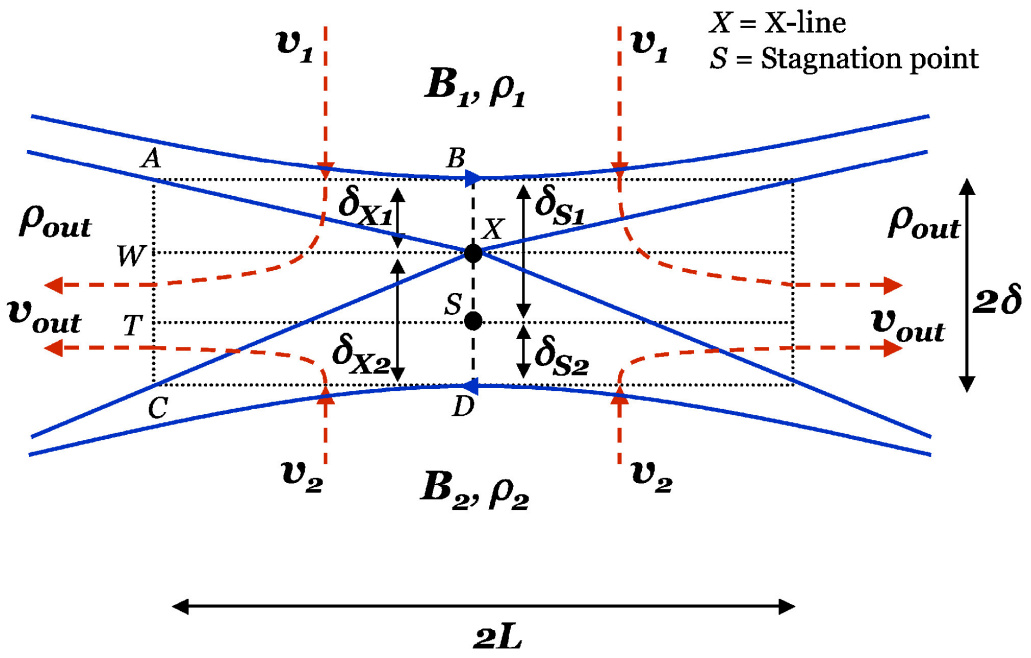

Figure 2.4: Asymmetric reconnection. The magnetic field lines are shown in blue, while the velocity lines are shown in red. B_1, ρ_1, and v_1 (B_2, ρ_2, and v_2) are the magnetic field, mass density, and bulk velocity upstream and above (below) the diffusion region. ρ_{out} and v_{out} are the density and bulk velocity in the outflow region. X and S are the locations of the X-line and stagnation point, respectively. Reprinted from Cassak & Shay, 2007 [47]

$$\oint_S d\mathbf{S} \cdot \left[\left(\mathcal{E} + P + \frac{B^2}{8\pi} \right) \mathbf{v} - \frac{(\mathbf{v} \cdot \mathbf{B})}{4\pi} \mathbf{B} \right] = 0, \tag{2.31}$$

where S is the surface of V. From Faraday's Law (and using Stokes' Theorem), we get

$$\oint_S d\mathbf{S} \times \mathbf{E} = 0. \tag{2.32}$$

These equations are used to analyze the reconnection event depicted in Figure 2.4. B_1, ρ_1, and v_1 are the magnetic field, mass density, and bulk velocity upstream and above the diffusion region, while B_2, ρ_2, and v_2 are those parameters upstream

and below the diffusion region. ρ_{out} and v_{out} are the density and bulk velocity in the outflow region. As before, δ and L are the half-lengths of the diffusion region.

The continuity equation (Eq. 2.29) gives

$$L\left(\rho_1 v_1 + \rho_2 v_2\right) \sim 2\delta\left(\rho_{out} v_{out}\right), \tag{2.33}$$

while the energy equation (Eq. 2.31) gives

$$L\left(\frac{B_1^2}{8\pi} v_1 + \frac{B_2^2}{8\pi} v_2\right) \sim 2\delta\left(\frac{1}{2}\rho_{out} v_{out}^2\right) v_{out}. \tag{2.34}$$

Here we assume the thermal pressure does not contribute to energy conversion. Lastly, Faraday's Law (Eq. 2.32) gives

$$v_1 B_1 \sim v_2 B_2 \tag{2.35}$$

when used in conjunction with Eq. 2.28.

Dividing Eq. 2.34 by Eq. 2.33 and using Eq. 2.35, we find

$$v_{out}^2 \sim \frac{B_1 B_2}{4\pi} \frac{B_1 + B_2}{\rho_1 B_2 + \rho_2 B_1}. \tag{2.36}$$

In the symmetric limit ($B_1 = B_2 = B_{up}$ and $\rho_1 = \rho_2 = \rho$), this simplifies to the upstream Alfvén speed c_{Aup}, as in Eq. 2.14. The (un-normalized) reconnection rate E can also be found with Eq. 2.34:

$$E \sim \left(\frac{\rho_{out} B_1 B_2}{\rho_1 B_2 + \rho_2 B_1}\right) \frac{v_{out}}{c} \frac{2\delta}{L}. \tag{2.37}$$

If we assume ρ_{out} scales like the mass density of a flux tube, it is straightforward to find

$$\rho_{out} \sim \frac{\rho_1 B_2 + \rho_2 B_1}{B_1 + B_2}, \tag{2.38}$$

which simplifies our expression for the outflow velocity (Eq. 2.36) to

$$v_{out}^2 \sim \frac{B_1 B_2}{4\pi\rho_{out}} \tag{2.39}$$

and the reconnection rate (Eq. 2.37) to

$$E \sim \left(\frac{2B_1 B_2}{B_1 + B_2}\right) \frac{v_{out}}{c} \frac{\delta}{L}. \tag{2.40}$$

Thus the outflow velocity is similar to an Alfvén velocity based on the geometric mean of the upstream fields and density of the outflow, while the reconnection rate depends on an effective magnetic field strength, the outflow velocity, and the aspect ratio of the dissipation region.

2.3.2 X-point vs Stagnation point

Another significant difference between asymmetric and symmetric reconnection is the difference in location of the magnetic X-point (where the magnetic field in the reconnection plane goes to zero) and the stagnation point (where the fluid velocity goes to zero). There is thus a net flow of plasma across the X-point in asymmetric reconnection, as we will see below.

We can calculate the relative position of the X-point and stagnation point thusly. As in Figure 2.4, δ_{X1} and δ_{X2} are the distances from the top and bottom of the dissipation region to the X-point X, while δ_{S1} and δ_{S2} are the distances from the top and bottom to the stagnation point S. To find δ_{X1} (δ_{X2}) we consider the energy equation (Eq. 2.31) for the rectangle $ABXW$ ($WXDC$). As WX is the neutral line, the magnetic energy through it is zero. The flow energy across the neutral line

is negligible, and there is no magnetic energy flow across BX (XD) by symmetry. For $ABXW$ we find

$$L\left(\frac{B_1^2}{8\pi}\right)v_1 \sim \delta_{X1}\left(\frac{1}{2}\rho_{out}v_{out}^2\right)v_{out}, \tag{2.41}$$

while $WXDC$ gives

$$L\left(\frac{B_2^2}{8\pi}\right)v_2 \sim \delta_{X2}\left(\frac{1}{2}\rho_{out}v_{out}^2\right)v_{out}. \tag{2.42}$$

By dividing Eq. 2.42 by Eq. 2.41 and using Eq. 2.35, we find

$$\frac{\delta_{X2}}{\delta_{X1}} \sim \frac{B_2}{B_1}. \tag{2.43}$$

Physically, this means the X-point is offset toward the inflow region with the weaker magnetic field.

To find δ_{S1} (δ_{S2}), we consider the continuity equation (Eq. 2.29) for the rectangle $ABST$ ($TSDC$). Mass flux across ST is zero by definition, while it is zero across BS (SD) by symmetry. For $ABST$ we find

$$L\left(\rho_1 v_1\right) \sim \delta_{S1}\left(\rho_{out}v_{out}\right), \tag{2.44}$$

while $TSDC$ gives

$$L\left(\rho_2 v_2\right) \sim \delta_{S2}\left(\rho_{out}v_{out}\right). \tag{2.45}$$

As before, dividing Eq. 2.45 by Eq. 2.44 and using Eq. 2.35, we find

$$\frac{\delta_{S2}}{\delta_{S1}} \sim \frac{\rho_2 B_1}{\rho_1 B_2}. \tag{2.46}$$

Thus the stagnation point is offset towards the side with smaller ρ/B. The X-point and stagnation point may still coincide, but they generally will not. In the case of symmetric reconnection, Eqs. 2.43 and 2.46 simplify to $\delta_{X1} \sim \delta_{X2}$ and $\delta_{S1} \sim \delta_{S2}$ [1].

[1] As $\delta_{X1} + \delta_{X2} = 2\delta = \delta_{S1} + \delta_{S2}$, in symmetric reconnection these values are all equal.

2.4 Numerical Simulations

The asymmetric reconnection simulations described in this thesis use the kinetic Particle-in-Cell (PIC) code `p3d` [48]. PIC simulations in three dimensions are computationally expensive, so several parameters utilized are smaller than realistic values to ease this expense. Using a smaller ion to electron mass ratio lessens the difference between ion and electron scales, though a ratio of $m_i/m_e = 25$ is generally sufficient to separate the two scales. The simulations presented here primarily use $m_i/m_e = 100$. Reducing the ratio of the electron plasma frequency ω_{pe} to electron cyclotron frequency ω_{ce} (also equal to c/c_{Ae}) lessens the difference between light waves and plasma waves. In most of our simulations, $\omega_{pe}/\omega_{ce} = 1.5$ and 0.3 in the asymptotic magnetosheath and magnetopause respectively, as compared to the more realistic values of 35 and 6, respectively.[2] Additionally, the ratio of the Debye length λ_D to the electron inertial length $d_e = c/\omega_{pe}$[3] is controlled by the choice of c/c_{A0} (where c_{A0} is defined below), which is chosen to be smaller than its realistsic value for resolution purposes. While reconnection generally does not depend on the Debye length, as the kinetic scales that control reconnection are d_e and the ion inertial length $d_i = c/\omega_{pi}$, instabilities such as the Buneman instability [49, 50] do. The instability analyzed in Chapters 4-6 has a much longer wavelength than λ_D, so the artificial Debye length does not appear to impact our results.

In addition, several code parameters must be chosen with care such that both

[2] While this seems to imply $c_{Ae} > c$, the wave speed plateaus before reaching c.

[3] λ_D/d_e is also equal to v_e/c, where $v_e = \sqrt{2T_e/m_e}$ is the electron thermal velocity.

small and large scale dynamics are properly captured. For large-scale dynamics, the system size L must be much larger than the ion inertial length d_i, and the simulation must run much longer than the ion cyclotron time ω_{ci}^{-1}. For small-scale dynamics, the grid spacing must be small enough to resolve the Debye length λ_D, the electron inertial length d_e and the Larmor radius ρ_x (where x can refer to either particle species). Not only does this ensure that small-scale physics are represented, it stabilizes a strong numerical instability resulting in artificial electron heating that occurs when the Debye length is unresolved [51]. Additionally, the time-step utilized must be small enough to resolve both ω_{pe} and ω_{ce} while also satisfying the Courant-Friedrichs-Lewy (CFL) condition [52], which requires any velocity seen in the simulation to satisfy $v < \Delta x/\Delta t$, where Δx is the grid spacing and Δt is the timestep used.

`p3d` is normalized such that most of the code variables are of order 1. A nominal magnetic field strength B_0 and density n_0 define the Alfvén speed $c_{A0} = \sqrt{B_0^2/4\pi m_i n_0}$, which is used to normalize the velocity. Lengths are normalized to the ion inertial length $d_i = c/\omega_{pi}$, where $\omega_{pi} = \sqrt{4\pi n_0 e^2/m_i}$ is the ion plasma frequency. Times are normalized to the ion cyclotron time $\omega_{ci0}^{-1} = m_i c/eB_0$. Electric fields are normalized to $c_{A0}B_0/c$, while temperatures are normalized to $m_i c_{A0}^2$. While most results are presented in these normalized units, some are converted to real units to better compare with MMS data.

Our simulations employ periodic boundary conditions in all directions. Since the reconnecting component of the magnetic field changes signs at a current sheet, there must be an even number of current sheets present in the system so that the

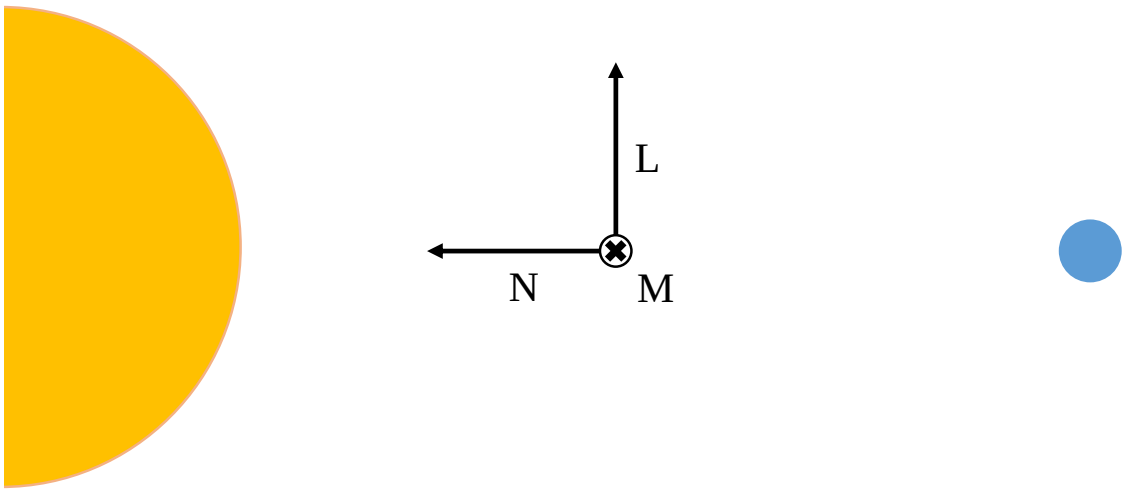

Figure 2.5: The LMN coordinate system. The sun and Earth (not to scale) are shown for reference. L is roughly north-south, in the direction of the reconnecting magnetic field. N is radial, in the inflow direction, while M is perpendicular to L and N.

reconnecting magnetic field matches polarity at the boundary. We use two current sheets that are treated independently, and all analysis is performed before the two current sheets become strongly correlated and merge with each other.

We use the LMN coordinate system, illustrated in Figure 2.5, in which L is in the direction of the reconnecting magnetic field (roughly north-south), N is in the inflow direction (roughly radial), and M is perpendicular to L and N in the out-of-plane direction (roughly azimuthal). To mimic the asymmetric conditions observed by MMS, the particle density n, reconnecting field component B_L, and

ion temperature T_i are initialized as functions of N with hyperbolic tangent profiles of width 1. The simulations are initially in asymptotic pressure balance but not precisely an exact equilibrium. Any evolution caused by the difference from an exact equilibrium is minor before reconnection develops.

Chapter 3: The Lower-Hybrid Drift Instability

In this chapter, I discuss an instability commonly seen in the presence of pressure gradients (which are commonly observed in asymmetric reconnection), the lower-hybrid drift instability (LHDI). I discuss drift waves in general before covering the general physics behind LHDI. I then derive a local dispersion relation for LHDI, finding the frequency and growth rate in the cold electron limit. Finally, I discuss numerical results for both the canonical LHDI and a longer wavelength LHDI mode.

3.1 Drift Waves

Asymmetric reconnection involves differences between the magnetic fields, densities, and temperatures for the two inflowing plasmas. The large gradients associated with these asymmetries are susceptible to the generation of drift waves and their associated instabilities. Drift waves control plasma transport across magnetic field lines and are driven unstable by steep gradients. We are interested in situations where these ambient gradients have scale lengths of the order of the ion Larmor radius ρ_i, and the associated drift waves have frequencies between the ion and electron cyclotron frequencies $\omega_{ci} \leq \omega \leq \omega_{ce}$. Drift waves are commonly associated with the $E \times B$ drift and the diamagnetic drift. These drifts may be easily derived from the

plasma momentum equation

$$mn\frac{d\mathbf{v}}{dt} = nq\left(\mathbf{E} + \frac{\mathbf{v}}{c} \times \mathbf{B}\right) - \boldsymbol{\nabla} P, \tag{3.1}$$

where m is the particle mass, n is the particle density, q is the particle charge, $\mathbf{v}$ is the plasma flow velocity, $\mathbf{E}$ is the electric field, $\mathbf{B}$ is the magnetic field, and P is the pressure scalar. We solve for $\mathbf{v}_\perp$ (the component of $\mathbf{v}$ perpendicular to $\mathbf{B}$) in the steady state, giving

$$\mathbf{v}_\perp = c\frac{\mathbf{E} \times \mathbf{B}}{B^2} + \frac{c}{nq}\frac{\mathbf{B} \times \boldsymbol{\nabla} P}{B^2}. \tag{3.2}$$

The first term on the right-hand side corresponds to the $E \times B$ drift, while the second term on the right-hand side describes the diamagnetic drift. Both are illustrated in Figure 3.1 [53]. In this simplified picture there are no temperature gradients, so using $P = nT$, the diamagnetic drift term becomes $cT\left(\mathbf{B} \times \boldsymbol{\nabla} n\right)/nqB^2$. The solid red line is at constant density, with regions of higher density to the left and lower density to the right of the solid line. There is a magnetic field B out of the page. The electrons flow from regions of higher density to lower density, creating an electric field E (black in the figure). This electric field results in an $E \times B$ drift, displayed in green in the figure. This drift pulls the line of constant density (in the directions indicated by the green arrows) to the red dotted line. By comparing the solid and dotted red lines, this wave appears to travel in the $-\mathbf{B} \times \boldsymbol{\nabla} n$ direction, where the negative sign is a result of the negative charge value. While drift waves are linearly stable, instabilities occur due to non-ideal effects.

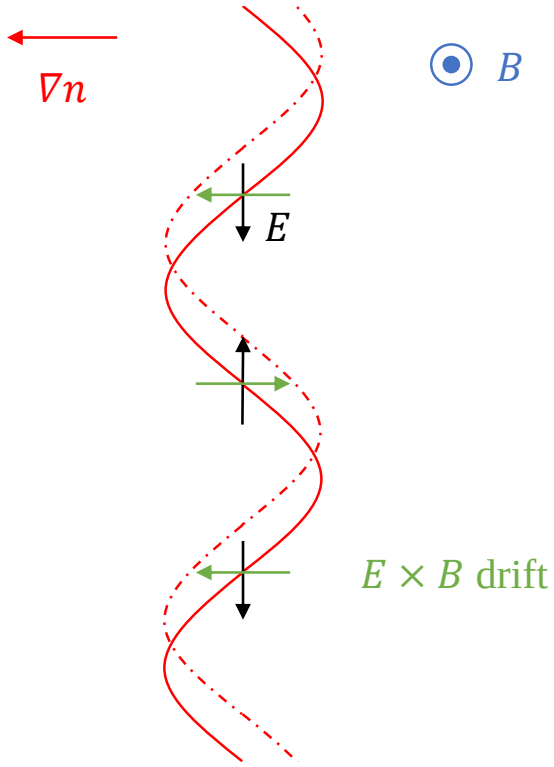

Figure 3.1: A physical interpretation of drift waves. The solid red line is at constant density, with a density gradient pointing to the left. Electrons flow from regions of high density to low density, creating the electric field E (black). The resulting $E \times B$ drift (green) pulls the (solid red) line of constant density to the dotted red line. The wave appears to travel in the $-\mathbf{B} \times \boldsymbol{\nabla} n$ direction.

3.2 The Physics Behind LHDI

The LHDI is driven by inhomogeneities in the magnetic field and plasma pressure. These inhomogeneities drive the relative drift of the electrons and ions. Before delving into the full LHDI dispersion relation, we examine simple scaling arguments. To lowest order, we assume the frequency of this instability $\omega \sim k v_{di}$, where k is the wavevector, $v_{di} = v_i \rho_i / L_p$ is the ion diamagnetic velocity, L_p is the pressure scale length, $v_i = \sqrt{2T_i/m_i}$ is the ion thermal velocity, $\rho_i = v_i/\omega_{ci}$ is the ion Larmor radius, and $\omega_{ci} = eB/m_i c$ is the ion cyclotron frequency. Then

$$\omega \sim k v_{di} \sim k v_i \frac{\rho_i}{L_p} \sim k v_i \sim \frac{v_i}{\rho_e} \sim \frac{v_i}{v_e}\omega_{ce} \sim \sqrt{\frac{m_e}{m_i}}\omega_{ce} \sim \sqrt{\omega_{ce}\omega_{ci}}. \tag{3.3}$$

Here, we have made the assumptions T_e and T_i are comparable, $L_p \sim \rho_i$ and $k\rho_e \sim 1$, where $\rho_e = v_e/\omega_{ce}$ is the electron Larmor radius, $v_e = \sqrt{2T_e/m_e}$ is the electron thermal velocity, and $\omega_{ce} = eB/m_e c$ is the electron cyclotron frequency. Thus the frequency is approximately the hybrid of the cyclotron frequencies.

To demonstrate basic properties of LHDI, we now derive a simplified dispersion relation. We express variables as equilibrium parts (with subscript 0) and perturbation parts (with subscript 1), such that $n_j = n_{j0} + n_{j1}$, $\mathbf{v}_j = \mathbf{v}_{j0} + \mathbf{v}_{j1}$, and $\mathbf{E} = \mathbf{E}_1$, where j is the particle species (e for electrons, i for ions) and we assume $\mathbf{E}_0 = 0$ and $n_{j0} = n_{j0}(y)$. The plasma equilibrium has $\mathbf{B} = B_0\hat{\mathbf{z}}$. LHDI is defined as having $\mathbf{k} \cdot \mathbf{B} = 0$, so for simplicity we assume $\mathbf{k} = k\hat{\mathbf{x}}$. Additionally, LHDI is canonically an electrostatic wave with $\mathbf{k} \times \mathbf{E} = 0$, so we assume $\mathbf{E}_1 = E_1\hat{\mathbf{x}}$. We are looking for an instability with frequency $\omega_{ci} \leq \omega \leq \omega_{ce}$, so we assume electrons are magnetized

but the ions are not. Lastly, we assume perturbed quantities are of the form

$$f(\mathbf{x},t) = f\exp\left[i\left(kx-\omega t\right)\right] \tag{3.4}$$

where $\mathrm{Im}(\omega) > 0$.

We consider the ion momentum equation (Eq. 2.2). To zeroth order in the steady state, we find

$$0 = \frac{e}{c}\mathbf{v}_{i0}\times\mathbf{B} - \boldsymbol{\nabla}P \tag{3.5}$$

which gives

$$v_{i0} = -\frac{c}{eB_0}\frac{\partial P_i}{\partial y} = v_{di} \tag{3.6}$$

in the x-direction. We move to the rest frame of the ions, where the frequency is modified to $\overline{\omega} \equiv \omega - kv_{di}$. Then to first order, the continuity equation (Eq. 2.1) gives

$$-i\overline{\omega}n_{i1} + ikn_{i0}v_{i1} = 0, \tag{3.7}$$

and the momentum equation gives

$$-i\overline{\omega}m_i v_{i1} = en_{i0}E_1. \tag{3.8}$$

Combining Equations 3.7 and 3.8 gives

$$\frac{n_{i1}}{n_{i0}} = i\frac{ke}{m_i\overline{\omega}^2}E_1. \tag{3.9}$$

We assume the electrons are cold, $\mathbf{v}_{e0} = 0$, and the particles drift with speed $\mathbf{v}_{e1} = v_E\hat{\mathbf{y}} + v_p\hat{\mathbf{x}}$, where $v_E = -cE_1/B_0$ is the $E\times B$ drift and $v_p = -c(dE_1/dt)/(\omega_{ce}B_0)$[1] is the polarization drift. Then the continuity equation (Eq.

[1] v_p may be found by substituting $\mathbf{v}_\perp = v_E + v_p$ into $m\frac{d}{dt}\mathbf{v}_\perp = q\left(\mathbf{E} + \mathbf{v}_\perp\times\mathbf{B}/c\right)$ and matching terms, where we assume $\frac{d}{dt}v_p$ is small.

2.1) gives

$$-i\omega n_{e1} - ikn_{e0}\frac{(-i\omega)}{\omega_{ce}}\frac{c}{B_0}E_1 - \left(\frac{\partial n_{e0}}{\partial y}\right)\frac{c}{B_0}E_1 = 0. \tag{3.10}$$

Dividing by $-i\omega n_{e0}$ and defining $1/L_n \equiv -(1/n_{e0})\partial n_{e0}/\partial y$, we get

$$\frac{n_{e1}}{n_{e0}} - i\frac{k}{\omega_{ce}}\frac{c}{B_0}E_1 + i\frac{1}{\omega L_n}\frac{c}{B_0}E_1 = 0. \tag{3.11}$$

The plasma approximation requires $n_i = n_e$, so we substitute Equation 3.9 for n_{e1}/n_{e0}; with some simplification we obtain

$$\frac{\Omega_{\rm lh}^2}{\overline{\omega}^2} - 1 + \frac{\Omega_{\rm lh}^2}{\omega_{ce}\omega}\frac{1}{kL_n} = 0, \tag{3.12}$$

where we have used $\Omega_{\rm lh} = \sqrt{\omega_{ce}\omega_{ci}}$. If we assume the $1/kL_n$ term is small compared to the others and that ω is small compared to kv_{di} (so $\overline{\omega} \approx -kv_{di}$), we find

$$\frac{\Omega_{\rm lh}^2}{k^2 v_{di}^2} \approx 1, \tag{3.13}$$

or $kv_{di} \approx \pm\Omega_{\rm lh}$. Keeping corrections gives

$$\frac{\Omega_{\rm lh}^2}{k^2 v_{di}^2\left(1 - \frac{\omega}{kv_{di}}\right)^2} - 1 + \frac{\Omega_{\rm lh}^2}{\omega_{ce}\omega}\frac{1}{kL_n} = 0, \tag{3.14}$$

which becomes

$$1 + 2\frac{\omega}{kv_{di}} - 1 + \frac{\Omega_{\rm lh}^2}{\omega_{ce}\omega}\frac{1}{kL_n} = 0 \tag{3.15}$$

when we use $k^2 v_{di}^2 = \Omega_{\rm lh}^2$ and Taylor expand $(1 - \omega/kv_{di})^{-2}$. Finally this gives

$$\omega^2 = -\frac{1}{2}\frac{\Omega_{\rm lh}^2 v_{di}}{\omega_{ci}L_n}, \tag{3.16}$$

which requires $v_{di}/\omega_{ci}L_n < 1$. As $\omega^2 < 0$, ω is imaginary, which leads to an instability.

These two examples together demonstrate the main properties of LHDI: $k\rho_e \sim 1$, $\omega \sim kv_{di} \sim \sqrt{\omega_{ce}\omega_{ci}}$, $\mathbf{k}\cdot\mathbf{B} = 0$, and LHDI is electrostatic.

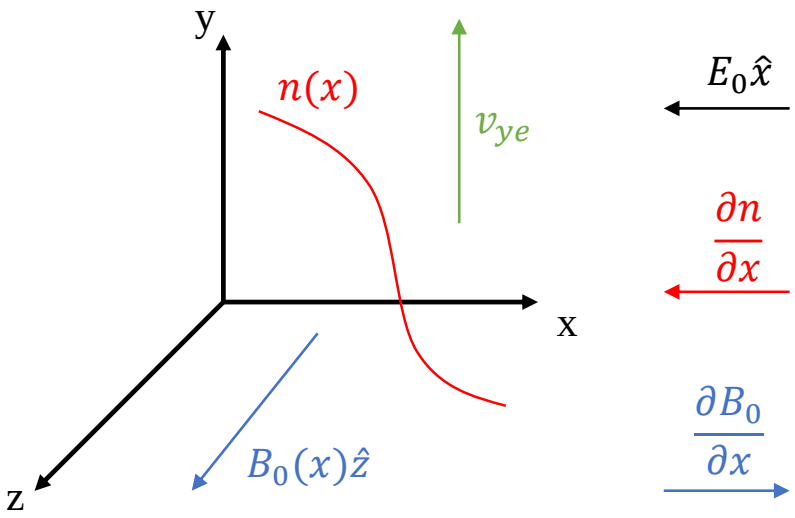

Figure 3.2: The background plasma configuration. n and $\mathbf{B}_0$ vary with respect to x, while $\mathbf{E}_0$ is constant. The electrons drift in the $+y$ direction with velocity v_{ye}.

3.3 Dispersion Relation Analysis

In Appendix A we more carefully derive a full dispersion relation for the LHDI. It is useful to describe the background plasma configuration this derivation is based on, depicted in Figure 3.2.

The magnetic field $\mathbf{B}_0 = B_0(x)\hat{\mathbf{z}}$ and density $n(x)$ vary with respect to x, while the electric field $\mathbf{E}_0 = -E_0\hat{\mathbf{x}}$ is constant. The particles of species j (e for electrons, i for ions) drift with speed $v_{yj} = v_E + v_{dj}$, where

$$v_E = cE_0/B_0 \tag{3.17}$$

is the $E \times B$ drift and

$$v_{dj} = \mathrm{sgn}(q_j) \frac{T_j}{m_j \omega_{cj}} \frac{\partial}{\partial x} \ln (nT_j) \tag{3.18}$$

is the particle diamagnetic drift, with $n = n_e(x) = n_i(x)$ the density, $T_j(x)$ the particle temperature, m_j the particle mass, and $\omega_{cj} = |q_j| B_0/m_j c$ the particle cyclotron frequency.

3.3.1 Dispersion Relation

From this configuration we derive the dispersion relation in Appendix A, the result of which is

$$\left(1 + \frac{2\omega_{pe}^2}{c^2 k_y^2} \Phi_1\right) \left[1 + \frac{2\omega_{pi}^2}{k_y^2 v_i^2} (1 + \xi_i Z(\xi_i)) + \frac{2\omega_{pe}^2}{k_y^2 v_e^2} (1 - \Phi_3)\right] = -\frac{2\omega_{pe}^2}{c^2 k_y^2} \frac{2\omega_{pe}^2}{k_y^2 v_e^2} \Phi_2^2, \tag{3.19}$$

where

$$\Phi_1 = \frac{2}{v_e^4} \int_0^\infty dv_\perp \frac{v_\perp^3 [J_0'(\mu)]^2 \exp(-v_\perp^2/v_e^2)}{\omega - k_y v_E - k_y v_B} \Lambda, \tag{3.20}$$

$$\Phi_2 = \frac{2}{v_e^3} \int_0^\infty dv_\perp \frac{v_\perp^2 J_0(\mu) J_0'(\mu) \exp(-v_\perp^2/v_e^2)}{\omega - k_y v_E - k_y v_B} \Lambda, \tag{3.21}$$

$$\Phi_3 = \frac{2}{v_e^2} \int_0^\infty dv_\perp \frac{v_\perp J_0^2(\mu) \exp(-v_\perp^2/v_e^2)}{\omega - k_y v_E - k_y v_B} \Lambda, \tag{3.22}$$

$Z(\xi)$ is the plasma dispersion function

$$Z(\xi) = \frac{1}{\sqrt{\pi}} \int_{-\infty}^\infty dx \frac{\exp(-x^2)}{x - \xi}, \tag{3.23}$$

$\xi_i = (\omega - k_y v_{yi}) / k_y v_i, \Lambda = \omega - k_y v_E - k_y v_n + k_y v_T (1 - v_\perp^2/v_e^2), v_\perp^2 = v_x^2 + (v_y - v_E)^2, J_0(\mu)$ is the Bessel function of the first kind of order 0, $J_0'(\mu) = dJ_0(\mu)/d\mu, \mu = k_y v_\perp/\omega_{ce}, v_B =$

$-\epsilon_B v_\perp^2/2\omega_{ce}, \omega_{pe}^2 = 4\pi ne^2/m_e$ is the electron plasma frequency, $\omega_{pi}^2 = 4\pi ne^2/m_i$ is the ion plasma frequency, $v_n = -(T_e/m_e\omega_{ce})\epsilon_n, v_T = -(T_e/m_e\omega_{ce})\epsilon_T, \epsilon_n = (1/n)\partial n/\partial x = \partial(\ln n)/\partial x$ is the inverse length scale of the density, $\epsilon_T = (1/T_e)\partial T_e/\partial x = \partial(\ln T_e)/\partial x$ is the inverse length scale of the temperature, and $\epsilon_B = (1/B_0)\partial B_0/\partial x = \partial(\ln B_0)/\partial x$ is the inverse length scale of the magnetic field.

This dispersion relation cannot be solved analytically except in limiting cases.

3.3.2 Cold Electron Limit

One such limiting case is the cold electron limit. If we assume $T_e \ll T_i$ and $\epsilon_T = 0$, we find that Eqns. 3.20, 3.21, and 3.22 become

$$\Phi_1 = 0, \tag{3.24}$$

$$\Phi_2 = \frac{1}{2}\frac{k_y v_e}{\omega_{ce}}, \tag{3.25}$$

and

$$\Phi_3 = 1 - \frac{1}{2}\left(\frac{k_y v_e}{\omega_{ce}}\right)^2 + \frac{k_y\left(v_n - v_B\right)}{\omega - k_y v_E}. \tag{3.26}$$

Substituting these quantities into Eqn. 3.19 gives

$$1 + \frac{2\omega_{pi}^2}{k_y^2 v_i^2}\left[1 + \xi_i Z(\xi_i)\right] + \frac{\omega_{pe}^2}{\omega_{ce}^2}\left(1 + \frac{\omega_{pe}^2}{c^2 k_y^2}\right) - \frac{k_y v_{di}}{\omega - k_y v_E}\frac{2\omega_{pi}^2}{k_y^2 v_i^2}\left(1 + \frac{\beta_i}{2}\right) = 0. \tag{3.27}$$

Here we have used $\epsilon_B = -(\beta_i/2)\epsilon_n$ from Eqn. A.9 to relate v_n and v_B.

In the low-drift-velocity limit, we approximate $Z(\xi_i) \simeq i\sqrt{\pi}k_y/|k_y|$. We also assume the ions carry no current, so $v_{yi} = v_E + v_{di} = 0$. Writing $\omega = \omega_r + i\gamma$, our

dispersion relation becomes

$$D(k_y, \omega_r + i\gamma) = 1 + \frac{k_M^2}{k_y^2}\left(1 - \frac{k_y v_{di}}{\omega_r + k_y v_{di} + i\gamma} + \frac{i\sqrt{\pi}}{1+\beta_i/2}\frac{\omega_r + i\gamma}{|k_y| v_i}\right), \tag{3.28}$$

where we have used

$$k_M^2 = \frac{2\omega_{pi}^2}{v_i^2}\frac{1+\beta_i/2}{1+\omega_{pe}^2/\omega_{ce}^2}. \tag{3.29}$$

The frequency ω_r can be found by assuming $|\omega_r| \gg |\gamma|$ and setting the real part of $D(k_y, \omega_r + i\gamma)$ to zero, giving

$$\omega_r = -k_y v_{di}\left(\frac{k_y^2}{k_y^2 + k_M^2}\right). \tag{3.30}$$

Similarly, the growth rate γ is found by setting the imaginary part of $D(k_y, \omega_r + i\gamma)$ to zero and using the newly found ω_r:

$$\gamma = \frac{\sqrt{\pi}}{1+\beta_i/2}\frac{k_y^2 v_{di}^2}{|k_y| v_i}\frac{k_y^2}{k_M^2}\left(\frac{k_M^2}{k_y^2 + k_M^2}\right)^3. \tag{3.31}$$

The growth rate γ is maximized at $k_y = \pm k_M$, giving a maximum growth rate of

$$\gamma_M = \frac{\sqrt{2\pi}}{8}\left(\frac{v_{di}}{v_i}\right)^2 \frac{1}{\sqrt{1+\beta_i/2}}\Omega_{\text{lh}} \tag{3.32}$$

and the corresponding frequency at maximum growth rate

$$\omega_M = \mp\sqrt{\frac{1+\beta_i/2}{2}}\left(\frac{v_{di}}{v_i}\right)\Omega_{\text{lh}}, \tag{3.33}$$

where we have used the lower-hybrid frequency Ω_{lh}, given by

$$\Omega_{\text{lh}}^2 = \frac{\omega_{pi}^2}{1+\omega_{pe}^2/\omega_{ce}^2}. \tag{3.34}$$

In the limit where $\omega_{pe} \gg \omega_{ce}$, $\Omega_{\text{lh}} \simeq \sqrt{\omega_{ce}\omega_{ci}}$, the hybrid of the cyclotron frequencies we obtained earlier.

3.4 Comparison to Numerical Studies

Numerical studies have shown that the fastest growing LHDI modes have $\mathbf{k} \cdot \mathbf{B} = 0$, $k\rho_e \sim 1$, $\gamma \lesssim \Omega_{\rm lh}$, and $\omega \sim k_y v_{di} \lesssim \Omega_{\rm lh}$ [54, 55]. The results derived above for the cold electron limit roughly match these conclusions. For example, when $\omega_{pe} \gg \omega_{ce}$ Equation 3.29 gives

$$k_y \rho_e \approx \sqrt{\frac{T_e}{T_i}\,(1 + \beta_i/2)}, \tag{3.35}$$

which matches $k_y\rho_e \sim 1$ for $T_e \approx T_i$ and $\beta_i \sim \mathcal{O}(1)$. This fastest growing electrostatic mode is localized on the edge of the current sheet, as it is stabilized by the high β within the sheet[2] [56–59].

There is numerical evidence for a longer-wavelength electromagnetic instability associated with LHDI [57,58,60]. If the current sheet is very narrow (with a width on the order of ρ_i), the fastest growing mode discussed previously saturates and a mode with $k\sqrt{\rho_e\rho_i} \sim 1$ develops. This mode can have a frequency between $\omega_{ci} \leq \omega \leq \Omega_{\rm lh}$, can penetrate the current sheet's center, and need not strictly satisfy $\mathbf{k} \cdot \mathbf{B} = 0$. This mode will be discussed further in Chapter 5.

[2] In the parameter regime considered here, high β reduces the maximum growth rate (as seen in Eqn. 3.32) but does not stabilize the instability. High β stabilization is discussed in the referenced papers, in which slightly different dispersion relations are derived.

Chapter 4: Simulations of the 16 October 2015 MMS Encounter

The first MMS data published was from an electron diffusion region encounter on 16 October 2015 [38]. This data shows two magnetopause crossings within approximately two minutes of each other. Several factors indicate that during this second crossing MMS entered the electron diffusion region (EDR). Figure 4.1 shows data from one of the MMS spacecraft. The magnetosphere is identified by the region of high magnetic field strength B and low plasma density n, while the magnetosheath is characterized by a population of hotter ions with a weaker B and higher n. The dissipation region has several indicators identified in the figure. First, around 13:07 UT there is a jet reversal as seen in v_{iL}. This occurs around the same time that the reconnecting magnetic field component B_L is nearly zero. Additionally, simulations indicate J_M should peak in the dissipation region, as the data indicates. Lastly, the reconnection electric field E_M has large bursts during the same time frame. These are all strong indicators that MMS encountered the electron diffusion region around 13:07 UT. At this time, the spacecraft were at $(X, Y, Z) = (8.30, 7.05, -4.82)R_e$ in geocentric solar magnetospheric coordinates [61].

One important result from this paper was the observation of crescent-shaped electron distribution functions, which had previously been predicted [62]. Figure 4.2

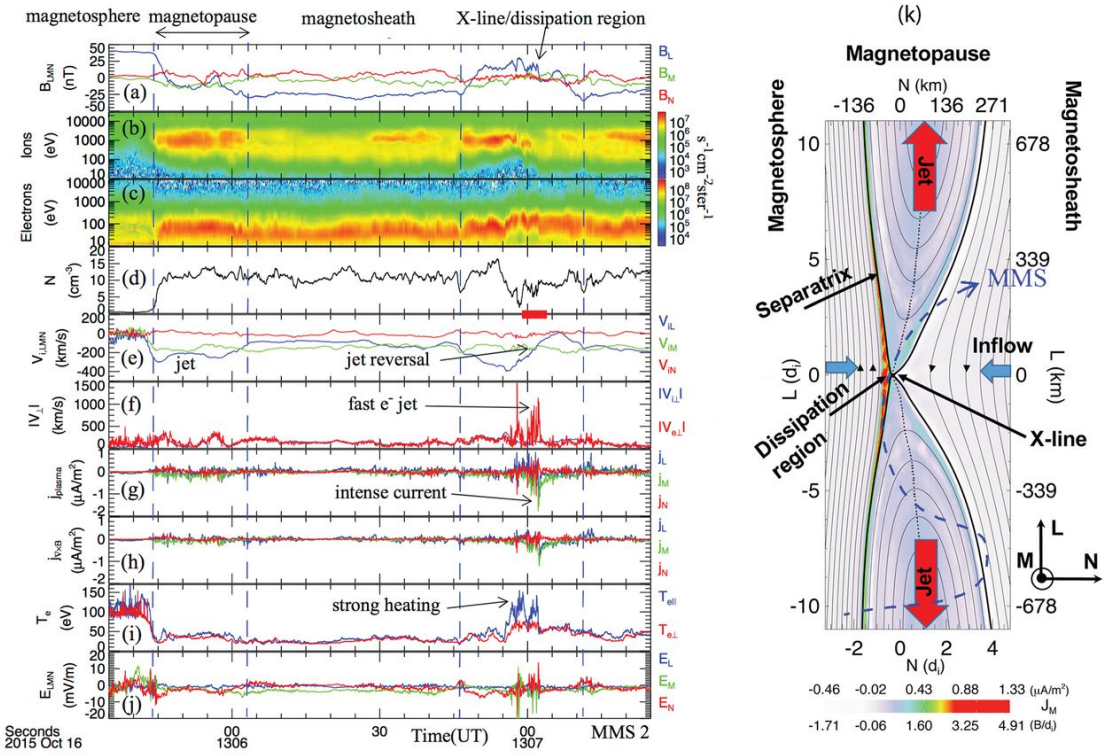

Figure 4.1: Data from MMS2. The two magnetopause crossings are indicated by the vertical blue dashed lines. Vector quantities use the (L, M, N) coordinate system introduced in Chapter 2. Panel data shows (a) the magnetic field in all three directions, (b-c) the energy-time spectrogram of ion and electron flux, respectively, (d) the plasma density, (e) ion flow velocity, (f) electron and ion convection velocities, (g-h) current computed from the particle velocities and $\nabla \times B$, respectively, (i) electron temperature, and (j) electric field. Panel (k) shows the spacecraft path from a simulation based on parameters from the crossing. From Burch et al., 2016 [38]. Reprinted with permission from AAAS.

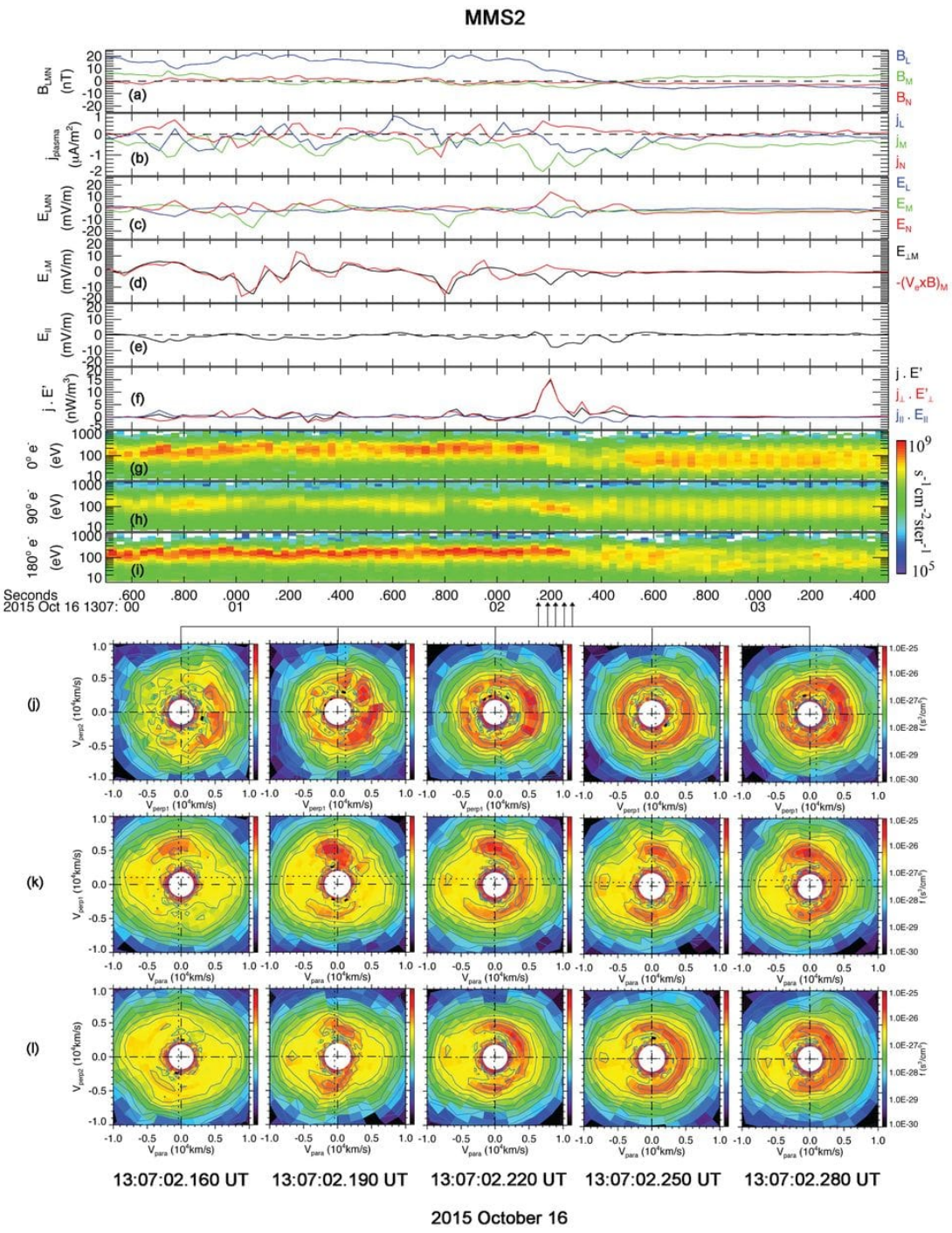

Figure 4.2: Data from MMS2 for approximately three seconds around the time of the electron diffusion region encounter. Panels show (a) the magnetic field, (b) current from plasma measurements, (c) the electric field, (d) M-component of $\mathbf{E}$ and $-(\mathbf{v}_e \times \mathbf{B})$, (e) $E_\parallel$. (f) $\mathbf{J} \cdot \mathbf{E}$, (g-i) electron energy-time spectrograms, and electron velocity-space distributions for (j) $(v_{\perp 1}, v_{\perp 2})$, (k) $(v_\parallel, v_{\perp 1})$, and (l) $(v_\parallel, v_{\perp 2})$. From Burch et al., 2016 [38]. Reprinted with permission from AAAS.

shows data from MMS2 for approximately three seconds around 13:07 UT. Panels (j-l) show electron velocity-space distribution functions in all three directions, where $v_\parallel$ is parallel to $\mathbf{b} = \mathbf{B}/|\mathbf{B}|$, $\mathbf{v}_{\perp 1} = (\mathbf{b} \times \mathbf{v}) \times \mathbf{b}$, and $\mathbf{v}_{\perp 2} = -\mathbf{v} \times \mathbf{b}$. The crescent-shaped distribution functions result from cusp-like motion of electrons in the $M-N$ plane controlled by both $B_L(N)$ and $E_N(N)$, as seen in Figure 4.3 [63,64]. E_N and B_L are assumed to be zero on the magnetosheath side and increase linearly with distance N into the magnetosphere. This electric field is an important component of asymmetric reconnection, caused by the stagnation point being displaced to the magnetosphere side of the X-line. An electron near the X-line (the dashed horizontal line) is accelerated toward the magnetosphere by E_N where B_L deflects it in the M direction. Ultimately the electron returns to the X-line only to repeat this cusp-like motion. It is conceivable that strong turbulence could scatter these electron orbits and prevent the formation of these crescent distributions, so it was originally hypothesized that the observations of these distributions indicated turbulence did not play an important role at the X-line.

Here we present two- and three-dimensional simulations of reconnection with initial conditions reflective of this MMS event.[1] Because of the extra freedom associated with dynamics in the dawn-dusk (M) direction, instabilities such as the lower-hybrid drift instability (LHDI) [66–69] or the electron Kelvin-Helmholtz instability [70] can develop. In contrast with the results of earlier simulations [66,69], we find that for the parameters associated with the MMS event, which has a larger jump in plasma density than had been previously treated, the turbulence signifi-

[1] The remainder of this chapter is based on Price et al., 2016 [65]

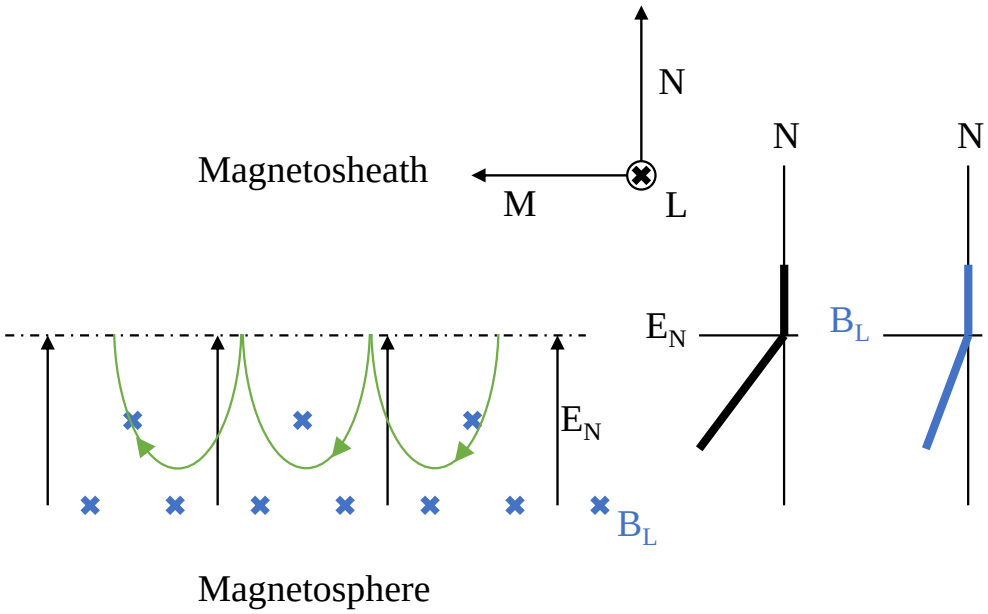

Figure 4.3: The cusp-like motion of electrons near the X-line. E_N and B_L are assumed to be zero on the magnetosheath side and increase linearly in the magnetosphere. Electrons near the X-line (the dashed horizontal line) are accelerated into the magnetosphere by E_N. B_L causes the electrons to deflect in the M direction until they completely reverse direction, returning to the X-line to repeat this motion. Figure adapted from Shay et al., 2016 [63].

Parameters	Magnetosheath		Magnetosphere	
	Measured	Normalized	Measured	Normalized
n	11.3 cm^{-3}	1.0	0.7 cm^{-3}	0.06
B_L	-23 nT	-1.0	39 nT	1.70
B_M	-2.278 nT	-0.099	-2.278 nT	-0.099
T_i	320 eV	1.37	2000 eV	7.73
T_e	28 eV	0.12	95 eV	1.28
ω_{pe}/ω_{ce}	35	1.5	6	0.3

Table 4.1: Parameters for the 16 Oct 2015 EDR encounter

cantly deforms the current layers and produces variations in the electromagnetic fields sufficiently strong to affect the structure of the diffusion region: anomalous resistivity and anomalous viscosity both play a role in breaking the frozen-in condition. (Interestingly, high-frequency electric field fluctuations, amplitude $\gtrsim$ 20 mV/m, were seen in the EDR during the MMS crossing.) However, in spite of the presence of turbulence in the simulations, crescents are still present in the electron distribution functions within the strong current layers on the magnetospheric edge of the diffusion region and separatrices. Thus, the role of turbulence in balancing Ohm's law remains an open issue in the MMS observations.

4.1 Simulation Descriptions

The initial conditions for the simulations closely mimic those observed by MMS during this diffusion region encounter. The particle density n, reconnecting field component B_L, and ion temperature T_i vary as a function of N with hyperbolic tangent profiles of width 1. The initial asymptotic values of n, B_L, and T_i are reported in Table 4.1. The guide field $B_M = 0.099$ is initially uniform. Temperatures are normalized to $m_i c_A^2 = 232.5$ eV. Pressure balance determines the magnetosphere electron temperature T_e, subject to the constraint that its asymptotic magnetosheath value is 0.12.[2]

We performed both two-dimensional and three-dimensional simulations with these parameters in the LMN coordinate system discussed in Section 2.4. For the two-dimensional simulation the domain had dimensions $(L_L, L_N) = (40.96, 20.48)$ and employed the same plasma parameters as that discussed in [38]. The three-dimensional simulation extended the M direction: $(L_L, L_M, L_N) = (40.96, 10.24, 20.48)$. The ion-to-electron mass ratio was set to 100, which is sufficient to separate the electron and ion scales. The spatial grid has a resolution $\Delta = 0.02$ while the smallest physical scale is the Debye length in the magnetosheath, ≈ 0.03. As in [38] we used 500 particles per cell per species when $n = 1.0$ for the two-dimensional simulation. Due to computational constraints, the three-dimensional simulation uses 50 particles per cell, which implies ≈ 3 particles per cell in the low-density magnetosphere. To

[2]For the stability of our simulations, it is more important for the initial conditions to be in pressure balance than it is for the temperatures to exactly match MMS values.

mitigate the resulting noise, our analysis of this case employs averages over multiple cells.

The velocity of light is $c = 15$ so that $\omega_{pe}/\Omega_{ce} = 1.5$ in the asymptotic magnetosheath and 0.3 in the asymptotic magnetosphere; the observed ratios are larger (≈ 35 and 6, respectively). As a result, the Debye length in the simulation is not as small as at the magnetopause and might artificially suppress very short wavelength electrostatic instabilities [71]. Unlike some earlier simulations of [66] we do not force the rate of reconnection with an external boundary condition; instead, the boundary conditions are periodic in all directions. Our initial profiles also differ from those earlier simulations (the density jump across the magnetopause being 16 rather than 10) since they have been chosen to match the event explored by MMS.

4.2 Turbulence and Chaotic Field Lines

Figure 4.4 displays images of J_{eM}, the dawn-dusk electron current density. Panels (a) and (b) show the $L - N$ plane for the two-dimensional and three-dimensional simulations after reconnection of roughly the same amount of magnetic flux. In both, the magnetosphere (strong field, low density) is to the left and the magnetosheath (weak field, high density) is to the right. As is typical in asymmetric configurations, the reconnection of equal amounts of flux from the two sides means the islands bulge into the magnetosheath. While the two-dimensional simulation is laminar, turbulence develops in the three-dimensional case. This can be clearly seen in panels (c) and (d), which show J_{eM} in cuts through the $M - N$ plane of the

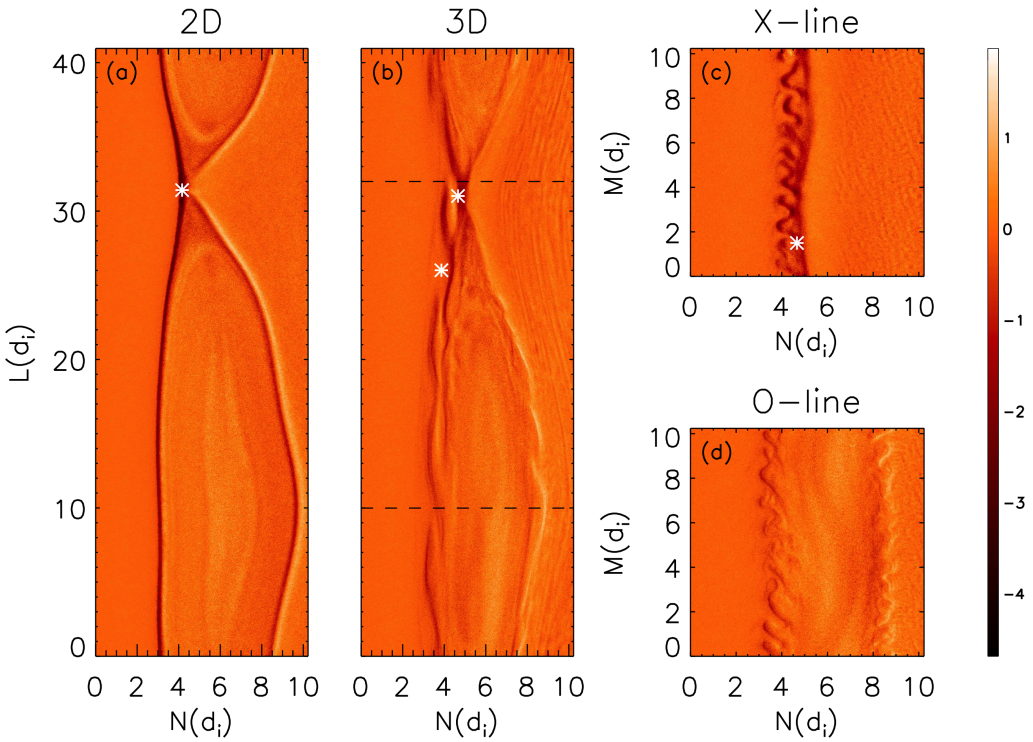

Figure 4.4: Snapshots of J_{eM}, the dawn-dusk electron current density. Panel (a): The $L-N$ plane from the two-dimensional simulation at $t = 40$. Panel (b): The $L-N$ plane from the three-dimensional simulation when roughly the same amount of flux has reconnected ($t = 30$). The two dashed lines denote the cuts shown in subsequent panels. Panel (c): The $M-N$ plane from a cut through the x-line, the upper line in panel (b). Panel (d): The $M-N$ plane from a cut through the island, the lower line in panel (b). In each panel the colors are separately normalized; the bar at the right shows the relative variation. The stars indicate the locations of the distribution functions presented in Figure 4.7.

simulation at the locations denoted by the dashed lines in panel (b). The current layers at both the x-line (panel (c)) and bordering the magnetic island (panel (d)) have become turbulent.

The free energy in the strong, spatially localized, out-of-plane electron flows are the likely drive for the instability. The wavelength is consistent with LHDI both near the x-line and on the separatrices during asymmetric reconnection. The energy source for the LHDI is the relative drift of the ions and electrons in the M direction and the wavevector satisfies the relation $\mathbf{k} \cdot \mathbf{B} = 0$ so that $\mathbf{k}$ is along M at the x-line and the midplane of the island. Thus, the LHDI does not develop in the two-dimensional simulation. Within the current layer, the range of excited wavenumbers is relatively broad, $(m_e/m_i)^{0.25} \lesssim k\rho_e \lesssim 1$, where ρ_e is the thermal electron Larmor radius [60]. For the parameters of our simulations, this can be written as a condition on the wavelength: $0.5 \lesssim \lambda/d_i \lesssim 2$. The fluctuations in the simulation fall within this range. On the other hand, the strong, localized electron drift seen in Figure 4.4 differs from systems usually analyzed for the LHDI instability and the electron Kelvin-Helmholtz instability [70] is also a possible driver for the turbulence. Note that while the instability has reached the non-linear stage by the time shown in panels (c) and (d), the structure at earlier times (not shown) exhibits similar spatial scales. The presence of strong turbulence around the x-line differs from the results of earlier three-dimensional simulations, where strong turbulence was largely localized away from the x-line along the separatrices. Chapter 5 is devoted to further analyzing this turbulence.

The flows driven by the instability are dominantly in the $M-N$ plane and twist

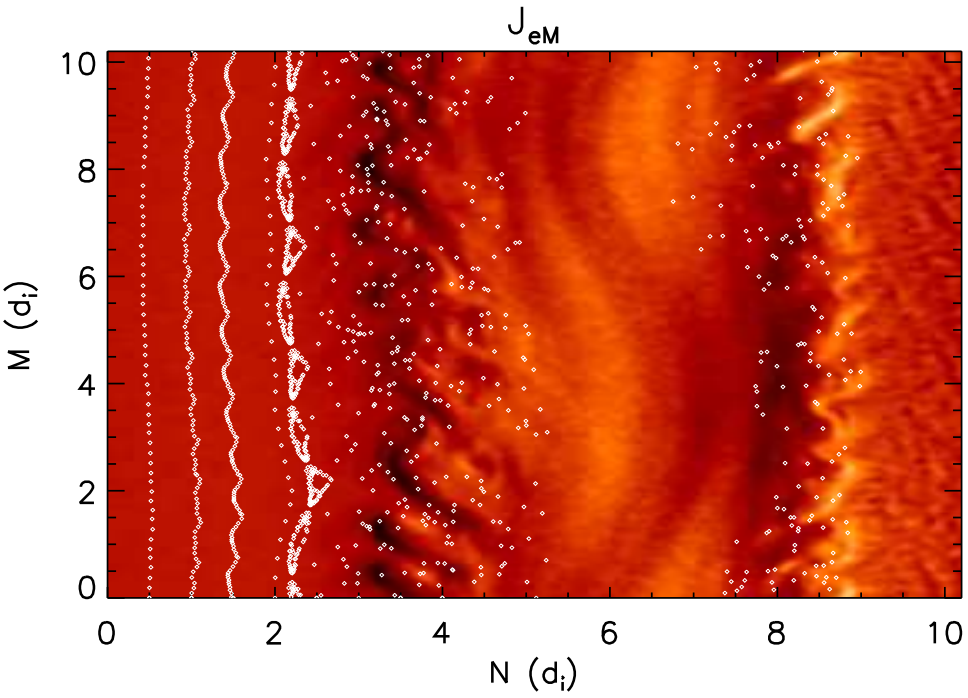

Figure 4.5: Puncture plot showing the intersections of field lines with panel (d) of Figure 4.4. Each dot represents the intersection of a field line with the plane after tracing its trajectory through the simulation domain. The islands at $N \approx 2.5$ mark the transition from laminar to turbulent behavior.

the dominant magnetic field (L direction) so that it develops M and N components. We emphasize, however, that the development of B_M and B_N is a conversion from flow to magnetic energy rather than the reverse. Nevertheless, the result is a chaotic magnetic field. Figure 4.5 shows the intersections of field lines with the $M-N$ plane at the midplane of the magnetic island with J_{eM} in the background. Because of the periodic boundary conditions, each field line passes through the simulation multiple times, although each pass can also be considered a separate field line. On the left side, in the upstream magnetosphere, the field is laminar. A band of magnetic flux ropes borders this region, just to the left of the strongest turbulence which peaks at $N \approx 3.5$. These coherent structures bound the chaotic field lines that fill the large-scale magnetic island. (The field lines within the island intersect the plane twice, once at $2.5 \lesssim N \lesssim 5$ and again at $7 \lesssim N \lesssim 8.5$.) The twisting of flux ropes by the vortical $M - N$ flows is similar to that inferred from MMS observations by [72].

4.3 Generalized Ohm's Law

The role of turbulence can be quantified by evaluating the terms of the generalized Ohm's law in a cut through the x-line. We begin with the momentum equation for the electron fluid

$$en\mathbf{E} = -mn\frac{d\mathbf{v}}{dt} - \boldsymbol{\nabla}\cdot\mathbb{P} - en(\mathbf{v}/c)\times\mathbf{B} \tag{4.1}$$

where m, n, $\mathbf{v}$, and $\mathbb{P}$ are the electron mass, density, velocity, and pressure tensor (we only refer to electrons below and so have dropped the species subscripts). Taking the out-of-plane (M) component gives, after invoking symmetry with respect to the

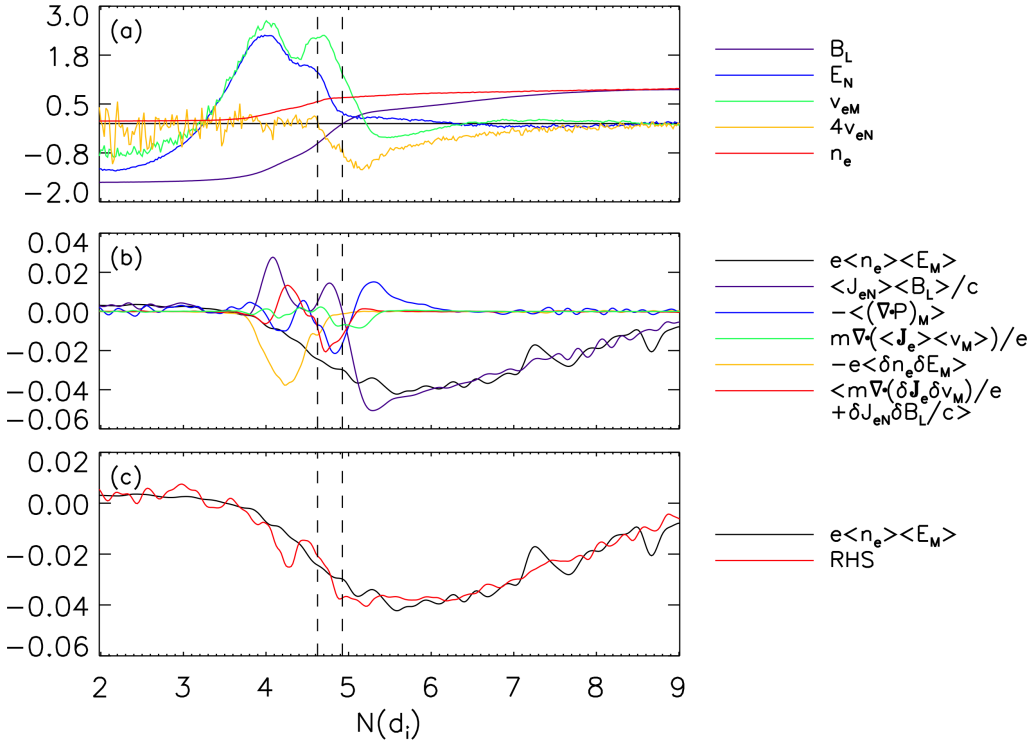

Figure 4.6: Cuts in the N direction through the electron diffusion region for the three-dimensional simulation. Panel (a): The density n_e, reconnecting magnetic field B_L, the normal electric field E_N, and the electron flows v_{eN} and v_{eM} all averaged over M. Panel (b): The principal terms in Ohm's law from equation 4.3. (Additional small terms are included, as noted by the key, but produce minimal effects.) Panel (c): The sum of the left and right sides of equation 4.3. In each panel the vertical lines show the approximate positions of the stagnation point ($N \approx 4.5$) and x-point ($N \approx 4.9$).

L coordinate near the x-line [62],

$$enE_M = -env_N B_L/c - \left(\frac{\partial P_{LM}}{\partial L} + \frac{\partial P_{NM}}{\partial N} + \frac{\partial P_{MM}}{\partial M}\right) - m\left(\frac{\partial}{\partial t}nv_M + \frac{\partial}{\partial N}nv_N v_M\right). \tag{4.2}$$

In the two-dimensional case $\partial P_{MM}/\partial M = 0$.

In Figure 4.6a we highlight the basics of asymmetric reconnection by plotting some of the key parameters on a cut along N through the x-line: n, B_L, E_N, v_M and v_N. The magnetosphere is on the left and the magnetosheath on the right. For asymmetric reconnection the stagnation point, where $v_N = 0$, lies on the magnetosphere side of the x-point, where $B_L = 0$ [47]. The vertical dashed lines in the figure indicate the approximate locations of these points. The high-speed electron flow v_M is dominantly driven by E_N and these two quantities track each other across the diffusion region. The qualitative behavior of cuts through the two-dimensional simulation (not shown) is similar to Figure 4.6(a) and consistent with the results of [62]. The electron inertia term balances E_M where $B_L = 0$ and the divergence of the pressure tensor balances E_M where $v_N = 0$.

To establish the role of turbulence in the three-dimensional simulation, we average over the M direction and decompose every quantity into a mean and fluctuating component, i.e., $n = \langle n \rangle + \delta n$.[3] Note that products of quantities produce two terms, $\langle AB \rangle = \langle A \rangle \langle B \rangle + \langle \delta A \delta B \rangle$. Keeping the most significant terms in equation

[3] Another option is to temporally average. However, our space resolution is much higher than our temporal resolution, so we utilize the method with better resolution.

4.2 gives

$$e\langle n\rangle\langle E_M\rangle = \langle J_N\rangle\langle B_L\rangle/c - \left[\frac{\partial}{\partial L}\langle P_{LM}\rangle + \frac{\partial}{\partial N}\langle P_{NM}\rangle\right] + \frac{m}{e}\left[\frac{\partial}{\partial L}\langle J_L\rangle\langle v_M\rangle + \frac{\partial}{\partial N}\langle J_N\rangle\langle v_M\rangle\right] - e\langle\delta n\delta E_M\rangle + \left\langle \delta J_N \delta B_L/c + \frac{m}{e}\frac{\partial}{\partial N}\delta J_N \delta v_M \right\rangle \quad (4.3)$$

In deriving equation 4.3, the weak time-dependence has been dropped since we are focusing on steady-state behavior. We have also discarded terms containing J_L and δJ_L that symmetry arguments suggest are small (and which we have confirmed are small in the simulation data).

The first three terms on the right-hand side involve only mean quantities and can be matched to terms in equation 4.2. They represent the usual contributions from the convective motion, pressure tensor, and inertial terms. The final two terms arise from the fluctuations and can be interpreted as contributions from an anomalous resistivity and an anomalous viscosity associated with the turbulent transport of the canonical momentum $mv_M - eA_M/c$ with $B_L = \partial A_M/\partial N$, where $\mathbf{A}$ is the vector potential [73].

Figure 4.6(b) displays the separate terms of equation 4.3 and Figure 4.6(c) shows the left side and the total of all of the terms on the right side. (While equation 4.3 includes only the most significant terms, all but the time-dependent term were kept for the figure.) The anomalous resistivity term $\langle\delta n\delta E_M\rangle$ is large around the stagnation point but diminishes near the x-point while the viscosity term is significant over a broad region between the two. Note that at the x-point the viscosity term is comparable to the off-diagonal pressure tensor term, which has been previously thought to be largely responsible for reconnection [74, 75]. Without

the inclusion of these terms, the two curves in panel (c) would not match. Thus, turbulent effects are playing an essential role in balancing the reconnection electric field.

4.4 Particle Distribution Functions

Recent investigations of particle distributions in two-dimensional asymmetric reconnection have revealed crescent-shaped features in the $v_M - v_N$ phase space of electrons. These are signatures of the cusp-like motion produced by the combination of E_N and a gradient in B_L [38,63,64]. If, in the electron current layers driven by E_N, the turbulence is sufficiently strong the fluctuating electric fields might scatter the electron orbits, preventing the formation of the crescent distributions. Of course, if the electrons were simply gyrating around the $\mathcal{O}(1)$ field, the turbulence would not strongly affect the orbits unless the turbulence frequency was comparable to Ω_{ce}. However, instead the orbits are cusp-like and unmagnetized close to the magnetic null where they are directly accelerated by E_N across B_L [63,64]. The motion along N is then turned into the M direction by B_L to produce the electron drift v_{eM}. If the turbulence breaks up the current layer so that the components of E_M and E_N are comparable, the electrons will be directly accelerated in both the N and M directions, potentially disrupting the cusp-like motions.

However, Figure 4.7 suggests that the crescents survive even when the turbulence in the electron current layers is strong. Panel a displays data from a region upstream of the x-line on the magnetosphere side from the two-dimensional simu-

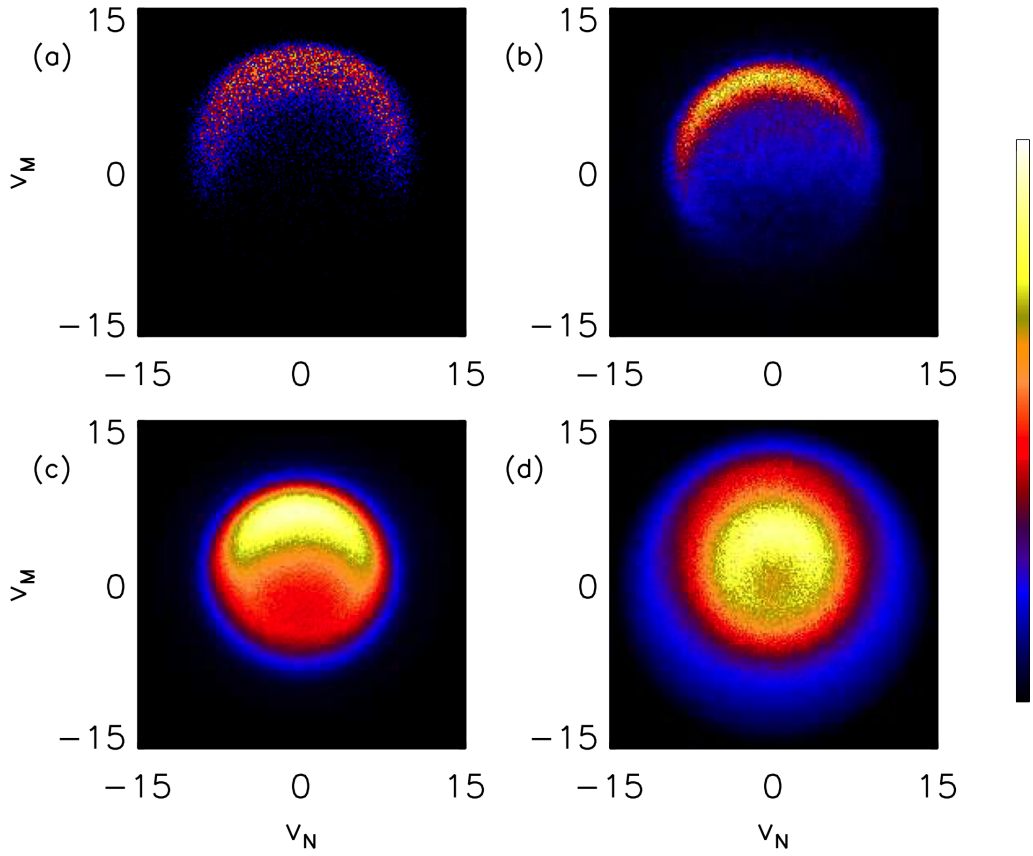

Figure 4.7: $v_N - v_M$ electron distribution functions from the two-dimensional (panel (a)) and three-dimensional (panels (b-d)) simulations. The distributions were taken at the positions shown by the stars in Figure 4.4. Panels (b) and (c) were taken near the x-line. In panel (b) only a limited range in M was sampled, $1 \leq M \leq 1.25$; panels (c) and (d) sample the entire box, $0 \leq M \leq 10.24$. Panel (d) was taken near the separatrix, downstream from the x-line (see Figure 4.4). The number of particles in each velocity bin is plotted on a linear scale that is different for each panel, although the color bar shows the relative variation.

lation. The crescent is clearly visible, consistent with earlier simulations [62, 63, 76] and the MMS data [38]. Data from the three-dimensional simulation, also taken from the magnetospheric side of the x-line, is shown in panels (b) and (c). For panel (b) the distribution is taken over a limited range in the out-of-plane direction $1 \leq M \leq 1.25$ while panel (c) is taken over all M. The crescent is clearly present in panel (b). In panel (c), integration over the larger range in M samples many periods of the turbulence and smears out, but does not destroy, the crescent. Panel d shows a distribution taken near the separatrix but downstream from the x-line in the three-dimensional simulation. A crescent feature is still visible.

The crescents from the two-dimensional and three-dimensional simulations do exhibit some qualitative differences. The noisier distribution of panel (a) is a consequence of the smaller number of particles (and hence larger random noise) per velocity bin. Second, the two-dimensional case shows a faster bulk flow in the M direction. This is because the electron current layer in the two-dimensional case remains highly localized in the N direction. In contrast, the turbulence in the three-dimensional run broadens the current layer. Since the integrated current across the layer must be the same in both cases, the broader layer from the three-dimensional run produces a smaller bulk velocity. On the other hand, the small counter-clockwise rotation observable in panel (b) is simply a consequence of the location at which the distribution is taken. Similar rotations can be seen in the two-dimensional simulation for distributions from nearby locations.

4.5 Discussion

Reconnection in asymmetric configurations can be stabilized by the presence of diamagnetic drifts [77–79], with complete stabilization occurring when the difference in $\beta = 8\pi P/B^2$ between the asymptotic plasmas exceeds $\tan\theta/2$, where θ is the shear angle between the reconnecting fields. In the configuration considered here, $\Delta\beta \approx 2.5$ is relatively large but, because the guide field is small, $\theta \approx 170^\circ$ is also large. Hence reconnection is unaffected by diamagnetic drifts, which is in agreement with the reconnection rate of $\mathcal{O}(0.1)$ observed for the both the two-dimensional and three-dimensional simulations. As a separate effect, a finite guide field can affect the development of structures in the out-of-plane direction. Because $B_M/B_L \lesssim 0.1$ is small in this case, however, the oblique tearing mode and the development of flux ropes, as seen in [80], does not occur in our domain.

An important question is whether real mass-ratio simulations would yield results that differ significantly from the present simulations where $m_i/m_e = 100$. We suggest that the results should not be sensitive to the mass-ratio, and we discuss a mass-ratio 400 simulation in the next chapter. Even with real mass ratios the LHDI is strong in systems with scale lengths near the ion Larmor scale, which is characteristic of the boundary layers with strong E_N at the magnetopause. The suppression of LHDI by magnetic shear and finite β is weaker in asymmetric reconnection because the strongest density gradient and peak current J_{eM}, which drive the instability, are on the magnetosphere side of the x-line where β is smaller. The strongest turbulent drag (Figure 4.6(b)) is peaked near the stagnation point ($v_{eN} = 0$), well away from

the magnetic null. The anomalous viscosity terms (Figure 4.6(b)) peak in the region between the magnetic null and the stagnation point where the gradients in v_{eM} are greatest and have scale lengths below d_i.

In a recent paper [72], Ergun et al. report on MMS observations of very intense parallel electric fields found in small-scale structures along the magnetospheric separatrices during magnetopause reconnection. They associate these parallel electric fields with localized reconnection events in which the magnetic field is twisted by vortical plasma motions in the $M-N$ plane. The magnetic turbulence that develops along the separatrices of our three-dimensional simulations is reminiscent of these observations – the strong electron flows basically twist up the magnetic field. On the other hand, the parallel electric fields in our simulations are not as intense as in the MMS data ($\approx$ 10 versus $\approx$ 100 mV/m) and are largest in the diffusion region rather than along the separatrices. Cuts of $E_{\parallel}$ in the $M-N$ plane through the x-line (not shown) reveal electron holes similar to those seen in earlier simulations with larger guide fields [81]. One possible explanation for this discrepancy may be the artificially low mass ratio. A realistic value could yield sharper gradients and more intense fields. It is also possible that in our simulations we are only exploring the early stages of the dynamics of these turbulent current layers. With larger simulations that could be evolved for longer times it is possible that the strong parallel currents that develop along the separatrices might form more intense localized parallel electric fields as seen in some earlier two-dimensional simulations [82, 83].

The role that turbulence might have in breaking the frozen-in condition has not yet been explored with the MMS data. On the other hand, short bursts of

$E_M \sim 10$ mV/m were seen in the current layer where E_N is large [38]. Thus, the presence of turbulence seems likely but its consequences and the specific correlated averages that need to be carried out to evaluate the anomalous drag and viscosity coefficients in equation 4.3 have not been evaluated.

In conclusion, we find that the inclusion of the third dimension permits the development of strong turbulence, both at the x-line and along the separatrices. This turbulence makes significant contributions to the balance of Ohm's law but, perhaps surprisingly, does not disrupt the formation of crescent features in the velocity distribution functions. Hence, the existence of such crescents cannot serve as an indicator as to whether turbulence plays an important role at a reconnection x-line.

Chapter 5: Turbulence in 16 October 2015 Simulations

In the previous chapter we performed a three-dimensional simulation of reconnection with initial conditions representative of an MMS observation of an electron diffusion region [38][1]. We observed turbulence developing around both the x-line and the separatrices and showed that the turbulence was strong enough to contribute an effective "anomalous resistivity" and "anomalous viscosity" to Ohm's law in the electron diffusion region. We suggested that the turbulence was due to LHDI. Others have noted, however, that the turbulence measured by the MMS did not satisfy the criteria for the "local" LHDI outlined above [85]. In this chapter, we perform a more detailed analysis of the turbulence produced in reconnection simulations and conclude that it, in fact, shares many characteristics with the longer wavelength electromagnetic version of the LHDI. These conclusions are consistent with [86], who also showed that during reconnection the instability produced significant transport across the magnetospheric separatrix. In addition, we identify characteristics of the turbulence in our simulations that are consistent with MMS observations.

[1] This chapter is based on Price et al., 2017 [84]

5.1 Simulation Descriptions

We study the simulation presented in Chapter 4, along with another simulation with the same asymptotic parameters. While the simulation presented in Chapter 4 has a computational domain of dimension $(L_L, L_M, L_N) = (40.96, 10.24, 20.48)$, the new simulation has dimensions $(20.48, 5.12, 10.24)$. These simulations differ in computational parameters, namely the ion-to-electron mass ratio, the grid resolution, and the speed of light. The mass ratios are 100 and 400, respectively, which eases the computational expense associated with using the true mass ratio yet is sufficient to separate the ion d_i and electron d_e scales ($d_e = 0.1d_i$ and $0.05d_i$, respectively). Note that although the computational domains differ in size when measured in d_i, they are the same size when measured in electron scales (d_e or ρ_e).

The spatial grid has resolutions of $\Delta = 0.02$ and $\Delta = 0.01$, respectively, which resolve the system's smallest physical scale, the Debye length in the magnetosheath, ≈ 0.03. We use 50 particles per cell per species when $n = 1.0$ and, as this implies ≈ 3 particles per cell in the low-density magnetosphere, our analysis employs, when necessary, averages over multiple cells to mitigate the resulting noise. The speed of light is chosen to be $c = 15$ and 30 respectively, and our boundary conditions are periodic in all directions. A small perturbation is added to initialize reconnection. Companion two-dimensional simulations show that reducing the size of this perturbation by a factor of two has no significant effect other than delaying the onset of reconnection. Unless otherwise stated, the subsequent figures and discussion focus on the larger simulation with $m_i/m_e = 100$.

5.2 Electromagnetic Turbulence

In two-dimensional simulations, where variations in the out-of-plane (M) direction are suppressed, reconnection in this system remains laminar, as we saw in Chapter 4. In contrast, the additional freedom present in three-dimensional simulations allows modes to develop with finite k_M. Figure 5.1 displays images of J_{eM}, the dawn-dusk electron current density, in a single $L-N$ plane at four representative times. The reason for choosing these times will be discussed further below, but they roughly correspond to the onset of the instability, the time of maximum growth, the beginning of the saturated non-linear state, and the end of the simulation. The magnetosphere (strong field, low density, high temperature) is to the left and the magnetosheath (weak field, high density, low temperature) to the right. The results exhibit the typical features of asymmetric reconnection, including the bulge of the magnetic islands into the low-field-strength magnetosheath and the separation between the x-point and the stagnation point of the fluid flow [47]. As can be seen in panel (a), turbulence first develops along the magnetospheric separatrix before developing at the x-line (panel (b)) and the magnetosheath separatrix (panels (c) and (d)). Images from other $L-N$ planes exhibit similar features.

The instability driving the turbulence is electromagnetic in nature, as can be seen in Figure 5.2. Panels (a-h) show E_M and δB_L in the $M-N$ plane that cuts through the x-line, while panels (i-p) show the same quantities along a cut through the island. Here, δB_L is the fluctuating component of B_L, i.e., $\delta B_L = B_L - \langle B_L \rangle$, where $\langle B_L \rangle$ is B_L averaged over the M direction. This is the dominant magnetic

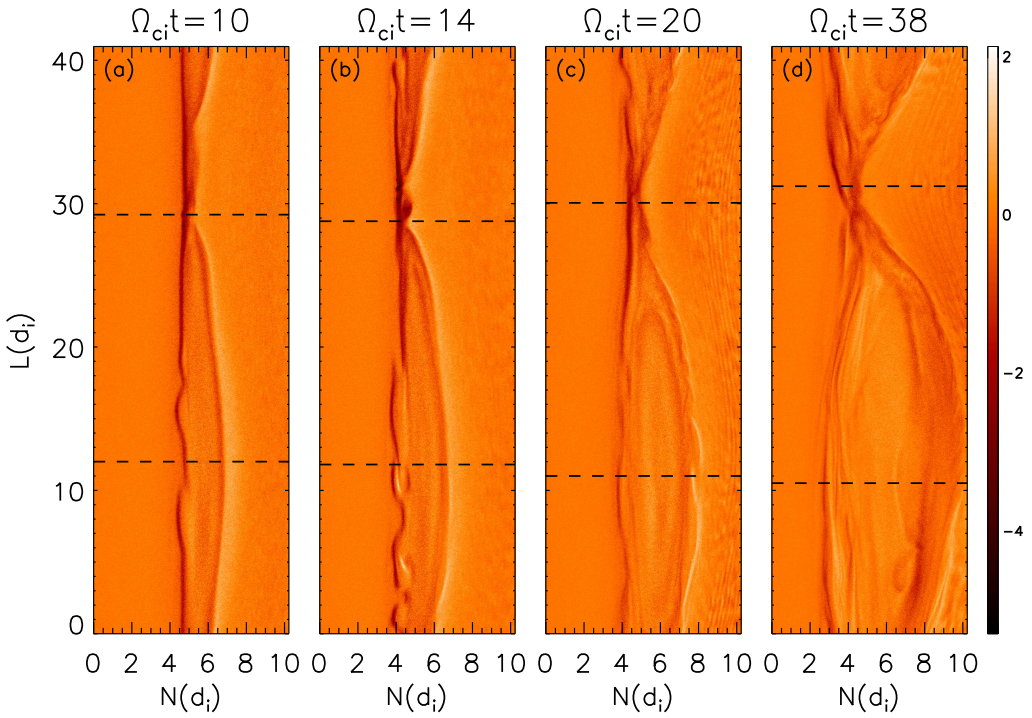

Figure 5.1: Snapshots of J_{eM}, the dawn-dusk electron current density, in one $L - N$ plane. Panels (a-d) are taken at $t = 10$, 14, 20, and 38, respectively. These times highlight the onset of the instability, the time of maximum growth, the beginning of the saturated non-linear state, and the end of the simulation. The colors in each panel are identically normalized, with the color bar at the right showing the range. The dashed lines in each panel indicate the locations of cuts through the x-line and island presented in Figure 5.2.

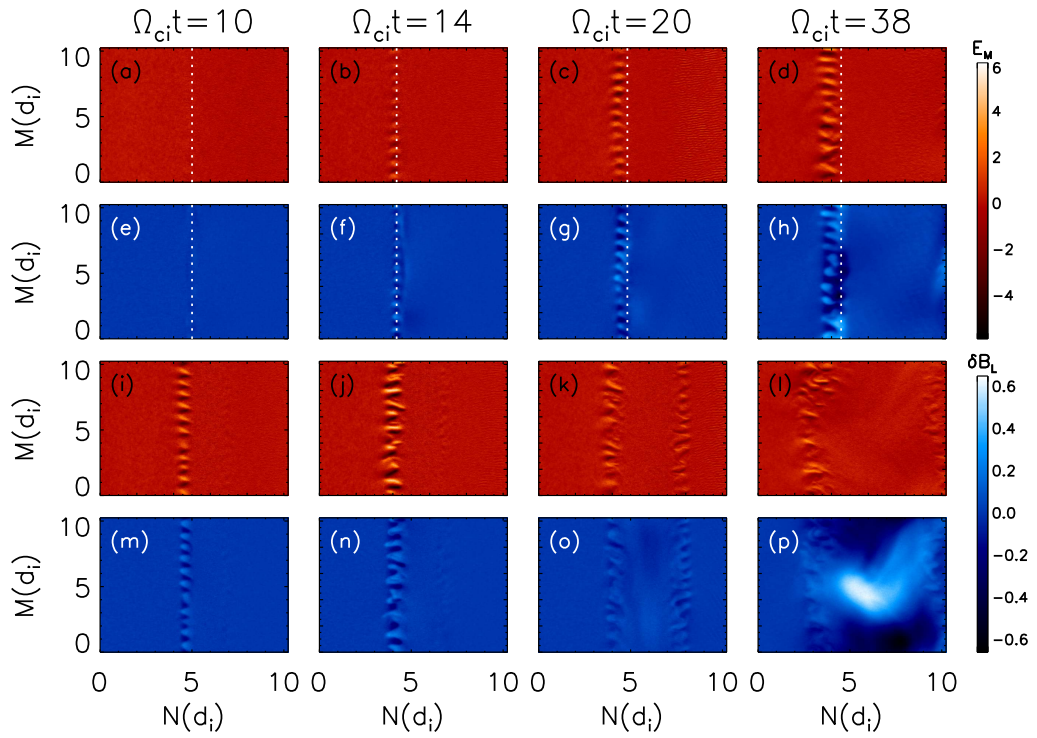

Figure 5.2: Snapshots of E_M (a-d, i-l), the electric field in the direction of the reconnection-associated current, and δB_L (e-h, m-p), the fluctuations in the reconnecting magnetic field, in the $M-N$ plane at the same times as in Figure 5.1. The cuts were taken at the positions shown by the dashed lines in Figure 5.1. Panels (a-h) are taken at the L location of the x-line, while panels (i-p) are taken through the middle of the island. The red color bar corresponds to E_M, while the blue color bar corresponds to δB_L. The dotted lines in panels (a-h) correspond to the N location of the x-line.

field perturbation – convection of the large gradient of B_L in the initial state due to the perturbed v_{eN} leads to large fluctuations. Fluctuations of B_M and B_N are also present but at a reduced amplitude.

The turbulence first appears in both E_M and δB_L at $t = 10$ along the magnetospheric separatrix in panels (i) and (m). Turbulence develops at the x-line (panels (b) and (f)) and along the magnetosheath separatrix (panels (j) and (n)) by $t = 14$,

though the latter is clearer by $t = 20$ (panels (k) and (o)). It is interesting to note that, even at relatively early times, the location of the turbulence begins to shift away from the x-line, denoted by the white dotted lines in panels (a-h), towards the magnetosphere. We also observe evidence of a possible kink mode late in the simulation in panel (p).[2] This mode produces a global perturbation to the current sheet, but at longer wavelength than the fluctuations seen in the other panels.

The wavelength of the drift instability can be directly measured in several of the panels. In Figure 5.2(c), for example, there are 11 wavelengths present in the M direction (length $10.24d_i$). In our mass-ratio 100 simulation $1d_i \approx 20\rho_e$, which gives $k_M\rho_e \approx 0.33$. As will be discussed later, this is consistent with the expectation for long wavelength LHDI.

5.3 Fourier Analysis

While LHDI is the most likely candidate to explain the turbulence seen in our simulations, the modified-two-stream instability (MTSI) can also exist in finite β systems if the relative cross-field drifts of the electrons and ions are comparable or exceed the local Alfvén speed [87]. It has been suggested that this instability is important in laboratory reconnection experiments [88]. This instability has a growth rate that peaks with a non-zero component of the wavevector along the local magnetic field $k_\parallel$ in contrast with the LHDI, which has a peak growth rate for $k_\parallel = 0$ [60]. Thus, to distinguish between the possible drivers of the turbulence, we examine

[2] This mode is not observed at the X-line. It could be stabilized by the density or velocity shear that appears at that location but not through the island.

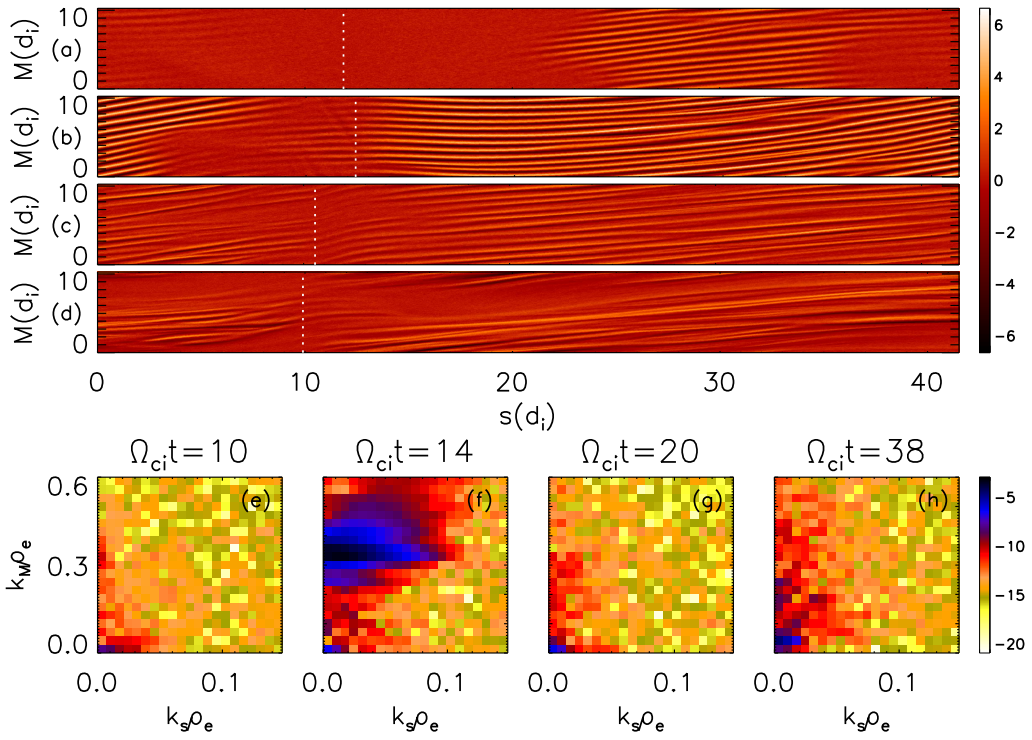

Figure 5.3: $E_M(s, M)$ (panels (a)-(d)) and Fourier transforms (panels (e)-(h)) at the same times as in Figure 5.1, where s is the distance along the average (over M) magnetic field. The data is from a surface that lies to the left (magnetospheric side) of the magnetospheric separatrix. Panel (a) shows $E_M(s, M)$ at $t = 10$; the $k_s - k_M$ power spectrum $\log(|\tilde{E}_M(k_s, k_M)|^2)$ at the same time is shown in panel (e). Panels (f), (g), and (h) are similarly paired with panels (b), (c), and (d) and show the simulation data at $t = 14$, 20, and 38, respectively. The white dotted lines in panels (a-d) correspond to the location of the x-line. Panels (a-d) are normalized to the same value, as seen in their accompanying color bar. Panels (e-h) also have a common normalization.

its Fourier spectrum perpendicular to and along the local magnetic field in $k_\perp - k_\parallel$ space, where $k_\perp$ is calculated from the data along the M direction. Since the local direction of the magnetic field varies in space, the necessary data must be taken while following a magnetic field line. Furthermore, since the actual field lines have chaotic trajectories, as we saw in the previous chapter, the analysis is carried out using the magnetic field components obtained by averaging over the M direction. The averaged magnetic field on the magnetospheric side of the reconnection layer follows the separatrix between the upstream and reconnected plasma, while M points in the perpendicular direction. Choosing s to represent the distance measured along the field, we construct $E_M(s, M)$ while traveling along a field line just outside the separatrix. The range of s is chosen in order to travel through the simulation domain in the L direction exactly once. This data is not periodic in s for a given value of M but the data can be extended arbitrary distances along s by stacking the data along s if it is shifted a fixed distance in M.

The resultant $E_M(s, M)$ at four times can be seen in Figure 5.3(a-d). The primarily horizontal stripes correspond to the same instability shown in Figure 5.2. In panel (a), calculated at $t = 10$, the instability is weak at the location of the x-line (the white dotted line), but strong near the middle of the island (see Figure 5.1a). By $t = 14$ in panel (b) the instability is present at all values of s, including at the x-line, although it remains strongest near the middle of the island. This pattern persists at later times, $t = 20$ and 38, panels (c) and (d) respectively, making it appear that the turbulence near the x-line is not strong. However note that, as seen in Figure 5.2(c) and (d), the turbulence at these times is displaced from the

separatrix. Although not shown here, $E_M(s, M)$ at the x-line is much stronger along a trajectory that is displaced toward the magnetosphere compared with that shown in Figure 5.3.

To determine the dominant wavelengths present in $E_M(s, M)$, we construct two-dimensional spatial Fourier transforms (denoted by the operator $\mathcal{F}$) of the $s-M$ domain, $\tilde{E}_M(k_s, k_M) = \mathcal{F}[E_M(s, M)]$. We plot $\log(|\tilde{E}_M(k_s, k_M)|^2)$ for the longest wavelength modes in Figure 5.3(e)-(h). At $t = 10$, panel (e), which is the linear stage of the instability, the spectrum is dominated by nearly-perpendicular wavevectors (note the difference in vertical and horizontal axis scales). The peak power when the instability is strongest, $t = 14$, occurs for $k_M\rho_e \approx 0.33$, consistent with the calculation based on Figure 5.2. By this time the spectrum has acquired a significant parallel wavevector (k_s), although it continues to be dominated by perpendicular modes. After saturation (panels (g) and (h)), however, those parallel modes diminish in strength. With an ion-to-electron mass ratio of 100, theory suggests that the longer wavelength LHDI mode has $k_M\rho_e \sim (m_e/m_i)^{0.25} \approx 0.32$, which is in very close agreement with our measured value of $k_M\rho_e \approx 0.33$. (This comparison neglects the fact that $T_i \neq T_e$ which will have a modest effect on the theoretical value.)

The non-local structure of the MTSI has not been explored in the literature. Nevertheless, in local models the instability peaks at $k_\parallel/k_\perp \sim \sqrt{m_e/m_i}$ [87]. For the simulation data shown in Fig. 5.3 in which $m_i/m_e = 100$ the spectrum should exhibit a distinct peak centered on $k_s \sim 0.1k_M$ if it were driven by the MTSI. There is no evidence for a peak at finite $k_\parallel$ in the data of Fig. 5.3.

However, the data of Fig. 5.3 does reveal that k_s is finite. We suggest that this

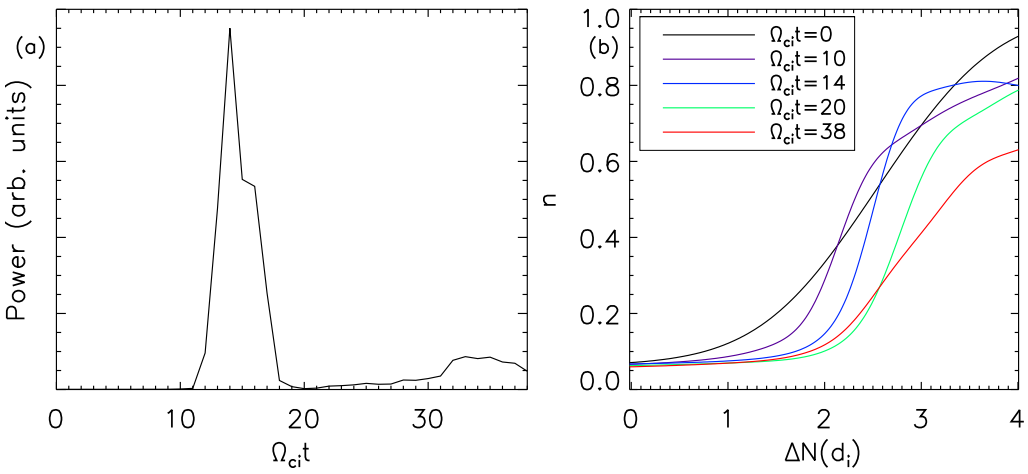

Figure 5.4: Panel (a): Power in the instability based on the Fourier transforms shown in Figure 5.3. Panel (b): Density profiles at the x-line over time. Since the location of the density gradient changes as the islands expand, the density profiles at later times are shifted in N to ease comparisons.

is a consequence of the inhomogeneity of the out-of-plane current with distance along the separatrices. As discussed in the previous chapter, this instability dominantly drives flows in the $M-N$ plane. The resulting twisting of flux ropes by the vortical $M-N$ flows is similar to that inferred from MMS observations by [72]. The strength of the vortices varies with distance along the field line (s direction) because the amplitude of the out-of-plane current J_{eM} depends on the distance from the x-line. As a consequence, the rate of twist of the flux tubes varies with distance from the x-line, generating non-zero values of B_M and B_N and a finite k_s.

5.4 The Power-Density Correlation

The total power in the instability's fluctuating electric field

$$P = \sum_{k_s,k_M} |\tilde{E}_M(k_s, k_M)|^2 \tag{5.1}$$

is computed for the duration of the simulation and plotted in Figure 5.4(a). The instability first becomes noticeable around $t = 10$, climbs rapidly to a peak at $t = 14$ and then rapidly decreases in intensity as it non-linearly saturates due to the relaxation of the driving gradients. A secondary instability, perhaps the kink mode that can be seen in the final panels of Figure 5.2, begins to grow, albeit more weakly, near the end of the simulation. This general pattern is not specific to the choice of E_M and is found in similar calculations performed on any component of the fluctuating electric and magnetic fields.

As discussed earlier, the energy source for the instability is the relative electron-ion drift, which is dominantly produced by the ion pressure gradient. Because of the large drop in the density across the magnetopause for the initial conditions of the present simulation, the ion pressure drop is dominated by the change in density. We therefore explore the linkage between the time evolution of the density profile and the development of the turbulence to demonstrate the causal relation between the local gradient and the turbulence. Figure 5.4(b) shows the density profiles at the x-line for several times. Because the N location of the current sheet changes as reconnection occurs, the density profiles have been shifted to make comparisons easier. The initial density scale length L_n ($\approx 1d_i = 10d_e$ for mass-ratio 100) steepens as

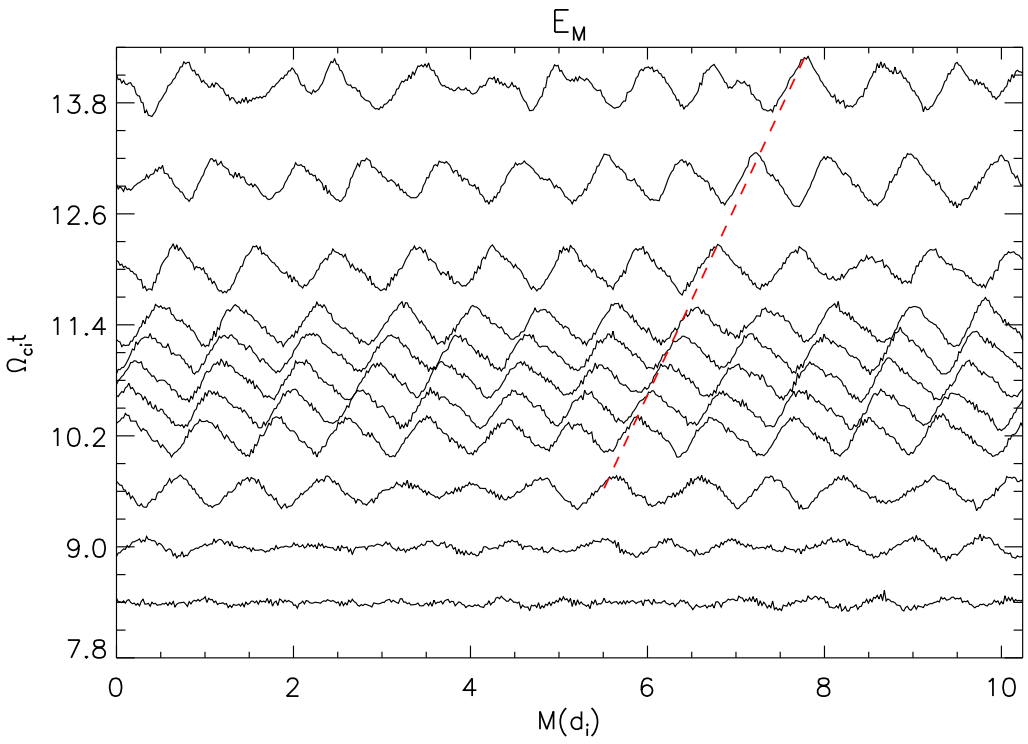

Figure 5.5: Cuts of E_M along the M direction through the center of the turbulence at the magnetospheric separatrix. The vertical position of each cut is shifted based on the time at which it was taken. The red dashed line traces the displacement of one wave peak.

reconnection develops, reaching its minimum value ($L_n \approx 0.25d_i = 2.5d_e$) at $t = 14$ when the instability is strongest. The density profile then relaxes and by the end of the simulation $L_n \approx 0.5d_i = 5d_e$. This result should be contrasted with the results of 2D simulations with the same parameters (not shown), in which turbulence does not develop and in which the density gradient steepens in time and comes to a constant density scale length of around $1.0d_e$. Thus, the turbulence clearly limits the minimum density scale length and the corresponding width of the electron current layer.

5.5 The Instability's Frequency

Next we calculate the phase speed and frequency of the instability. Figure 5.5 shows cuts of E_M along the M direction through the center of the turbulence at the magnetospheric separatrix near the middle of the island. The vertical position of each cut corresponds to the time at which it was taken. The turbulence begins to appear over the background variations at $t \approx 9$ and by $t = 10$ has clearly developed linear oscillations. The topmost trace, at $t \approx 14$, is taken when the instability is strongest. The irregular variations show that it has already reached a non-linear stage. By tracing the displacement of one wave peak (the red dashed line), we determine the phase velocity of this wave to be $v_p \approx \frac{1}{2}v_A$ in the direction of the electron diamagnetic drift. This value is not specific to the wave peak chosen; similar results are obtained by translating the red dashed line in the M direction to adjacent peaks. Thus we can compute the instability frequency in the frame of the simulation $\omega = v_p k_M \approx \frac{1}{3}\Omega_{\rm lh}$.

This differs signficantly from $\Omega_{\rm lh}$, which is the textbook frequency of the LHDI. There are two reasons for this. The first is that, as discussed in [60], electromagnetic LHDI modes are not fixed at $\Omega_{\rm lh}$, but can instead have frequencies anywhere in the range $\omega_{\rm ci} \leq \omega \leq \Omega_{\rm lh}$. Second, the standard derivation of the frequency of LHDI frequency is performed in a frame with $E_N = 0$, which is not the case at the magnetopause and is not true for our simulation. In the $E_N = 0$ frame, the ions have the strongest drift, of the order of the ion diamagnetic drift velocity (which exceeds the electron diamagnetic velocity because the ions are hotter than the electrons). In

our system, the ions are close to stationary, so the observed frequency is naturally lower than the lower-hybrid frequency found in the typical analysis. Further, the mode propagates in the electron direction. In our simulation it is not possible to completely transform away E_N since this would require cE_N/B_L to be a constant. It is possible, however, to transform our simulation results into a frame in which the value of E_N is greatly reduced. At the magnetospheric separatrix during the time of linear evolution, $c(\mathbf{E}\times\mathbf{B})_M/B^2 \approx cE_N/B_L$ has a peak value of around $-1.7v_A$. In a frame with this velocity, the phase speed of the wave is $\approx 1.2v_A$, giving a frequency of $\omega = 0.8\Omega_{\rm lh}$, similar to the expected value. Finally, we note that waves below the lower-hybrid frequency at the magnetopause have been interpreted as arising from the LHDI [89].

5.6 Mass Dependence

In Chapter 4, we suggested that the qualitative features of a real mass-ratio simulation would not differ significantly from one with $m_i/m_e = 100$. Although we find that conclusion still holds, there are important quantitative differences between the simulation discussed in detail above (mass ratio of 100) and one with mass ratio 400. Figure 5.6(a-b) shows E_M in the $M-N$ plane through the x-line for mass ratio 100 (panel (a)) and 400 (panel (b)) at times of maximum power (as determined using equation 5.1). While the simulation domains differ in size when measured in d_i, they are equivalent when measured in ρ_e. The instability is stronger in the mass ratio 400 case and the turbulence has a greater spread in the N direction.

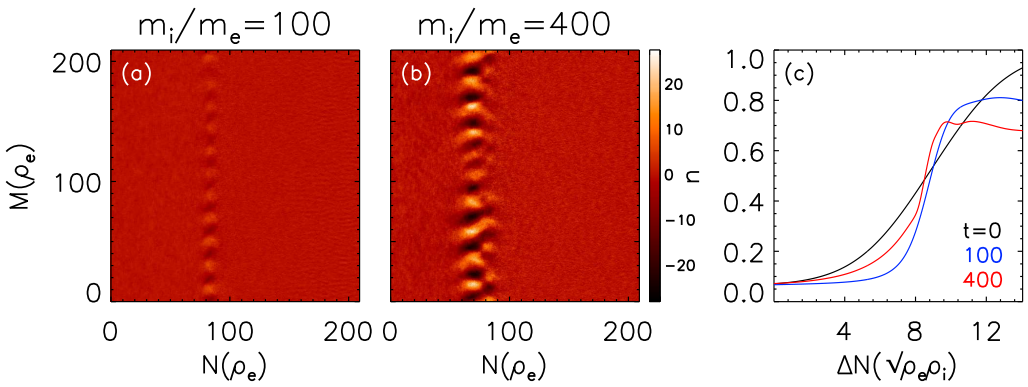

Figure 5.6: Comparison between the $m_i/m_e = 100$ and 400 simulations. Panels (a-b): Snapshots of E_M in the $M - N$ plane through the x-line at times of maximum power for $m_i/m_e = 100$ (panel (a)) and 400 (panel (b)). The numerical values of E_M have been converted to units of mV/m. Panel (c): Density profiles at the x-line at $t = 0$ and times of minimum density scale length. As in Figure 5.4(b), the profiles have been shifted in N to facilitate comparison.

As before, the wavelength of the instability can be visually determined. In Figure 5.6(b), there are 10 wavelengths in the M direction (length $\approx 209\rho_e$), giving $k_M\rho_e \approx 0.30$. In agreement with theoretical expectations there are fewer wavelengths (10 versus 11) and smaller $k_M\rho_e$ for the more realistic mass ratio. Furthermore, by constructing $E_M(s, M)$ and $\log(|\tilde{E}_M(k_s, k_M)|^2)$ (not shown), we find that the peak of the instability occurs at $k_M\rho_e \approx 0.29$. For an ion-to-electron mass ratio of 400, the longer wavelength LHDI mode is expected to satisfy $k_M\rho_e \sim (m_e/m_i)^{0.25} \approx 0.22$. Note though that, as discussed below, the ambient density gradient also varies between the two simulations so the scaling $k_M\rho_e \sim (m_e/m_i)^{0.25}$ is only approximate.

The scale lengths of the density and current layers at the magnetopause are topics of scientific interest since they are linked to the processes that limit the electron current. As noted previously, our 2D simulations show that density scale

length is of order $1d_e$, which is the expected value in non-turbulent reconnection [90]. The current layers in the 3D simulations are limited by the development of turbulence and never reach electrons scales. Because our simulations are carried out with artificial mass ratios, care must be taken in interpreting the data. In Figure 5.6(c) we display density profiles at the x-line, similar to Figure 5.4(b), for our mass-ratio 100 and 400 simulations. The initial density profile is the same for both simulations. The profiles displayed for each mass ratio are chosen to correspond to the time when the density gradient is greatest. The horizontal length scale is measured in hybrid units, $\sqrt{\rho_i \rho_e}$. Thus, the minimum scale length of the density profile (and the current profile) during reconnection at the magnetopause appears to scale as the hybrid of the electron and ion Larmor radii rather than either the electron or ion scale. However, because of the weak dependence of this scaling on the mass ratio and the limited mass ratios explored in the simulations, there is some uncertainty in this conclusion. Nevertheless, the current and density scale lengths at the magnetopause are significantly greater than the expected d_e or ρ_e scale. Further, the widths are comparable to measurement of the widths of current layers during symmetric reconnection in the magnetosheath [91] and in a laboratory reconnection experiment [92].

5.7 Localized Ohm's Law

The previous chapter considered the effects of the turbulence on reconnection by evaluating the contributions of various terms to an averaged Ohm's law measured

within the electron diffusion region. This average was performed over the entire M dimension and eliminated the first-order turbulent contributions in order to isolate the terms relevant to large-scale reconnection. Averaging over the turbulent scales, however, is appropriate only when there is a sufficient spatial and temporal separations between large-scale reconnection and the ambient turbulence. This assumption is normally satisfied since the turbulence is at the ρ_e scale with a frequency $\Omega_{\rm lh}$ while large-scale reconnection takes place on time scales longer than the Alfvén transition time across the computational domain. The conclusion from the averaged Ohm's law was that turbulent effects play an essential role in balancing the reconnection electric field.

Before making further comparisons between the simulations and the MMS data, we must establish the correspondence between the units used in the simulation and those used in spacecraft measurements. For the asymptotic parameters of the 16 October 2015 event ($B_{L,sh} \sim 23$ nT, $B_{L,ms} \sim 39$ nT, $n_{sh} \sim 11.3/\text{cm}^3$, $n_{ms} \sim 0.7/\text{cm}^3$) with "sh" and "ms" subscripts denoting the magnetosheath and magnetosphere respectively, $d_{e,sh} \sim 1.6$ km, $d_{i,sh} \sim 68$ km, $\omega_{ce,sh} \sim 4.05$ kHz, $\Omega_{\text{lh},sh} \sim 95$ Hz, $\omega_{ci,sh} \sim 2.2$ Hz, $v_{A,sh} \sim 150$ km/s and $E_{0,sh} \sim 3.4$ mV/m. In our simulations we find a reconnection electric field of ~ 0.2 mV/m for either mass ratio, a value that would be very difficult to detect observationally. In fact, MMS observations reveal spikes in E_M with much larger values, peaking around ± 10 mV/m. In addition, large amplitude, short-timescale fluctuations of the parallel electric field $E_\parallel$, up to 100 mV/m, have been reported [72, 85]. These intense parallel electric fields are not observed in our simulations.

The question, then, is whether the MMS electric field measurements correspond to an effective average over the turbulence in the simulation or a slice at a particular value of M. To answer this question, note that the particle instruments on MMS directly measure the full distribution function of electrons in 30 ms and of ions in 150 ms. The frequency ω of the fluctuations in the simulation is around $\frac{1}{3}\Omega_{\mathrm{lh},sh} = 30$ Hz so the period of the waves is around 200 ms. Thus, the electron data is collected over a very short period compared to the wave period. The MMS instruments are therefore measuring the local electron Ohm's law and not the average Ohm's law that controls the global reconnection rate.

In order to model what MMS would observe on a cut through the simulation we examine the various terms in the M component of Ohm's law (the electron equation of motion)

$$E_M = -\frac{1}{c}(\mathbf{v_e} \times \mathbf{B})_M - \frac{1}{ne}(\boldsymbol{\nabla} \cdot \mathbb{P}_e)_M - \frac{1}{e} m_e \mathbf{v_e} \cdot \boldsymbol{\nabla} v_{eM} \tag{5.2}$$

Here $m, n, \mathbf{v_e}$ and $\mathbb{P}_e$ are the electron mass, density, velocity, and pressure tensor. In Figure 5.7 we present data from two sample cuts through the electron diffusion region along the N direction that illustrate measurements characteristic of the MMS data. Figure 5.7(c) shows E_M near the x-line in the $M - N$ plane at $t = 38$. Panel (a) displays the separate terms in Ohm's law (Eq. 5.2) at $M = 4.9$ along a cut in the N direction (the upper dashed line in panel (c)). Panel (b) shows E_M and the sum of the terms from the right-hand side of equation 5.2. The two curves are in close agreement, which confirms that the simulation data is consistent with momentum conservation based on the electron equation of motion. Note also that the vertical

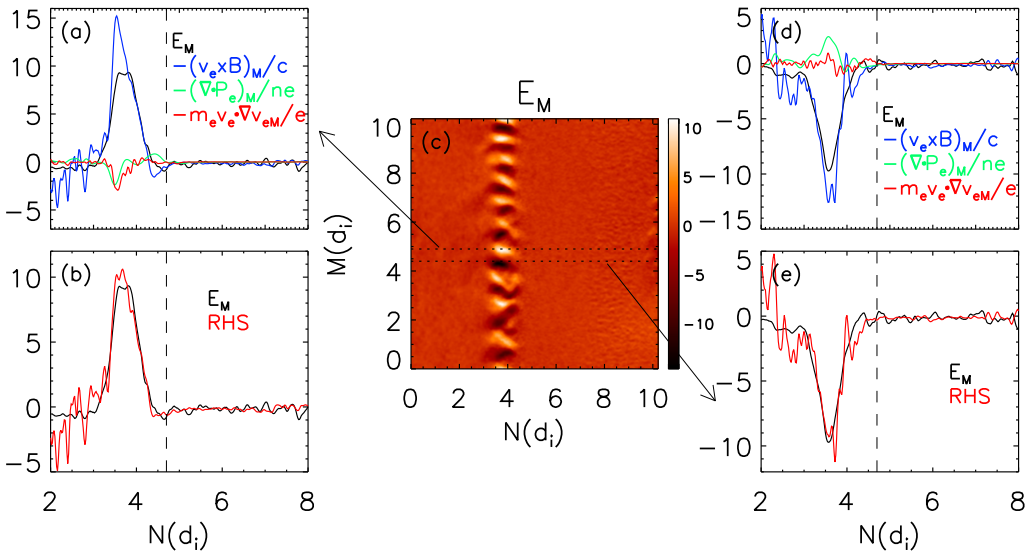

Figure 5.7: Evaluation of Ohm's law on cuts through the region of instability. For direct comparison to data, values are converted from our normalized units to mV/m. Panel (a): The terms in Ohm's Law from equation 5.2 for a cut through $M = 4.9$. Panel (b): The sum of the left and right sides of equation 5.2 for $M = 4.9$. Panel (c): E_M in the $M - N$ plane at $t = 38$. The horizontal dotted lines denote locations of two cuts, at $M = 4.4$ and 4.9. Panel (d): The terms in Ohm's Law from equation 5.2 for a cut through $M = 4.4$. Panel (e): The sum of the left and right sides of equation 5.2 for $M = 4.4$. The vertical dashed lines in panels (a), (b), (d), and (e) indicate the position of the x-line.

scale is expressed in mV/m so the curves reflect the size of the terms that should be visible in the MMS data. Panels (d) and (e) show the same information for a cut through $M = 4.4$. The value of E_M peaks around ± 10 mV/m, very close to the values reported in the MMS data [38]. The peak value of E_M changes sign between the two cuts, which are separated by a distance roughly comparable to the distance between the MMS spacecraft. Interestingly, a similar difference in polarity is seen in the MMS data (see Figure 5 of [38]). It should be emphasized that the large value of E_M shown in these cuts is a result of the turbulence and does not reflect the rate of magnetic reconnection. The reconnection electric field, while present, is two orders of magnitude smaller and can only be extracted by the type of averaging performed in the previous chapter.

5.8 Discussion

As a further demonstration that E_M is primarily associated with the turbulence, Figure 5.8 shows E_M and E_N (panels (a) and (b)) in the $M-N$ plane near the x-line at $t = 20$. In panel (c) we plot cuts of δE_M and δE_N at the locations denoted by the vertical dashed lines in panels (a) and (b). As the current layer breaks up, it naturally produces large values of E_M and the large electron currents in the M direction are diverted into the N direction. These N-directed flows are driven by E_M. The fact that δE_M and δE_N are similar in magnitude and roughly 90° out of phase indicates that the fluctuations are linked and not due to a steady-state reconnection process. Of course, the turbulence itself might undergo reconnection on faster time

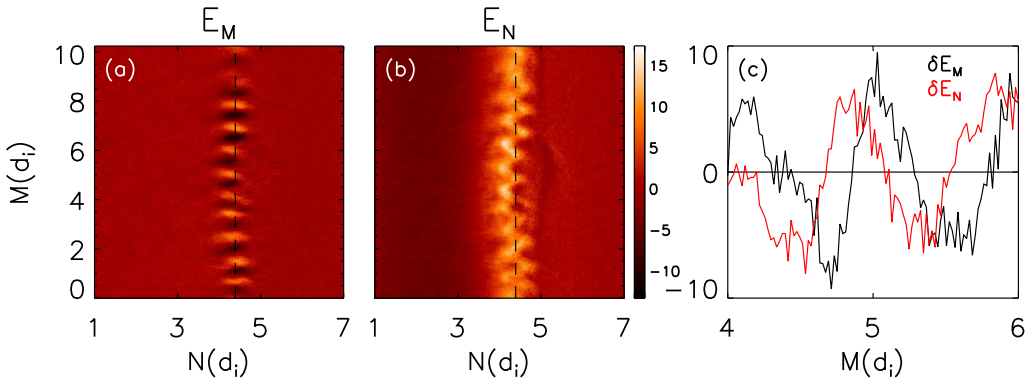

Figure 5.8: E_M and E_N (panels (a) and (b), respectively) in the $M-N$ plane at the x-line at $t = 20$. For direct comparison to data, values are converted from our normalized units to mV/m. Panel (c): δE_M and δE_N through the vertical dashed line in panels (a) and (b). Panels (a) and (b) are normalized to the same value.

scales and produce electric fields larger than the nominal value of 0.1mV/m. Such a possibility requires further analysis and comparison with observations.

Multiple MMS observations of magnetopause electron diffusion regions have found features similar to those in Figure 5.7 [85]. Since the observed turbulence did not satisfy the properties of homogeneous LHDI it was suggested that some other mechanism was responsible. However, the findings presented here suggest that the governing instability has all of the characteristics of a longer wavelength version of LHDI. The instability has a dominant wavelength satisfying $k\rho_e \approx (m_e/m_i)^{0.25}$, is observed in both electric and magnetic field components and has a wavevector that is dominantly, but not strictly, perpendicular to the local magnetic field. The frequency of the instability falls in the range of frequencies unstable to LHDI, $\omega_{\rm ci} < \omega \leq \Omega_{\rm lh}$ and the growth of the instability is closely correlated with the steepening and relaxing of a density gradient (and therefore the ion pressure gradient, which is

the basic driver of drift instabilities at the magnetopause). Similar instabilities have been seen in other three-dimensional reconnection simulations (albeit with different inital conditions) and were also attributed to LHDI [60, 68].

Chapter 6: Simulations of the 8 December 2015 MMS Encounter

Another MMS electron diffusion region encounter occurred on 8 December 2015 [93]. In this encounter, the guide field B_M was quite a bit stronger than that of the 16 October encounter. Figure 6.1 shows data from one of the MMS spacecraft. As before, the magnetosphere is identified by the region of high magnetic field strength B and low plasma density n, while the magnetosheath has a weaker B and higher n. In the magnetosheath, the guide field B_M is of the order of the reconnection magnetic field B_L. Similar to the 16 October crossing, the dissipation region is indicated by a nearly zero B_L, a peak in J_M, and a bursty reconnection electric field E_M. In contrast to the 16 October event, the ions do not exhibit a jet reversal in v_{iL}; instead v_{iL} gradually decreases in magnitude. However, the presence of the other indicators, in addition to a large electron outflow v_{eL}, suggests an EDR crossing at 11:20:43 UT. At this time, the spacecraft were at $(X, Y, Z) = (10.2, 1.3, -1.4)R_e$ in geocentric solar magnetospheric coordinates.

The crescent-shaped electron distribution functions seen in the 16 October event are also present here [36, 62–64]. Figure 6.2 shows data from MMS1 for 11:20:42-11:20:45 UT. The distribution functions on the right side of the figure are in separate planes, where $v_\parallel$ is parallel to $\mathbf{b} = \mathbf{B}/|\mathbf{B}|$, $\mathbf{v}_{\perp 1} = (\mathbf{b} \times \mathbf{v}) \times \mathbf{b}$, and

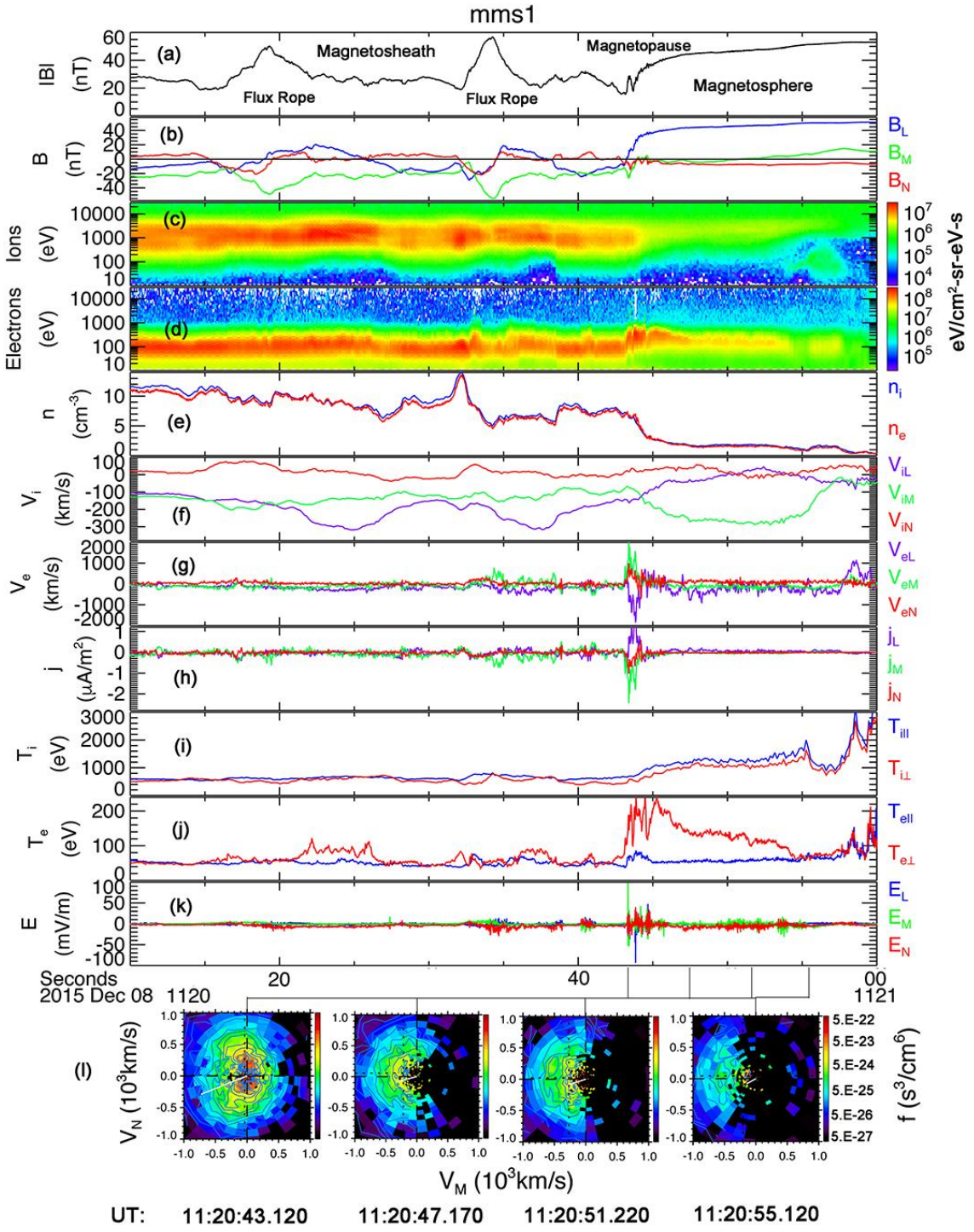

Figure 6.1: Data from MMS1. Vector quantities use the (L, M, N) coordinate system introduced in Chapter 2. Panel data shows (a) the magnetic field strength, (b) the magnetic field, (c-d) the energy-time spectrogram of ion and electron flux, respectively, (e) the plasma density, (f-g) ion and electron flow velocities, respectively, (h) current, (i-j) ion and electron temperature[1], respectively, (k) electric field, and (l) ion distribution functions in the $M - N$ plane. From Burch and Phan, 2016 [93].[2]

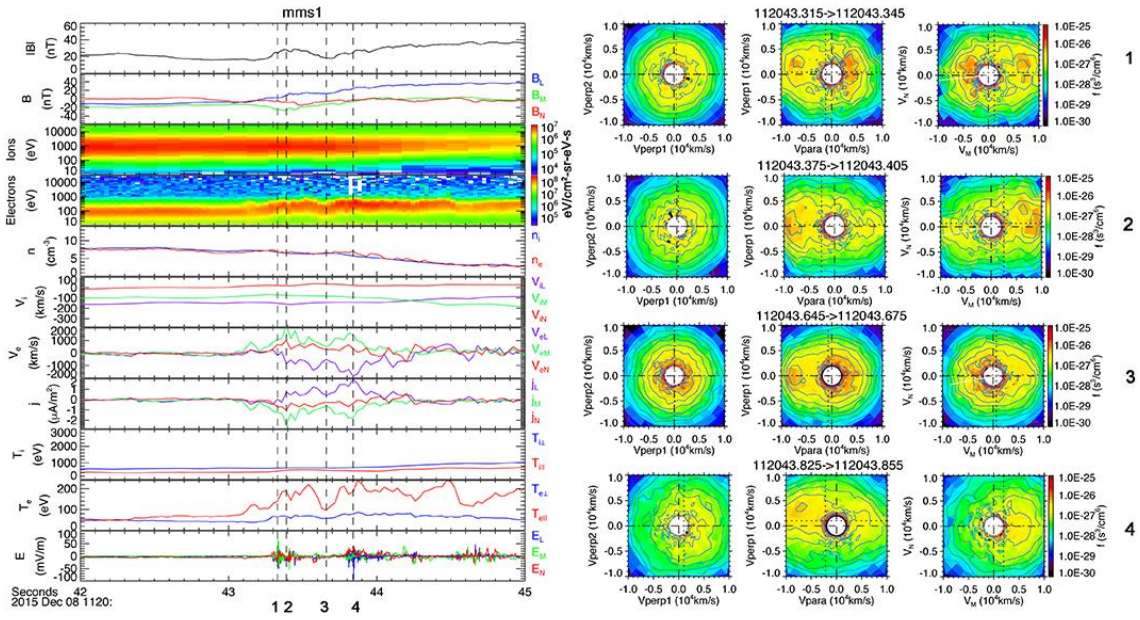

Figure 6.2: Data from MMS1 for three seconds around the time of the EDR encounter. The panels are in the same order as in Figure 6.1. The four vertical dashed lines indicate the regions with (1) in-plane magnetic null, (2) strongest out-of-plane current j_M near (1), (3) quiescent region, and (4) strongest out-of plane current j_M near the flow stagnation point. To the right are electron velocity space distribution functions for each region. The distribution functions are for (left column) $(v_{\perp 1}, v_{\perp 2})$, (middle column) $(v_{\parallel}, v_{\perp 1})$, and (right column) (v_M, v_N). From Burch and Phan, 2016 [93].[2]

$\mathbf{v}_{\perp 2} = -\mathbf{v} \times \mathbf{b}$ as in Chapter 4. The right-most column is in $M - N$ coordinates. The four regions are locations of the (1) in-plane magnetic null, (2) strongest out-of-plane current j_M near (1), (3) quiescent region, and (4) strongest out-of plane current j_M near the flow stagnation point. Regions 1-3 show mostly isotropic distributions in the plane perpendicular to $\mathbf{B}$ (left column), while parallel to $\mathbf{B}$ (middle column) shows mostly field-aligned populations, with evidence of a narrow beam along the $-\mathbf{B}$ direction in region 2. In the region near the flow stagnation point (4), the distributions are nongyrotropic in the left and right plots, which the authors identify as crescent-shaped. The "crescent" shapes are less defined in comparison to the 16 October event.

Here we present preliminary results of a three-dimensional simulation with initial conditions reflective of this MMS event with analysis similar to that performed in Chapters 4 and 5. The asymptotic code parameters explored here are not exactly the same as those measured by MMS, in part because measurement fluctuations make it difficult to fix the upstream state precisely. Nevertheless, they are similar enough to expect that the structure and development of the two systems should agree. We find that turbulence develops along the magnetosphere separatrix with a wavevector consistent with LHDI, $k\rho_e \sim (m_i/m_e)^{0.25}$ [60]. This turbulence is electromagnetic in nature and follows $\mathbf{k} \cdot \mathbf{B} = 0$. Due to computational expense, this

[1] $T_{e\parallel}$ and $T_{e\perp}$ appear to be incorrectly labeled (swapped) in panel (j), but the figure is presented unmodified from the published form.

[2] Reprinted without modification under the terms of the Creative Commons license, http://creativecommons.org/licenses/by/4.0/

Parameters	Magnetosheath		Magnetosphere	
	Measured	Normalized	Measured	Normalized
n	9 cm^{-3}	1.0	2 cm^{-3}	0.222
B_L	-15 nT	-1.0	45 nT	3.0
B_M	-20 nT	-1.33	10 nT	0.66
T_i	600 eV	4.833	1200 eV	9.769
T_e	60 eV	0.805	86.7 eV	0.706
ω_{pe}/ω_{ce}	35	0.9	6	0.2

Table 6.1: Asymptotic parameters for the 8 Dec 2015 EDR encounter

simulation is too small in size to explore turbulence near the X-line. We reproduce the crescent-shaped distribution functions observed by MMS, but balancing Ohm's Law remains an open question.

6.1 Simulation Description

The initial conditions for the simulations are similar to those observed by MMS during this diffusion region encounter. We first normalize the asymptotic values of n, B_L, B_M, and T_i as reported in Table 6.1. Temperatures are normalized to $m_i c_A^2 = 124.2$ eV. Pressure balance determines the magnetosheath electron temperature T_e, subject to the constraint that its asymptotic magnetosphere value is 0.706. This makes the magnetosheath electron temperature of 0.805 slightly larger than the magnetosphere value, in contrast to the observations. The asymptotic

Parameters	Magnetosheath	Magnetosphere
B_L	-1.563	2.882
B_M	-0.578	-1.066

Table 6.2: Final code parameters for the 8 Dec 2015 EDR encounter

parameters are not well-defined, and those listed in Table 6.1 are our best guess at describing the observations. The electrons can quickly re-equilibrate from the starting configuration if necessary.

The magnetic X-line is oriented in such a way that it approximately bisects the angle formed between the magnetic fields [94]. To ensure the M direction is indeed the direction of the dominant X-line, we rotate our coordinates by 32.8° in the $L - M$ plane, resulting in the simulation parameters in Table 6.2. The scalar quantities from Table 6.1 of course remain unchanged. The particle density n, reconnecting field component B_L, guide field B_M, and ion temperature T_i vary as a function of N with hyperbolic tangent profiles of width 1.

We performed a three-dimensional simulation with these parameters in the LMN coordinate system discussed in Section 2.4. The simulation had dimensions $(L_L, L_M, L_N) = (19.2, 4.8, 9.6)$. The ion-to-electron mass ratio was set to 100, which is sufficient to separate the electron and ion scales. The spatial grid has a resolution $\Delta = 0.0\overline{3}$ while the smallest physical scale is the Debye length in the magnetosphere, ≈ 0.08. The simulation uses 100 particles per cell per species when $n = 1.0$, which implies ≈ 22 particles per cell in the low-density magnetosphere. To mitigate the resulting noise, our analysis of this case employs averages over multiple cells.

The velocity of light is $c = 15$ so that $\omega_{pe}/\Omega_{ce} = 0.9$ in the asymptotic magnetosheath and 0.2 in the asymptotic magnetosphere. Similar to the simulations presented in Chapter 4 and 5, we do not force the rate of reconnection with an external boundary condition; instead, the boundary conditions are periodic in all directions.

6.2 Developing Turbulence

Just as in the simulations of the 16 October 2015 event, reconnection proceeds and turbulence develops along the magnetosphere separatrix. Despite the fact that magnetic shear can stabilize LHDI [95], the turbulence persists even with a strong guide field. In this case, the magnetic shear across the separatrix is relatively weak (the initial shear angle is $\approx 140°$) while the ambient density gradient is strong. Figure 6.3 displays J_{eM}, the dawn-dusk electron current density, in a $L - N$ plane at three times. These times represent the onset of the instability, a time of further development, and a time near the end of the simulation. The magnetosphere (strong field, low density) is to the left and the magnetosheath (weak field, high density) is to the right. Once again, the results exhibit the typical features of asymmetric reconnection, with the magnetic islands bulging into the low-field magnetosheath [47], similar to Chapters 4 and 5. While the simulations of the 16 October event discussed previously exhibited turbulence along the magnetosphere separatrix, that turbulence had a wavevector $\mathbf{k}$ primarily in the M-direction. Here however, the turbulence appears to have a component in the L-direction. This is consistent with

the LHDI condition of $\mathbf{k} \cdot \mathbf{B} = 0$ in the presence of a large guide field.

Figure 6.4 shows J_{eM} at $t = 30$. Panel (a) is in the $L - N$ plane, as in Figure 6.3(b). Panels (b) and (c) show the current in the $M - N$ plane at both the X-line (b) and through the island (c). Turbulence develops along the magnetosphere separatrix in both the L and M direction in the cut through the island, but it is difficult to quantify the development through the X-line. While it is possible similar turbulence develops at the X-line at a later time (recall X-line turbulence was delayed with respect to O-line turbulence in the 16 October simulation), the current sheets in this simulation become strongly correlated and merge with each other soon after the time displayed here. Larger simulations are required to investigate X-line turbulence.

As was the case for the 16 October simulations, this turbulence is electromagnetic in nature. Figure 6.5 shows E_M and δB_L in the $M - N$ plane through the X-line (panels (a-f)) and the middle of the island (panels (g-l)) at the three representative times. δB_L is the fluctuating component of B_L, i.e., $\delta B_L = B_L - \langle B_L \rangle$, where $\langle B_L \rangle$ is B_L averaged over the M direction. The turbulence appears faintly in both E_M and δB_L at $t = 20$ along the magnetospheric separatrix in panels (g) and (j) and near the X-line in panels (a) and (d). It grows in strength by $t = 25$ and persists at $t = 30$. As in Figure 6.4(c), while there is some evidence of turbulence at the X-line, it is not as strong as the turbulence along the separatrix.

The wavelength of this instability can be directly measured. In panels (h-i), there are roughly 2 wavelengths present in the M direction (length $4.8d_i$). In this simulation, $1d_i \approx 8.5\rho_e$, which gives $k_M \rho_e \approx 0.31$. This value is consistent with

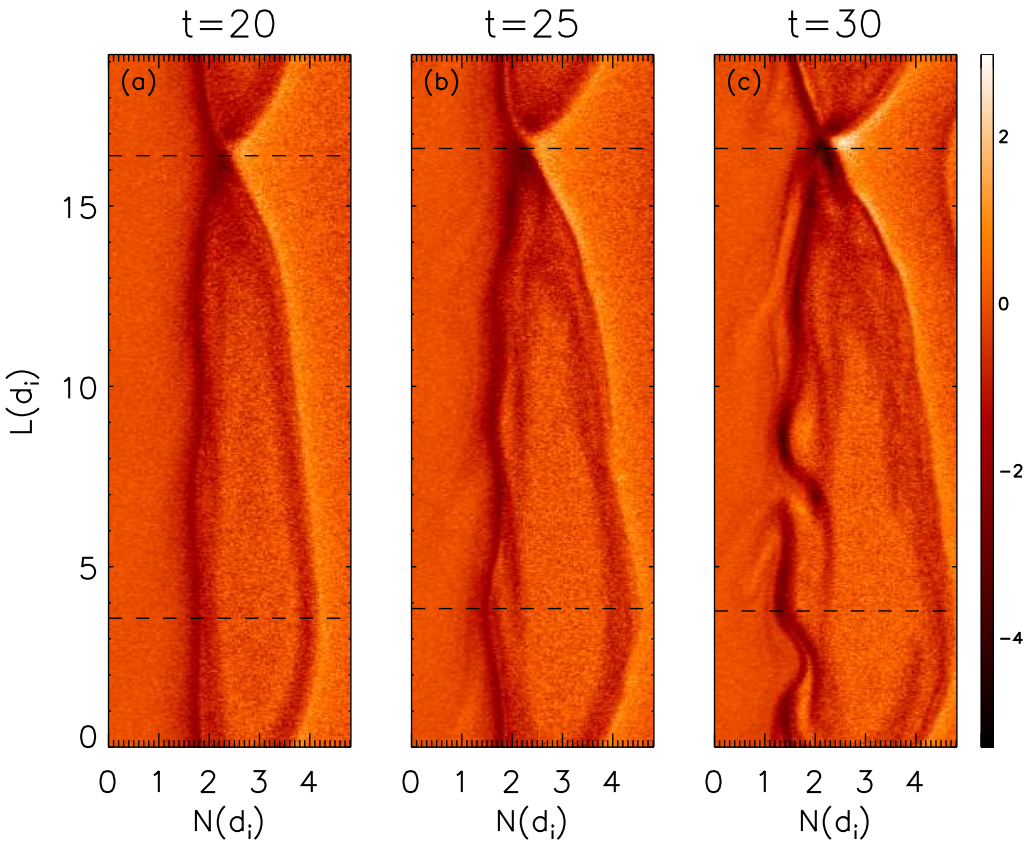

Figure 6.3: Snapshots of J_{eM}, the dawn-dusk electron current density, in one $L - N$ plane. Panels (a-c) are taken at $t = 20$, 25, and 30, respectively. These times highlight the onset of the instability, a time of further development, and a time near the end of the simulation. The colors in each panel are identically normalized, with the color bar at the right showing the range. The dashed lines in each panel indicate the locations of cuts through the x-line and island presented in Figure 6.5.

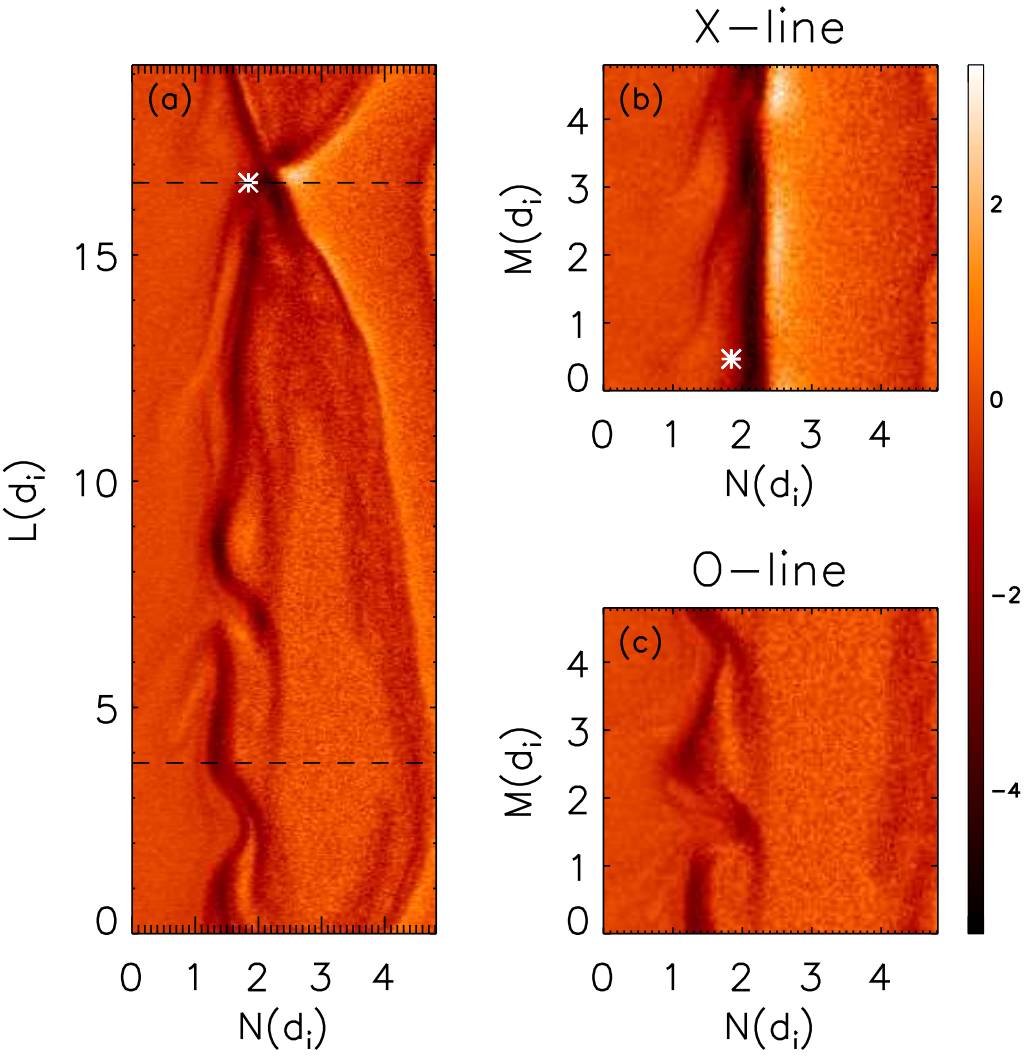

Figure 6.4: Snapshots of J_{eM}, the dawn-dusk electron current density, at $t = 30$. Panel (a): The $L - N$ plane. The two dashed lines denote the cuts shown in subsequent panels. Panel (b): The $M - N$ plane from a cut through the X-line, the upper line in panel (a). Panel (c): The $M - N$ plane from a cut through the island, the lower line in panel (a). The colors in each panel are identically normalized. The stars indicate the locations of the distribution functions presented in Figure 6.8.

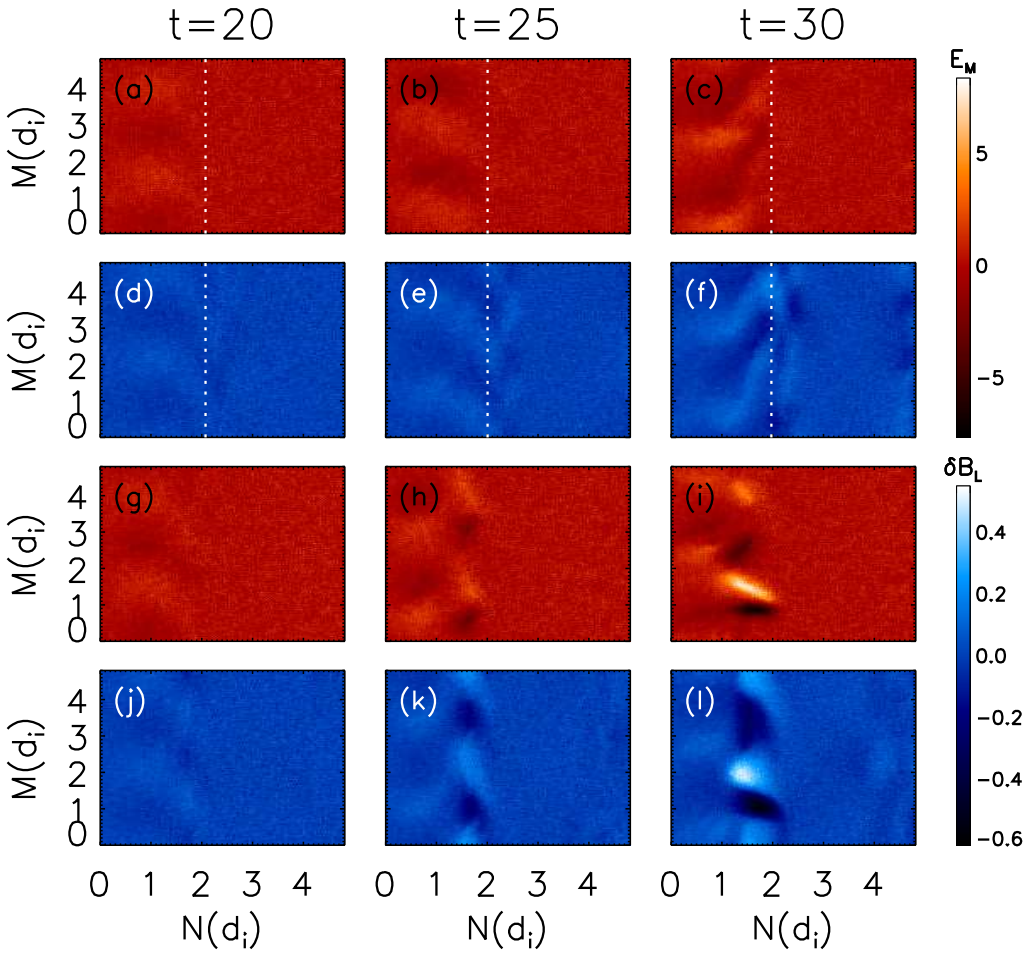

Figure 6.5: Snapshots of E_M (a-c, g-i), the electric field in the direction of the reconnection-associated current, and δB_L (d-f, j-l), the fluctuations in the reconnecting magnetic field, in the $M - N$ plane at the same times as in Figure 6.3. The cuts were taken at the positions shown by the dashed lines in Figure 6.3. Panels (a-f) are taken at the L location of the x-line, while panels (g-l) are taken through the middle of the island. The red color bar corresponds to E_M, while the blue color bar corresponds to δB_L. The dotted lines in panels (a-f) correspond to the N location of the x-line.

a recent simulation of magnetopause reconnection, where $k\rho_e$ was found to vary between approximately 0.3 and 0.5 [96]. Recalling that the longer wavelength LHDI mode has $k\rho_e \sim (m_e/m_i)^{0.25} \approx 0.32$, this measurement is consistent with the longer wavelength LHDI mode.

6.3 Fourier Analysis

We repeat the Fourier analysis introduced in Chapter 5 for this simulation. As before, the data is taken while following a magnetic field line, where this trajectory is calculated from magnetic field components averaged over the M direction. Once again, we choose s to represent the distance measured along the field line following the magnetospheric separatrix and construct $E_M(s, M)$. The resultant $E_M(s, M)$ is displayed for three times in Figure 6.6(a-c). The instability appears as linear striations, showing that the turbulence is strongly field-aligned (note the difference in vertical and horizontal axis scales). As was the case in Chapter 5, the instability is weak or non-existent at the X-line (the white dotted lines) but strong along the separatrix. As there is evidence that the turbulence near the X-line is displaced from the separatrix (see Figure 6.5(e)), the trajectory along the separatrix chosen to construct $E_M(s, M)$ misses this turbulence. No conclusion can be made about development of further turbulence at the X-line due to the simulation size.

We construct two-dimensional spatial Fourier transforms (denoted again by the operator $\mathcal{F}$) of the $s - M$ domain, $\tilde{E}_M(k_s, k_M) = \mathcal{F}[E_M(s, M)]$. We plot $\log(|\tilde{E}_M(k_s, k_M)|^2)$ for the longest wavelength modes in Figure 6.6(d)-(f). The in-

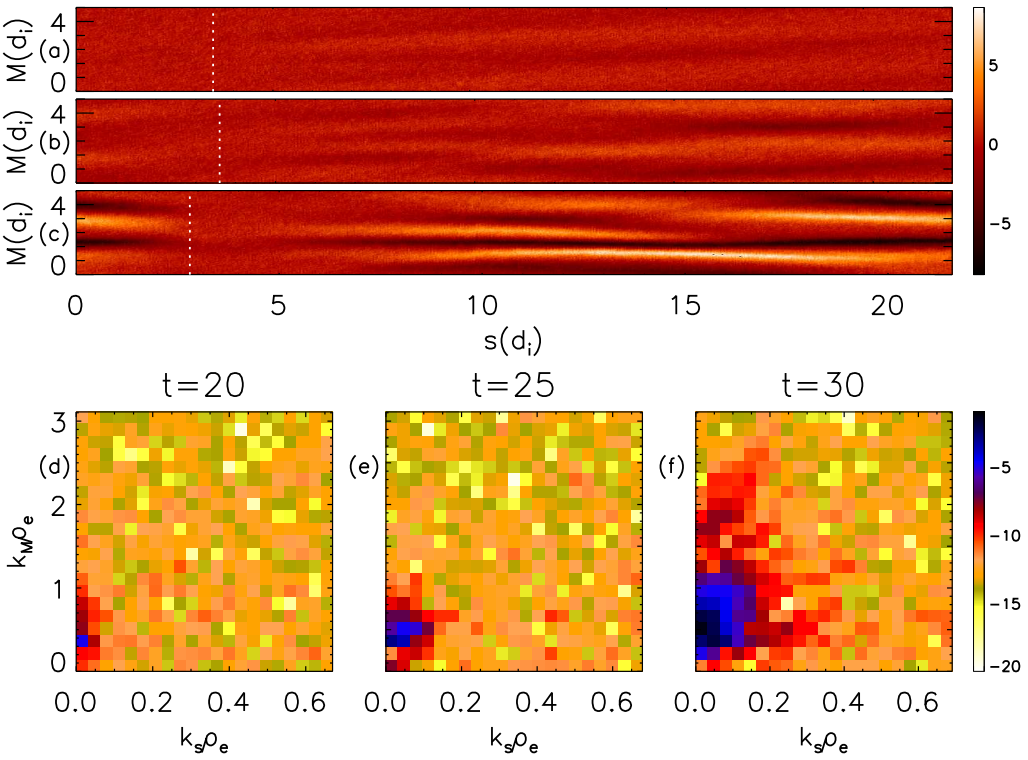

Figure 6.6: $E_M(s, M)$ (panels a-c) and Fourier transforms (panels d-f) at the same times as in Figure 6.3, where s is the distance along the average (over M) magnetic field. The data is from a surface that lies to the left (magnetospheric side) of the magnetospheric separatrix. Panel (a) shows $E_M(s, M)$ at $t = 20$; the $k_s - k_M$ power spectrum $\log(|\tilde{E}_M(k_s, k_M)|^2)$ at the same time is shown in panel (d). Panels (e) and (f) are similarly paired with panels (b), (c), and show the simulation data at $t = 25$, and 30, respectively. The white dotted lines in panels (a-c) correspond to the location of the x-line. Panels (a-c) are normalized to the same value, as seen in their accompanying color bar. Panels (d-f) also have a common normalization.

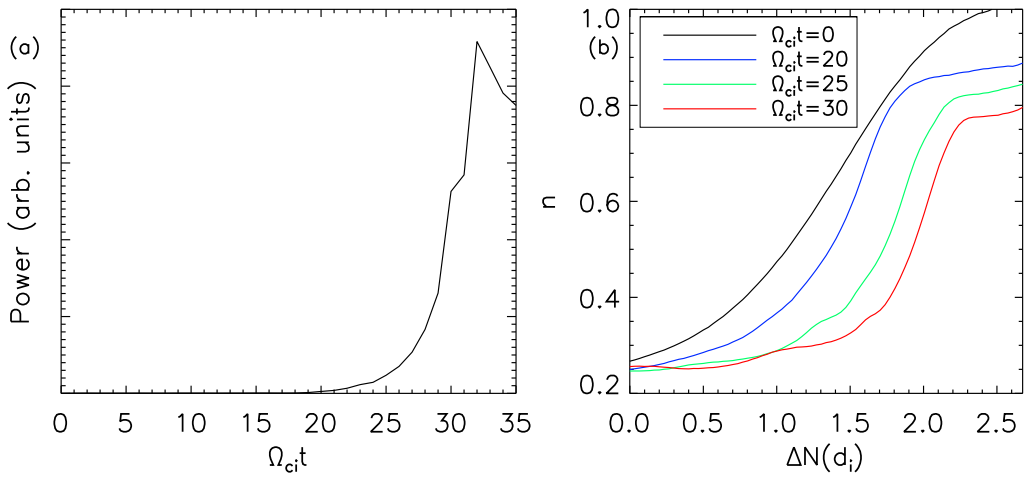

Figure 6.7: Panel (a): Power in the instability based on the Fourier transforms shown in Figure 6.6. Panel (b): Density profiles at the x-line over time. Since the location of the density gradient changes as the islands expand, the density profiles at later times are shifted in N to ease comparisons.

stability appears at $t = 20$ with $k_M \rho_e$ centered around ≈ 0.31, consistent with the calculation based on Figure 6.5. Beyond this, the instability grows in power but remains centered near this value.

The total power in the instability's fluctuating electric field

$$P = \sum_{k_s, k_M} |\tilde{E}_M(k_s, k_M)|^2 \tag{6.1}$$

is computed through the end of the simulation and plotted in Figure 6.7(a). The instability first becomes noticeable around $t = 20$ and climbs to a peak at $t = 32$. Further development is limited by the system size.

As in Chapter 5, we also explore the time evolution of the density profile. Figure 6.7(b) shows the density profiles at the X-line for several times. Again we shift the density profiles to account for the changing N location of the current sheet

as reconnection occurs. The initial density scale length L_n ($\approx 1d_i$) steepens slightly as reconnection develops, peaking at $\approx 0.5d_i$.

6.4 Electron Distribution Functions

Figure 6.8 shows electron momentum distribution functions in all three simulation planes (momentum is chosen instead of velocity due to the near-relativistic thermal velocity). The distributions are taken at the same location denoted by the stars in Figure 6.4 near the X-line. LMN coordinates are not generally the same as the magnetic field coordinates used in the first two columns of Figure 6.2. However, since these are taken near the X-line where B_L is small and the magnetic field is predominantly in the M direction, the LMN coordinates here roughly correspond to the magnetic coordinates. Panels (a-b) are taken in the $N - M$ plane and differ only in the extent of M sampled, with (b) sampling the entire domain in M. Panel (c) is taken in the L_N plane, while panel (d) is taken in the $L - M$ plane. The distribution functions are strongly reminiscent of those observed by MMS in Figure 6.2 [93]; while not exactly crescent-shaped, they still exhibit nongyrotropy. As in Chapter 4, while turbulence is strong in this simulation, the crescent-shaped distribution functions persist.

6.5 Generalized Ohm's Law

Lastly, we consider the role of this turbulence in balancing the reconnection electric field [62]. We follow the derivation in Section 4.3, where the M component

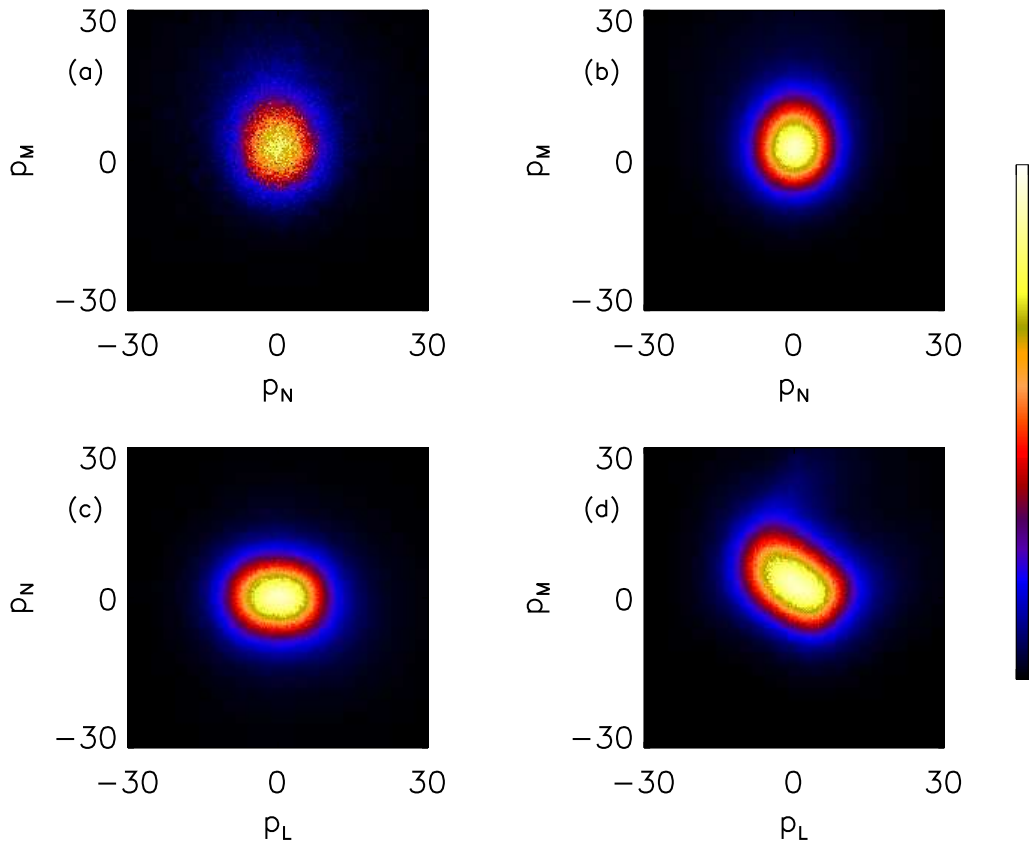

Figure 6.8: Electron distribution functions in all simulation planes. The distributions were taken at the position shown by the stars in Figure 6.4 near the X-line. In panel (a) only a limited range in M was sampled, $0.24 \leq M \leq 0.72$; panels (b-d) sample the entire box, $0 \leq M \leq 4.8$. The number of particles in each velocity bin is plotted on a linear scale that is different for each panel, although the color bar shows the relative variation.

of the generalized Ohm's law gives

$$enE_M = -envB_L/c - \left(\frac{\partial P_{LM}}{\partial L} + \frac{\partial P_{NM}}{\partial N} + \frac{\partial P_{MM}}{\partial M}\right) - m\left(\frac{\partial}{\partial t}nv_M + \frac{\partial}{\partial N}nv_N v_M\right) \tag{6.2}$$

where we assume a steady state ($\partial/\partial t = 0$). As we did in Section 4.3, we average over the M direction and decompose quantities into a mean and fluctuating component, i.e. $n = \langle n\rangle + \delta n$. We obtain

$$e\langle n\rangle\langle E_M\rangle = \langle J_N\rangle\langle B_L\rangle/c - \left[\frac{\partial}{\partial L}\langle P_{LM}\rangle + \frac{\partial}{\partial N}\langle P_{NM}\rangle\right] + \frac{m}{e}\left[\frac{\partial}{\partial L}\langle J_L\rangle\langle v_M\rangle + \frac{\partial}{\partial N}\langle J_N\rangle\langle v_M\rangle\right]$$
$$- e\langle\delta n\delta E_M\rangle + \left\langle \delta J_N\delta B_L/c + \delta J_L\delta B_N/c + \frac{m}{e}\boldsymbol{\nabla}\cdot(\delta\mathbf{J}\delta v_M)\right\rangle, \tag{6.3}$$

where we keep more terms than we did in Chapter 4.

Figure 6.9(a) shows key parameters on a cut along N through the X-line: n, B_L, B_M, E_N, v_{eN}, and v_{eM}. The vertical dashed lines denote the location of the X-point, where $B_L = 0$, and the stagnation point, where $v_{eN} = 0$. The high-speed electron flow v_{eM} is driven by E_N.

The terms in Equation 6.3 are plotted in Figure 6.9(b). We combine the terms in the top row (the convective motion, pressure tensor, and inertial terms) as 'Laminar terms' in the figure. The final two terms are interpreted as contributions from an anomalous resistivity and an anomalous viscosity as in Chapter 4. In contrast to the results from Chapter 4, neither the anomalous resistivity nor the anomalous viscosity terms are significant over this region. The two curves in panel (c), representing the left-hand side and right-hand side of Equation 6.3, roughly match, though perhaps not as well as in Chapter 4. The primary term excluded is the time dependence term, which may have a large effect. Due to the small system

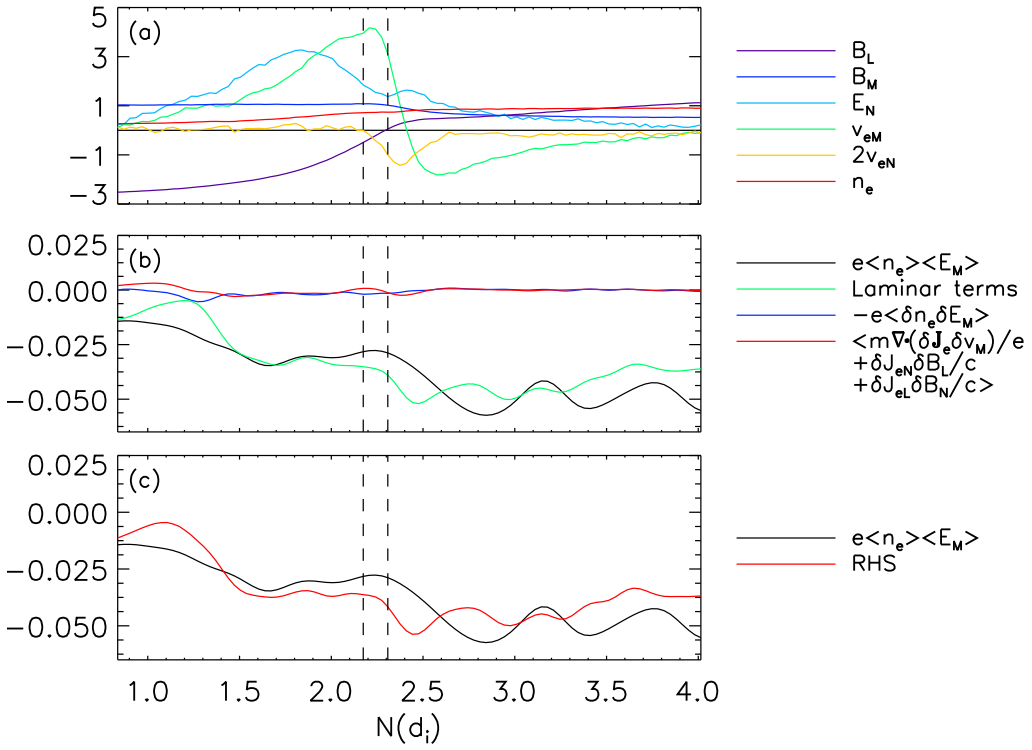

Figure 6.9: Cuts in the N direction through the electron diffusion region at $t = 25$. Panel (a): The reconnecting magnetic field B_L, the guide magnetic field B_M, the normal electric field E_N, the electron flow v_{eM}, and the density n_e all averaged over M. Panel (b): The principal terms in Ohm's law from equation 6.3. Panel (c): The sum of the left and right sides of equation 6.3. In each panel the vertical lines show the approximate position of the X-point ($N \approx 2.4$).

size in M, averaging in the M direction may not minimize the effects of turbulence as it did in Section 4.3, which could plausibly be countered with the inclusion of the time dependence term.

6.6 Conclusion

This MMS encounter on 8 December 2015 provides a contrast to the 16 October 2015 encounter discussed previously. We observe turbulence that is consistent with LHDI. The instability has a dominant wavelength satisfying $k\rho_e \sim (m_e/m_i)^{0.25}$, is observed in both electric and magnetic field components, and has a wavevector that is dominantly perpendicular to the local magnetic field. The non-gyrotropic electron distribution functions observed by MMS persist in our simulation. The reconnection electric field is balanced by laminar terms and not those arising from turbulent effects. The existence of turbulence near the X-line is yet to be investigated.

Chapter 7: Conclusions

7.1 Summary

In this thesis I performed simulations of two MMS diffusion region encounters, one with a weak constant initial guide field and the other with a strong varying guide field. While 2D simulations remained laminar, the introduction of a third dimension allowed for significant turbulence to develop. In the weak guide field case, this turbulence developed first along the magnetosphere separatrix before developing along the magnetosheath separatrix and the X-line. In the strong guide field case, turbulence primarily develops along the magnetosphere separatrix; soon after, the magnetic islands merge with each other, so turbulence along the magnetosheath separatrix and the X-line has not been investigated. In both cases, the turbulence is seen in both the electric and magnetic field components, is field aligned, and has a dominant wavelength satisfying $k\rho_e \sim (m_i/m_e)^{0.25}$, making it consistent with the LHDI. Despite this turbulence, in both cases the crescent-shaped features observed by MMS in the electron velocity-space distribution functions persist.

In both simulations we explore the balancing of the reconnection electric field by comparing terms of the generalized Ohm's law in a cut through the X-line. In the weak guide field case, we find that two terms arising from turbulence, one corre-

sponding to anomalous resistivity and another to anomalous viscosity, are essential in balancing the reconnection electric field. The anomalous resistivity term is large around the stagnation point but diminished near the X-point, while the anomalous viscosity term is large over a broad region. In contrast, in the strong guide field case we find neither the anomalous resistivity nor the viscosity terms to be significant, and the reconnection electric field is balanced by laminar term.

For the weak guide field simulation we also evaluate Ohm's law locally on cuts through the region of instability. We observe peaks of E_M around ± 10 mV/m, which is very close to values reported in the MMS data. We do not, however, observe the large peaks in $E_\parallel$ that are present in MMS data and other simulations.

7.2 Future Work

Several possibilities for extending the work presented here exist. We are currently in the process of simulating the strong guide field case with different parameters; namely, the simulation is twice as large, with $(L_L, L_M, L_N) = (40, 10, 20)$, a grid resolution of $\Delta = 0.025$, and velocity of light $c = 20$. This larger size in M will allow us to explore turbulence along the magnetosheath separatrix and X-line and may help with the analysis of the generalized Ohm's Law.

Additionally, there has been recent discussion of reconnection occurring at a very small scale [97]. It is conceivable that reconnection could take place within the regions of turbulence seen in the simulations presented herein, which could occur at faster timescales and have large localized reconnection electric fields. For the weak

guide field case, we have found oppositely directed B_N pairs on the magnetosphere side of the reversal region of B_L with reconnection outflows in the N direction. Further analysis of this simulation could prove fruitful, along with the search for these signatures in the strong guide field case.

The large amplitude, short-timescale fluctuations of the parallel electric field $E_\parallel$ observed by MMS [72, 85] but not seen in our simulations are a concern. One possible reason we may not see these intense parallel electric fields is the ratio between the Debye length λ_D and the electron inertial length d_e[1], which is much larger numerically than it is physically, particularly in the strong guide field simulation. If we assume that $E_\parallel$ is established by creating a parallel potential drop $\Delta\phi$ such that $E_\parallel = \Delta\phi/\Delta x$ and that Δx scales like λ_D, a larger-than-physical λ_D would result in a smaller $E_\parallel$ for the same $\Delta\phi$. Another possibility is that the low number of particles in the low-density magnetosphere makes these electric fields difficult to detect. We are currently exploring the implementation of weighted macro-particles, increasing the number of numerical macro-particles representing the smaller number of actual particles, which would decrease the noise in low-density regions.

[1] λ_D/d_e is equivalent to v_e/c

Appendix A: LHDI Dispersion Relation Derivation

Here we derive the dispersion relation for LHDI. While there are many papers deriving full dispersion relations for the LHDI [54, 57, 66, 95, 98–101], the derivation below follows [55]. Since we are concerned with kinetic effects, we must utilize aspects of kinetic theory.

A.1 Equilibrium Configuration

Recall the equilibrium configuration discussed in Chapter 3: The magnetic field $\mathbf{B}_0 = B_0(x)\hat{\mathbf{z}}$ and density $n(x)$ vary with respect to x, while the electric field $\mathbf{E}_0 = -E_0\hat{\mathbf{x}}$ is constant. The particles of species j (e for electrons, i for ions) drift with speed $v_{yj} = v_E + v_{dj}$, where

$$v_E = cE_0/B_0 \tag{A.1}$$

is the $E \times B$ drift and

$$v_{dj} = \mathrm{sgn}(q_j)\frac{T_j}{m_j\omega_{cj}}\frac{\partial}{\partial x}\ln\left(nT_j\right) \tag{A.2}$$

is the particle diamagnetic drift, with $n = n_e(x) = n_i(x)$ the density, $T_j(x)$ the particle temperature, m_j the particle mass, and $\omega_{cj} = |q_j|\, B_0/m_j c$ the particle cyclotron frequency.

The electron distribution function can be written as

$$F_{e0}\left(v_\perp^2, v_z^2, X\right) = n(X)\left(\frac{1}{\pi v_e^2(X)}\right)^{3/2} \exp\left(-\frac{v_\perp^2 + v_z^2}{v_e^2(X)}\right), \tag{A.3}$$

where $v_\perp^2 = v_x^2 + (v_y - v_E)^2$, $X = x - (v_y - v_E)/\omega_{ce}$, and $v_e(X) = \sqrt{2T_e(X)/m_e}$. We expand the X-dependent variables locally, which gives

$$F_{e0}\left(v_\perp^2, v_z^2\right) \simeq n\left(\frac{1}{\pi v_e^2}\right)^{3/2} \exp\left(-\frac{v_\perp^2 + v_z^2}{v_e^2}\right) \times \left\{1 - \epsilon_n \frac{v_y - v_E}{\omega_{ce}}\left[1 - \frac{\epsilon_T}{\epsilon_n}\left(\frac{3}{2} - \frac{v_\perp^2 + v_z^2}{v_e^2}\right)\right]\right\}, \tag{A.4}$$

where

$$\epsilon_n = \frac{1}{n}\frac{\partial n}{\partial x} = \frac{\partial}{\partial x}\ln(n) \tag{A.5}$$

and

$$\epsilon_T = \frac{1}{T_e}\frac{\partial T_e}{\partial x} = \frac{\partial}{\partial x}\ln(T_e) \tag{A.6}$$

are the inverse length scales of the density and temperature gradients, respectively.

The ion distribution function can be written as

$$F_{i0}\left(v_\perp^2, v_z^2\right) = n\left(\frac{1}{\pi v_i^2}\right)^{3/2} \exp\left(-\frac{v_\perp^2 + v_z^2}{v_i^2}\right), \tag{A.7}$$

where $v_\perp^2 = v_x^2 + (v_y - v_{yi})^2$, with v_{yi} and v_i defined above. It is assumed the ions are unmagnetized and $\partial T_i/\partial x = 0$.

Lastly, we define the inverse length scale of the magnetic field,

$$\epsilon_B = \frac{1}{B_0}\frac{\partial B_0}{\partial x} = \frac{\partial}{\partial x}\ln(B_0). \tag{A.8}$$

Using Ampére's law, we can relate these inverse length scales, finding

$$\epsilon_B = -\frac{1}{2}(\beta_i + \beta_e)\epsilon_n - \frac{1}{2}\beta_e\epsilon_T, \tag{A.9}$$

where $\beta_j = 8\pi n T_j/B_0^2$ is the local particle beta.

A.2 Linearized Maxwell Equations

To derive the dispersion relation, we need to linearize Maxwell's equations and apply them to the perturbed quantities. We assume

$$\delta\mathbf{E}\left(\mathbf{x},t\right)=\delta E_x\left(\mathbf{x},t\right)\hat{\mathbf{x}}+\delta E_y\left(\mathbf{x},t\right)\hat{\mathbf{y}} \tag{A.10}$$

and

$$\delta\mathbf{B}\left(\mathbf{x},t\right)=\delta B_z\left(\mathbf{x},t\right)\hat{\mathbf{z}}. \tag{A.11}$$

All perturbed quantities are assumed to take the form

$$\delta A\left(\mathbf{x},t\right)=\delta\hat{A}(x)\exp\left[i\left(k_y y-\omega t\right)\right], \tag{A.12}$$

where $\mathrm{Im}(\omega)>0$. In analogy to the LHDI discussion in Section 3.2, we seek modes satisfying $\mathbf{k}\cdot\mathbf{B}=0$, so we assume $k_z=0$.

Linearizing Faraday's law ($c\boldsymbol{\nabla}\times\mathbf{E}=-\partial\mathbf{B}/\partial t$) for the given configuration, we find

$$\frac{\partial}{\partial x}\delta\hat{E}_y(x)-ik_y\delta\hat{E}_x(x)=\frac{i\omega}{c}\delta\hat{B}_z(x). \tag{A.13}$$

Linearizing Ampére's law ($c\boldsymbol{\nabla}\times\mathbf{B}=4\pi\mathbf{J}+\partial\mathbf{E}/\partial t$) in the x direction gives

$$ik_y\delta\hat{B}_z(x)=\frac{4\pi}{c}\delta\hat{J}_x(x)-\frac{i\omega}{c}\delta\hat{E}_x(x), \tag{A.14}$$

where $\delta\hat{J}(x)=\sum_j e_j\int d^3\mathbf{v}\mathbf{v}\delta\hat{f}_j(x,\mathbf{v})$ is the perturbed current density and $\delta f_j(\mathbf{x},\mathbf{v},t)=\delta\hat{f}_j(x,\mathbf{v})\exp[i(k_y y-\omega t)]$ is the perturbed distribution function representing particle species j. Lastly, linearizing Poisson's equation ($\boldsymbol{\nabla}\cdot\mathbf{E}=4\pi\rho$) gives

$$\frac{\partial}{\partial x}\delta\hat{E}_x(x)+ik_y\delta\hat{E}_y(x)=4\pi\delta\hat{\rho}(x), \tag{A.15}$$

where $\delta\hat{\rho}(x) = \sum_j e_j \int d^3\mathbf{v}\delta\hat{f}_j(x,\mathbf{v})$ is the perturbed charge density.

Equations A.13 and A.14 can be combined to find

$$\delta\hat{E}_x(x) = \frac{i}{k_y}\left[-\frac{1}{1-\Delta^2}\frac{\partial}{\partial x}\delta\hat{E}_y(x) + \frac{4\pi}{c}\frac{\Delta}{1-\Delta^2}\delta\hat{J}_x(x)\right] \tag{A.16}$$

and

$$\delta\hat{B}_z(x) = \frac{i}{k_y}\left[\frac{\Delta}{1-\Delta^2}\frac{\partial}{\partial x}\delta\hat{E}_y(x) - \frac{4\pi}{c}\frac{1}{1-\Delta^2}\delta\hat{J}_x(x)\right], \tag{A.17}$$

where $\Delta = \omega/ck_y$. Combining Equations A.16 and A.15 gives

$$-\frac{i}{k_y}\frac{1}{1-\Delta^2}\frac{\partial^2}{\partial x^2}\delta\hat{E}_y(x) + ik_y\delta\hat{E}_y(x) = -\frac{4\pi i}{ck_y}\frac{\Delta}{1-\Delta^2}\frac{\partial}{\partial x}\delta\hat{J}_x(x) + 4\pi\delta\hat{\rho}(x). \tag{A.18}$$

For this local analysis, we assume the x variation of perturbed amplitudes is small ($\partial/\partial x \simeq 0$), so Equations A.16-A.18 are simplified to

$$\delta\hat{E}_x(x) = \frac{4\pi i}{ck_y}\frac{\Delta}{1-\Delta^2}\delta\hat{J}_x(x), \tag{A.19}$$

$$\delta\hat{B}_z(x) = -\frac{1}{\Delta}\delta\hat{E}_x(x), \tag{A.20}$$

and

$$\delta\hat{E}_y(x) = -\frac{4\pi i}{k_y}\delta\hat{\rho}(x). \tag{A.21}$$

These are our linearized Maxwell's equations.

A.3 Local Dispersion Relation

All that remains is to determine $\delta\hat{J}_x(x)$ and $\delta\hat{\rho}(x)$. As defined above, both depend on the perturbed distribution functions $\delta\hat{f}_j(x,\mathbf{v})$. These may be found with

the help of the Vlasov equation

$$\frac{\partial f_j}{\partial t} + \mathbf{v} \cdot \frac{\partial}{\partial \mathbf{x}} f_j + \frac{q_j}{m_j} \left(\mathbf{E} + \frac{1}{c} \mathbf{v} \times \mathbf{B} \right) \cdot \frac{\partial}{\partial \mathbf{v}} f_j = 0, \tag{A.22}$$

where f_j is the distribution function for particle species j. If we let $f_j = F_{j0} + \delta f_j$ and assume all perturbed quantities are much smaller than the background quantities, to first-order we find

$$\delta \hat{f}_j = -\frac{q_j}{m_j} \int_{-\infty}^{0} d\tau \exp\left[i k_y \Delta y'(\tau) - i\omega\tau \right] \left[\left(\delta \hat{\mathbf{E}} + \frac{\mathbf{v} \times \delta \hat{\mathbf{B}}}{c} \right) \cdot \frac{\partial}{\partial \mathbf{v}} F_{j0} \right]_{\mathbf{x}=\mathbf{x}'(\tau), \mathbf{v}=\mathbf{v}'(\tau)}, \tag{A.23}$$

where $\tau = t' - t$, $\Delta y' = y'(\tau) - y$, and $\mathbf{x}'(\tau)$ and $\mathbf{v}'(\tau)$ satisfy

$$\frac{d\mathbf{x}'}{d\tau} = \mathbf{v}' \tag{A.24}$$

and

$$\frac{d\mathbf{v}'}{d\tau} = \frac{q_j}{m_j} \left(\mathbf{E}_0 + \frac{\mathbf{v}' \times \mathbf{B}}{c} \right), \tag{A.25}$$

with the initial conditions of $\mathbf{x}'(\tau = 0) = \mathbf{x}$ and $\mathbf{v}'(\tau = 0) = \mathbf{v}$. For the detailed derivation, see [55]; this results in

$$\delta \hat{f}_i(x, \mathbf{v}) = -\frac{2ie}{m_i} \frac{\partial F_{i0} / \partial v_\perp^2}{\omega - k_y v_y} \left[v_x \left(1 - \frac{k_y v_{yi}}{\omega} \right) \delta \hat{E}_x + (v_y - v_{yi}) \delta \hat{E}_y \right] \tag{A.26}$$

and

$$\begin{aligned} \delta \hat{f}_e(x, \mathbf{v}) = -\frac{e}{m_e} \sum_{l,p} & \frac{J_p(\mu) \exp[i(l-p)(\phi - \pi/2)]}{\omega - k_y v_E - k_y v_B - l\omega_{ce}} \\ & \left\{ \frac{v_\perp}{\omega} \left[2(\omega - k_y v_E) \frac{\partial F_{e0}}{\partial v_\perp^2} - \frac{k_y}{\omega_{ce}} \frac{\partial F_{e0}}{\partial X} \right] J_l'(\mu) \delta \hat{E}_x \right. \\ & \left. - \frac{i}{k_y} \left[2(l\omega_{ce} + k_y v_B) \frac{\partial F_{e0}}{\partial v_\perp^2} - \frac{k_y}{\omega_{ce}} \frac{\partial F_{e0}}{\partial X} \right] J_l(\mu) \delta \hat{E}_y \right\}, \end{aligned} \tag{A.27}$$

where $J_l(\mu)$ is the Bessel function of the first kind of order l, $J_l'(\mu) = dJ_l(\mu)/d\mu$, $\mu = k_y v_\perp/\omega_{ce}$, $v_B = -\epsilon_B v_\perp^2/2\omega_{ce}$, and $\phi = \tan^{-1}[(v_y - v_E)/v_x]$.

Using $\delta\hat{J}(x) = \sum_j e_j \int d^3\mathbf{v}\mathbf{v}\delta\hat{f}_j(x,\mathbf{v})$, we find

$$\delta\hat{J}_x = \frac{1}{2\pi}\frac{\omega_{pe}^2}{\omega}\left(i\Phi_1\delta\hat{E}_x - \frac{\omega}{k_y v_e}\Phi_2\delta\hat{E}_y\right), \tag{A.28}$$

where

$$\Phi_1 = \frac{2}{v_e^4}\int_0^\infty dv_\perp \frac{v_\perp^3[J_0'(\mu)]^2\exp(-v_\perp^2/v_e^2)}{\omega - k_y v_E - k_y v_B}\Lambda, \tag{A.29}$$

$$\Phi_2 = \frac{2}{v_e^3}\int_0^\infty dv_\perp \frac{v_\perp^2 J_0(\mu)J_0'(\mu)\exp(-v_\perp^2/v_e^2)}{\omega - k_y v_E - k_y v_B}\Lambda, \tag{A.30}$$

$\Lambda = \omega - k_y v_E - k_y v_n + k_y v_T(1 - v_\perp^2/v_e^2)$, $\omega_{pe}^2 = 4\pi ne^2/m_e$ is the electron plasma frequency, $v_n = -(T_e/m_e\omega_{ce})\epsilon_n$, and $v_T = -(T_e/m_e\omega_{ce})\epsilon_T$. Here we have kept only the $l = 0$ term.

Similarly, using $\delta\hat{\rho}(x) = \sum_j e_j \int d^3\mathbf{v}\delta\hat{f}_j(x,\mathbf{v})$ we find

$$\delta\hat{\rho} = \frac{k_y}{2\pi}\frac{\omega_{pe}^2}{\omega^2}\left\{\frac{\omega}{k_y v_e}\Phi_2\delta\hat{E}_x - i\frac{\omega^2}{k_y^2 v_e^2}\left[\frac{T_e}{T_i}\left(1 + \xi_i Z(\xi_i)\right) + (1 - \Phi_3)\right]\delta\hat{E}_y\right\}, \tag{A.31}$$

where

$$\Phi_3 = \frac{2}{v_e^2}\int_0^\infty dv_\perp \frac{v_\perp J_0^2(\mu)\exp(-v_\perp^2/v_e^2)}{\omega - k_y v_E - k_y v_B}\Lambda, \tag{A.32}$$

$Z(\xi)$ is the plasma dispersion function

$$Z(\xi) = \frac{1}{\sqrt{\pi}}\int_{-\infty}^\infty dx \frac{\exp(-x^2)}{x - \xi}, \tag{A.33}$$

and $\xi_i = (\omega - k_y v_{yi})/k_y v_i$.

We substitute Equations A.28 and A.31 into our linearized Maxwell's equations

(Eqns. A.19 and A.21) and find

$$\begin{pmatrix} D_{xx} & D_{xy} \\ D_{yx} & D_{yy} \end{pmatrix} \begin{pmatrix} \delta\hat{E}_x \\ \delta\hat{E}_y \end{pmatrix} = \begin{pmatrix} 0 \\ 0 \end{pmatrix}, \tag{A.34}$$

where

$$D_{xx} = 1 - \frac{c^2 k_y^2}{\omega^2} - \frac{2\omega_{pe}^2}{\omega^2}\Phi_1, \tag{A.35}$$

$$D_{xy} = -D_{yx} = -2i\frac{\omega_{pe}}{\omega}\frac{\omega_{pe}}{k_y v_e}\Phi_2, \tag{A.36}$$

and

$$D_{yy} = 1 + \frac{2\omega_{pi}^2}{k_y^2 v_i^2}\left\{1 + \xi_i Z(\xi_i)\right\} + \frac{2\omega_{pe}^2}{k_y^2 v_e^2}\left(1 - \Phi_3\right). \tag{A.37}$$

The dispersion relation is given by $\det \mathbf{D} = 0$, which assuming $|\omega|^2 \ll c^2 k_y^2$ is

$$\left(1 + \frac{2\omega_{pe}^2}{c^2 k_y^2}\Phi_1\right)\left[1 + \frac{2\omega_{pi}^2}{k_y^2 v_i^2}\left(1 + \xi_i Z(\xi_i)\right) + \frac{2\omega_{pe}^2}{k_y^2 v_e^2}\left(1 - \Phi_3\right)\right] = -\frac{2\omega_{pe}^2}{c^2 k_y^2}\frac{2\omega_{pe}^2}{k_y^2 v_e^2}\Phi_2^2. \tag{A.38}$$

Bibliography

[1] James L. Burch and James F. Drake. Reconnecting magnetic fields. *Amer. Scientist*, 97(5):392–399, 2009.

[2] R.C. Carrington. Description of a singular appearance seen in the sun on September 1, 1859. *MNRAS*, 20:13–15, 1859.

[3] R. Hodgson. On a curious appearance seen in the sun. *MNRAS*, 20:15–16, 1859.

[4] R. G. Giovanelli. Magnetic and electric phenomena in the sun's atmosphere associated with sunspots. *MNRAS*, 107, 1947.

[5] J.W. Dungey. Lxxvi. conditions for the occurrence of electrical discharges in astrophysical systems. *The London, Edinburgh, and Dublin Philosophical Magazine and Journal of Science*, 44(354):725–738, 1953.

[6] J.W. Dungey. The neutral point discharge theory of solar flares. A reply to Cowling's critcism. *Electromagnetic Phenomena in Cosmical Physics, Proceedings from IAU Symposium*, 6:135, 1958.

[7] E.N. Parker. The solar-flare phenomenon and the theory of reconnection and annihiliation of magnetic fields. *Astrophys. Journal Supp.*, 8, July 1963.

[8] P. A. Sweet. *Electromagnetic Phenomena in Cosmical Physics*, page 123. Cambridge University Press, New York, 1958.

[9] E. N. Parker. Acceleration of cosmic rays in solar flares. *Phys. Rev.*, 107:830–836, 1957.

[10] E. N. Parker. Sweet's mechanism for merging magnetic fields in conducting fluids. *J. Geophys. Res.*, 62(4):509–520, 1957.

[11] Harry E. Petschek. Magnetic field annihilation. In *Proc. AAS-NASA Symp. Phys. Solar Flares*, volume 50 of *NASA-SP*, pages 425–439, 1964.

[12] D. Biskamp. Magnetic reconnection via current sheets. *Phys. Fluids*, 29(5):1520–1531, 1986.

[13] M. Ugai and T. Tsuda. Magnetic field-line reconnexion by localized enhancement of resistivity. I - evolution in a compressible MHD fluid. *Journal of Plasma Physics*, 17:337–356, 1977.

[14] B. N. Rogers, R. E. Denton, J. F. Drake, and M. A. Shay. The role of dispersive waves in collisionless magnetic reconnection. *Phys. Rev. Lett.*, 87(19):195004, 2001.

[15] J. Birn, J. F. Drake, M. A. Shay, B. N. Rogers, R. E. Denton, M. Hesse, M. Kuznetsova, Z. W. Ma, A. Bhattacharjee, A. Otto, and P. L. Pritchett. Geospace Environmental Modeling (GEM) magnetic reconnection challenge. *J. Geophys. Res.*, 106(A3):3715–3719, 2001.

[16] M. Øieroset, M. Fujimoto, R. P. Lin, and R. P. Lepping. In situ detection of collisionless reconnection in the earth's magnetotail. *Nature*, 412:414–417, 2001.

[17] F. S. Mozer, S. D. Bale, and T. D. Phan. Evidence of diffusion regions at a subsolar magnetopause crossing. *Phys. Rev. Lett.*, 89, 2002.

[18] J. D. Scudder, F. S. Mozer, N. C. Maynard, and C. T. Russell. Fingerprints of collisionless reconnection at the separator, I, Ambipolar-Hall signatures. *Journal of Geophysical Research: Space Physics*, 107(A10):SMP 13–1–SMP 13–38, 2002. 1294.

[19] C. T. Russell. Planetary magnetospheres. *Reports on Progress in Physics*, 56(6):687, 1993.

[20] William Gilbert. *De Magnete*. Peter Short, London, 1600.

[21] S. Chapman and V.C.A. Ferraro. A new theory of magnetic storms. *Terr. Mag.*, 36:77–97, 1931.

[22] S. Chapman and V.C.A. Ferraro. A new theory of magnetic storms. *Terr. Mag.*, 36:171–186, 1931.

[23] S. Chapman and V.C.A. Ferraro. A new theory of magnetic storms, II. The main phase. *Terr. Mag.*, 38:79, 1933.

[24] S. Chapman and V.C.A. Ferraro. The theory of the first phase of the geomagnetic storm. *Terr. Mag.*, 45:245, 1940.

[25] L. Biermann. Kometenschweife und solare korpuskularstrahlung. *Zeit. Astrophys.*, 29:274, 1951.

[26] E.N. Parker. Dynamics of the interplanetary gas and magnetic fields. *Astrophys. J.*, 128:664, 1958.

[27] T. Gold. Motions in the magnetosphere of the earth. *Journal of Geophysical Research*, 64(9):1219–1224, 1959.

[28] J. W. Dungey. Interplanetary magnetic field and the auroral zones. *Phys. Rev. Lett.*, 6(2):47–48, 1961.

[29] J. A. Van Allen, G. H. Ludwig, E. C. Ray, and C. E. McIlwain. Observation of high intensity radiation by satellites 1958 alpha and gamma. *Journal of Jet Propulsion*, 28(9):588–592, 1958.

[30] L. H. Meredith, M. B. Gottlieb, and J. A. Van Allen. Direct detection of soft radiation above 50 kilometers in the auroral zone. *Phys. Rev.*, 97:201–205, Jan 1955.

[31] L. J. Cahill and P. G. Amazeen. The boundary of the geomagnetic field. *Journal of Geophysical Research*, 68(7):1835–1843, 1963.

[32] L. J. Cahill and V. L. Patel. The boundary of the geomagnetic field, August to November 1961. *Planet. and Space Sci.*, 15:997–1033, 1967.

[33] C.P. Escoubet, R. Schmidt, and M.L. Goldstein. Cluster – science and mission overview. *Space Science Reviews*, 79(1):11–32, 1997.

[34] V. Angelopoulos. The THEMIS mission. *Space Science Reviews*, 141(1):5, 2008.

[35] C. T. Russell. The magnetopause. In *Physics of Magnetic Flux Ropes*, pages 439–453. American Geophysical Union, 1990.

[36] J. L. Burch, T. E. Moore, R. B. Torbert, and B. L. Giles. Magnetospheric multiscale overview and science objectives. *Space Science Reviews*, 199(1):5–21, 2016.

[37] S. Curtis. The Magnetospheric Multiscale Mission–resolving fundamental processes in space plasmas. report of the NASA Science and Technology Definition Team for the Magnetospheric Multiscale (MMS) Mission. *NASA/TM 2000-209883*, 1999.

[38] J. L. Burch, R. B. Torbert, T. D. Phan, L.-J. Chen, T. E. Moore, R. E. Ergun, J. P. Eastwood, D. J. Gershman, P. A. Cassak, M. R. Argall, S. Wang, M. Hesse, C. J. Pollock, B. L. Giles, R. Nakamura, B. H. Mauk, S. A. Fuselier, C. T. Russell, R. J. Strangeway, J. F. Drake, M. A. Shay, Yu. V. Khotyaintsev, P.-A. Lindqvist, G. Marklund, F. D. Wilder, D. T. Young, K. Torkar, J. Goldstein, J. C. Dorelli, L. A. Avanov, M. Oka, D. N. Baker, A. N. Jaynes, K. A. Goodrich, I. J. Cohen, D. L. Turner, J. F. Fennell, J. B. Blake, J. Clemmons, M. Goldman, D. Newman, S. M. Petrinec, K. J. Trattner, B. Lavraud, P. H. Reiff, W. Baumjohann, W. Magnes, M. Steller, W. Lewis, Y. Saito, V. Coffey, and M. Chandler. Electron-scale measurements of magnetic reconnection in space. *Science*, 352(6290), 2016.

[39] H. Alfvén. On the Existence of Electromagnetic–Hydrodynamic Waves. *Arkiv for Astronomi*, 29:1–7, 1943.

[40] D. A. Uzdensky and R. M. Kulsrud. Two-dimensional numerical simulation of the resistive reconnection layer. *Physics of Plasmas*, 7(10):4018–4030, 2000.

[41] B. D. Jemella, M. A. Shay, J. F. Drake, and B. N. Rogers. Impact of frustrated singularities on magnetic island evolution. *Phys. Rev. Lett.*, 91:125002, Sep 2003.

[42] B. D. Jemella, J. F. Drake, and M. A. Shay. Singular structure of magnetic islands resulting from reconnection. *Physics of Plasmas*, 11(12):5668–5672, 2004.

[43] F. Trintchouk, M. Yamada, H. Ji, R. M. Kulsrud, and T. A. Carter. Measurement of the transverse spitzer resistivity during collisional magnetic reconnection. *Physics of Plasmas*, 10(1):319–322, 2003.

[44] Ivo Furno, Thomas P. Intrator, Erik W. Hemsing, Scott C. Hsu, S. Abbate, Paolo Ricci, and Giovanni Lapenta. Coalescence of two magnetic flux ropes via collisional magnetic reconnection. *Physics of Plasmas*, 12(5):055702, 2005.

[45] M. A. Shay, J. F. Drake, B. N. Rogers, and R. E. Denton. The scaling of collisionless, magnetic reconnection for large systems. *Geophys. Res. Lett.*, 26(14):2163–2166, 1999.

[46] J. D. Huba and L. I. Rudakov. Hall magnetic reconnection rate. *Phys. Rev. Lett.*, 93(17), 2004.

[47] P. A. Cassak and M. A. Shay. Scaling of asymmetric magnetic reconnection: General theory and collisional simulations. *Phys. Plasmas*, 14, 2007.

[48] A. Zeiler, D. Biskamp, J. F. Drake, B. N. Rogers, M. A. Shay, and M. Scholer. Three-dimensional particle simulations of collisionless magnetic reconnection. *J. Geophys. Res.*, 107(A9):1230, 2002.

[49] O. Buneman. Excitation of field aligned sound waves by electron streams. *Phys. Rev. Lett.*, 10:285–287, Apr 1963.

[50] D. T. Farley. Two-stream plasma instability as a source of irregularities in the ionosphere. *Phys. Rev. Lett.*, 10:279–282, Apr 1963.

[51] C. K. Birdsall and A. B. Langdon. *Plasma Physics via Computer Simulation*, chapter 8. Institute of Physics Publishing, Philadelphia, 1991.

[52] H. Lewy, K. Friedrichs, and R. Courant. Über die partiellen differenzengleichungen der mathematischen physik. *Mathematische Annalen*, 100:32–74, 1928.

[53] John Wesson. *Tokamaks*. Oxford University Press, fourth edition, 2011.

[54] Nicholas A. Krall and Paulett C. Liewer. Low-frequency instabilities in magnetic pulses. *Phys. Rev. A*, 4:2094–2103, Nov 1971.

[55] R. C. Davidson, N. T. Gladd, C. S. Wu, and J. D. Huba. Effects of finite plasma beta on the lower-hybrid-drift instability. *The Physics of Fluids*, 20(2):301–310, 1977.

[56] J. D. Huba, J. F. Drake, and N. T. Gladd. Lower-hybrid-drift instability in field reversed plasmas. *The Physics of Fluids*, 23(3):552–561, 1980.

[57] D. Winske. Current-driven microinstabilities in a neutral sheet. *The Physics of Fluids*, 24(6):1069–1076, 1981.

[58] Motohiko Tanaka and Tetsuya Sato. Simulations on lower hybrid drift instability and anomalous resistivity in the magnetic neutral sheet. *Journal of Geophysical Research: Space Physics*, 86(A7):5541–5552, 1981.

[59] J. U. Brackbill, D. W. Forslund, K. B. Quest, and D. Winske. Nonlinear evolution of the lower-hybrid drift instability. *The Physics of Fluids*, 27(11):2682–2693, 1984.

[60] William Daughton. Electromagnetic properties of the lower-hybrid drift instability in a thin current sheet. *Phys. Plasmas*, 10(3103), 2003.

[61] R. E. Denton, B. U. . Sonnerup, H. Hasegawa, T. D. Phan, C. T. Russell, R. J. Strangeway, B. L. Giles, D. Gershman, and R. B. Torbert. Motion of the mms spacecraft relative to the magnetic reconnection structure observed on 16 october 2015 at 1307 ut. *Geophysical Research Letters*, 43(11):5589–5596, 2016. 2016GL069214.

[62] Michael Hesse, Nicolas Aunai, David Sibeck, and Joachim Birn. On the electron diffusion region in planar, asymmetric systems. *Geophys. Res. Lett.*, 41(24), 2014.

[63] M. A. Shay, T. D. Phan, C. C. Haggerty, M. Fujimoto, J. F. Drake, K. Malakit, P. A. Cassak, and M. Swisdak. Kinetic signatures of the region surrounding the x-line in asymmetric (magnetopause) reconnection. *Geophys. Res. Lett.*, 43, 2016.

[64] N. Bessho, L.-J. Chen, and M. Hesse. Electron distribution functions in the diffusion region of asymmetric magnetic reconnection. *Geophys. Res. Lett.*, 43:1828–1836, 2016.

[65] L. Price, M. Swisdak, J. F. Drake, P. A. Cassak, J. T. Dahlin, and R. E. Ergun. The effects of turbulence on three-dimensional magnetic reconnection at the magnetopause. *Geophys. Res. Lett.*, 43, 2016.

[66] V. Roytershteyn, W. Daughton, H. Karimabadi, and F. S. Mozer. Influence of the lower-hybrid drift instability on magnetic reconnection in asymmetric configurations. *Phys. Rev. Lett.*, 108, 2012.

[67] P. L. Pritchett and F. S. Mozer. Rippling mode in the subsolar magnetopause current layer and its influence on three-dimensional magnetic reconnection. *J. Geophys. Res.*, 116, 2011.

[68] P. L. Pritchett, F. S. Mozer, and M. Wilber. Intense perpendicular electric fields associated with three-dimensional magnetic reconnection at the subsolar magnetopause. *J. Geophys. Res.*, 117, 2012.

[69] P. L. Pritchett. The influence of intense electric fields on three-dimensional asymmetric magnetic reconnection. *Phys. Plasmas*, 20, 2013.

[70] Sang-Yun Lee, Ensang Lee, Khan-Hyuk Kim, Dong-Hun Lee, Jongho Seon, and Ho Jin. Electron Debye scale Kelvin-Helmholtz instability: electrostatic particle-in-cell simulations. *Phys. Plasmas*, 22(122113), 2015.

[71] J. Jara-Almonte, W. Daughton, and H. Ji. Debye scale turbulence within the electron diffusion layer during magnetic reconnection. *Phys. Plasmas*, 21, 2014.

[72] R. E. Ergun, K. A. Goodrich, F. D. Wilder, J. C. Holmes, J. E. Stawarz, S. Eriksson, A. P. Sturner, D. M. Malaspina, M. E. Usanova, R. B. Torbert, P.-A. Lindqvist, Y. Khotyaintsev, J. L. Burch, R. J. Strangeway, C. T. Russell, C. J. Pollock, B. L. Giles, M. Hesse, L. J. Chen, G. Lapenta, M. V. Goldman, D. L. Newman, S. J. Schwartz, J. P. Eastwood, T. D. Phan, F. S. Mozer, J. Drake, M. A. Shay, P. A. Cassak, R. Nakamura, and G. Marklund. Magnetospheric multiscale satellites observations of parallel electric fields associated with magnetic reconnection. *Phys. Rev. Lett.*, 116:235102, Jun 2016.

[73] H. Che, J. F. Drake, and M. Swisdak. A current filamentation mechanism for breaking field magnetic field lines during reconnection. *Nature*, 474:184–187, 2011.

[74] V. M. Vasyliunas. Theoretical models of magnetic field line merging, 1. *Rev. Geophys.*, 13(1):303, Feb. 1975.

[75] Michael Hesse, Karl Schindler, Joachim Birn, and Masha Kuznetsova. The diffusion region in collisionless magnetic reconnection. *Phys. Plasmas*, 6:1781, 1999.

[76] L.-J. Chen, Michael Hesse, Shan Wang, Naoki Bessho, and William Daughton. Electron energization and structure of the diffusion region during asymmetric reconnection. *Geophys. Res. Lett.*, 43, 2016.

[77] M. Swisdak, B. N. Rogers, J. F. Drake, and M. A. Shay. Diamagnetic suppression of component magnetic reconnection at the magnetopause. *J. Geophys. Res.*, 108(A5):1218, 2003.

[78] M. Swisdak, M. Opher, J. F. Drake, and F. Alouani Bibi. The vector direction of the interstellar magnetic field outside the heliosphere. *Ap. J.*, 710(2):1769–1775, 2010.

[79] T. D. Phan, G. Paschmann, J. T. Gosling, M. Øieroset, M. Fujimoto, J. F. Drake, and V. Angelopoulos. The dependence of magnetic reconnection on plasma β and magnetic shear: Evidence from magnetopause observations. *Geophys. Res.. Lett.*, 40:11–16, 2013.

[80] W. Daughton, V. Roytershteyn, H. Karimabadi, L. Yin, B. J. Albright, B. Bergen, and K. J. Bowers. Role of electron physics in the development of turbulent magnetic reconnection in collisionless plasmas. *Nature Phys.*, 7:539–542, 2011.

[81] J. F. Drake, M. Swisdak, C. Cattell, M. A. Shay, B. N. Rogers, and A. Zeiler. Formation of electron holes and particle energization during magnetic reconnection. *Science*, 299(5608):873–877, 2003.

[82] C. Cattell, J. Dombeck, J. Wygant, J. F. Drake, M. Swisdak, M. L. Goldstein, W. Keith, A. Fazakerley, M. André, E. Lucek, and A. Balogh. Cluster observations of electron holes in association with magnetotail reconnection and comparison to simulations. *J. Geophys. Res.*, 110, 2005.

[83] G. Lapenta, S. Markidis, A. Divin, M. V. Goldman, and D. L. Newman. Bipolar electric field signatures of reconnection separatrices for a hydrogen plasma at realistic guide fields. *Geophys. Res. Lett.*, 38(17), 2011.

[84] L. Price, M. Swisdak, J.F. Drake, J.L. Burch, P.A. Cassak, and R.E. Ergun. Turbulence associated with magnetopause reconnection. *J. Geophys. Res.*, 2017. submitted.

[85] R. E. Ergun, L. J. Chen, F. D. Wilder, N. Ahmadi, S. Eriksson, M. E. Usanova, K. A. Goodrich, J. C. Holmes, A. P. Sturner, D. M. Malaspina, D. L. Newman, R. B. Torbert, M. Argall, P.-A. Lindqvist, J. L. Burch, J. M. Webster, J. F. Drake, L. M. Price, P. A. Cassak, M. Swisdak, M. A. Shay, D. B. Graham, R. J. Strangeway, C. T. Russell, B. L. Giles, J. C. Dorelli, D. Gershman, L. Avanov, M. Hesse, B. Lavraud, O. Le Contel, A. Retino, T. D. Phan, M. V. Goldman, J. E. Stawarz, S. J. Schwartz, J. P. Eastwood, K.-J. Hwang, R. Nakamura, and S. Wang. Drift waves, intense parallel electric fields, and turbulence associated with asymmetric magnetic reconnection at the magnetopause. *Geophysical Research Letters*, 2017. 2016GL072493.

[86] A. Le, W. Daughton, L.-J. Chen, and J. Egedal. Enhanced electron mixing and heating in 3-d asymmetric reconnection at the earth's magnetopause. *Geophysical Research Letters*, pages n/a–n/a, 2017. 2017GL072522.

[87] C. S. Wu, Y. M. Zhou, ShihTung Tsai, S. C. Guo, D. Winske, and K. Papadopoulos. A kinetic cross-field streaming instability. *The Physics of Fluids*, 26(5):1259–1267, 1983.

[88] Hantao Ji, Stephen Terry, Masaaki Yamada, Russell Kulsrud, Aleksey Kuritsyn, and Yang Ren. Electromagnetic fluctuations during fast reconnection in a laboratory plasma. *Phys. Rev. Lett.*, 92(11), 2004.

[89] S. D. Bale, F. S. Mozer, and T. Phan. Observation of lower hybrid drift instability in the diffusion region at a reconnecting magnetopause. *Geophysical Research Letters*, 29(24):33–1–33–4, 2002. 2180.

[90] H. Karimabadi, W. Daughton, and J. Scudder. Multi-scale structure of the electron diffusion region. *GRL*, 34:L13104, 2007.

[91] T. D. Phan, G. Paschmann, C. Twitty, F. S. Mozer, J. T. Gosling, J. P. Eastwood, M. Øieroset, H. Rème, and E. A. Lucek. Evidence of magnetic reconnection initiated in the magnetosheath. *Geophys. Res. Lett.*, 2007.

[92] Yang Ren, Masaaki Yamada, Hantao Ji, Stefan P. Gerhardt, and Russell Kulsrud. Identification of the electron-diffusion region during magnetic reconnection in a laboratory plasma. *Phys. Rev. Lett.*, 101:085003, Aug 2008.

[93] J. L. Burch and T. D. Phan. Magnetic reconnection at the dayside magnetopause: Advances with MMS. *Geophysical Research Letters*, 43(16):8327–8338, 2016. 2016GL069787.

[94] M. Swisdak and J. F. Drake. Orientation of the reconnection X-line. *Geophys. Res. Lett.*, 34, 2007.

[95] J. D. Huba, N. T. Gladd, and J. F. Drake. The lower hybrid drift instability in nonantiparallel reversed field plasmas. *Journal of Geophysical Research: Space Physics*, 87(A3):1697–1701, 1982.

[96] Y. Chen, G. Toth, P.A. Cassak, X. Jia, T.I. Gombosi, J. Slavin, S. Markidis, I. Peng, and V. K. Jordanova. Global three-dimensional simulation of earth's dayside reconnection using a two-way coupled magnetohydrodynamics with embedded particle-in-cell model: initial results. *J. Geophys. Res.*, 2017. submitted.

[97] J. L. Burch. private communication.

[98] R. C. Davidson and N. T. Gladd. Anomalous transport properties associated with the lower-hybrid-drift instability. *The Physics of Fluids*, 18(10):1327–1335, 1975.

[99] J. D. Huba, N. T. Gladd, and K. Papadopoulos. The lower-hybrid-drift instability as a source of anomalous resistivity for magnetic field reconnection. *Geophys. Res. Lett.*, 4(3):125–128, 1977.

[100] R. C. Davidson, N. T. Gladd, and Y. Goren. Influence of magnetic shear on the lower-hybrid-drift instability in toroidal reversed-field pinches. *The Physics of Fluids*, 21(6):992–999, 1978.

[101] P. H. Yoon, Y. Lin, X. Y. Wang, and A. T. Y. Lui. Theory and simulation of lower-hybrid drift instability for current sheet with guide field. *Physics of Plasmas*, 15(11):112103, 2008.